Numerical methods for electromagnetic geophysics beyond 1D

PhD Thesis
by
Tue Boesen

October, 2017
Department of Geoscience
Faculty of Science and Technology
Aarhus University
Denmark

Pretext

This thesis is submitted to the Faculty of Science and Technology at Aarhus University, as part of the requirements for obtaining a PhD degree in geophysics. The bulk of this thesis is the four papers as well as the technical report, which can all be found in the appendix.

The first part of this thesis provides a general introduction to airborne electromagnetic modelling and inversion, with emphasis on numerical modelling and numerical optimizations. The introduction is followed by extended summaries of all 4 papers and the technical report. Finally, the thesis is rounded off by a discussion and outlook.

Articles in this thesis:

- Auken, E., **Boesen, T.**, and Christiansen, A.V., 2017. A review of Airborne Electromagnetic methods with focus on geotechnical and hydrological applications from 2007-2017 (Paper 1). Accepted by Advances in Geophysics.
- **Boesen, T.**, Auken, E., Christiansen, A.V., Fiandaca, G., Kirkegaard, C., Pfaffhuber, A., and Vöge, M., 2017. An efficient 2D inversion scheme for airborne frequency domain data (Paper 2). Submitted to Geophysics.
- **Boesen, T.**, Auken, E., Christiansen, A.V., Fiandaca, G., and Schamper, C., 2017. A parallel computing thin sheets inversion algorithm for airborne time domain data utilizing a variable overburden (Paper 3). Submitted to Geophysical Prospecting.
- **Boesen, T.** and Haber, E., 2017. A novel approach to solving the quasi-static electromagnetic problem (Paper 4). Submitted to Radio Science.
- **Boesen, T.**, 2017. Numerical tools and optimizations for EM geophysical methods (Technical Report). Available at http://hgg.au.dk/publications/reports/.

Peer reviewed extended abstracts:

- Kirkegaard, C., Andersen, K., Christiansen, AV., Auken, E., and **Boesen, T**, 2015. Rapid Inversion of Large Airborne AEM Data Datasets Utilizing Massively Parallel Co-processors. Presented at First European Airborne Electromagnetics Conference.
- Vöge, M., Pfaffhuber, A., Auken, E., Kirkegaard, C., **Boesen, T.**, Hendricks, S., and Hunkeler, P., 2015. 2.5 D Inversion of Sea Ice Thickness from Helicopter EM Data. Presented at First European Airborne Electromagnetics Conference.
- Kirkegaard, C, Andersen, K., **Boesen T.**, Christiansen, AV., Auken, E., and Fiandaca, G., 2015. Utilizing massively parallel co-processors in the

AarhusInv 1D forward and inverse AEM modelling code. Presented at ASEG.

- **Boesen, T.**, Auken, E., Vöge, M., Kirkegaard, C., Andersen, KR., Pfaffhuber, AA., and Christiansen AV., 2016. 2D FEM Inversion With A Moving Footprint And A hybrid 1D And 2D Forward And Derivative Implementation. Presented at AGU.

- Auken, E., **Boesen, T.**, Christiansen, AV., Fiandaca, G., Pfaffhuber, AA., and Vöge, M., 2017. Efficient 2D Hybrid Inversion of Airborne Frequency Domain Data. Presented at Second European Airborne Electromagnetics Conference.

Acknowledgements

First and foremost, I would like to thank my supervisor, Esben Auken. A few years after completing my master in theoretical physics, I was living in Scotland and unsure about in which direction to take my life, when I contacted Esben Auken, my old boss, and asked if he had anything I could do for him. He promptly offered me a PhD for which I am extremely grateful. For the first half of my PhD I had the pleasure of working closely with my co-supervisor Casper Kirkegaard, for whom I have immense respect. Casper took me under his wings and spent considerable amounts of time guiding me. Unfortunately, Casper left the HydroGeophysics Group about halfway through my PhD. Luckily, Kristoffer Andersen stepped in and took over as my co-supervisor, and helped me through some of the more challenging times in my PhD, when I was stuck and felt like I was getting nowhere. Less than a year later, Kristoffer left the group as well, but at that point I was nearing the end of my PhD and luckily Gianluca Fiandaca stepped in and co-supervised the end, for which I was very grateful for, especially considering the amount of work and pressure he was already under at that point.

I am grateful, to Eldad Haber and the whole geophysics community at University of British Columbia, Canada, for taking me in and making me feel both welcome and useful. On arrival, Eldad Haber suggested a research topic to me, which he had just realized could be interesting the week before. The research I did at UBC was probably the most interesting and rewarding experience I had during my entire PhD. For those reasons, Vancouver and UBC will always be a place that I think of fondly, and long to go back to.

While Esben has not always had much time for supervision, and we certainly have had our differences during my PhD, we managed to push through the hard times. On the occasions he did have time for me, his supervision was always immensely helpful and offered key insights, which I doubt many other people in this world could have given. To mention a small example that happened only a few weeks ago: I had made some postulates in my thesis, but was missing a citation to an article that would validate my postulate. When I presented this to Esben, he said he believed he had once read an article stating just that from the late 1980's by Art Raiche and urged me to look it up... And of course he was right.

Doing a PhD can often be a lonely challenge, and because of this I am immensely grateful to my friends, who kept me sane and took my mind off the PhD every now and again, and especially to Pradip Kumar Maurya, who started his PhD around the same time as me, and who has always been both friendly and helpful.

Finally, I thank my colleagues in the HydroGeophysics Group at Aarhus University, AirTech4Water for the funding, and all co-authors on the papers presented in this thesis, for a pleasant and fruitful working environment.

Tue Jensen Boesen

Contents

Summary 1
Resumé (Danish summary) 2

1 Introduction **3**
1.1 Airborne EM systems 4
1.2 Data interpretation 6
1.2.1 Forward modelling 6
1.2.2 Inverse modelling 7
1.2.3 Numerical modelling 9
1.2.4 Numerical optimization & parallelization 11

2 A review of Airborne Electromagnetic methods with focus on geotechnical and hydrological applications from 2007-2017 (Paper 1) **13**
2.1 Introduction 13
2.2 Hardware 14
2.3 Software 15
2.4 Closing remarks 16

3 An efficient 2D inversion scheme for airborne frequency domain data (Paper 2) **17**
3.1 Introduction 17
3.2 Methodology 18
3.3 Results & Discussion 20

4 A parallel computing thin sheets inversion algorithm for airborne time domain data utilizing a variable overburden (Paper 3) **23**
4.1 Introduction 23
4.2 Methodology 24
4.3 Results & Discussion 25

5 A novel approach to solving the quasi-static electromagnetic problem (Paper 4) **29**
5.1 Introduction 29

5.2 Methodology 30
5.3 Results & Discussion 31

6 Numerical tools and optimizations for EM geophysical methods (Technical Report) 33
6.1 Introduction 33
6.2 Parallel framework 34
6.3 Sparse linear solvers 34

7 Discussion and Outlook 39

8 Bibliography 43

A Paper 1 49

B Paper 2 85

C Paper 3 125

D Paper 4 157

E Technical Report 169

Summary

Airborne electromagnetic methods have emerged as one of the most vital methods for near surface exploration. In this thesis, I present the advances made during my PhD studies to near surface exploration through electromagnetic modelling. The main body of this thesis is the four papers and the technical report presented in the appendix. The thesis begins with an introduction of the airborne electromagnetic method, followed by an introduction of the governing equations and how they are numerically solved.

Paper 1, is a review of the last decade of airborne electromagnetic methods with a focus on geotechnical and hydrological applications. The review details various advances both in the data gathering hardware, as well as the interpretive software. The focus of the review is largely to try to give the reader a holistic view of all the advances and put them into context, without diving too deeply into the technical details.

Paper 2 presents our 2D airborne electromagnetic finite element code. The goal for this code was to create a code capable of large scale 2D modelling and inversion. In order to achieve this, a local meshing scheme as well as a hybrid scheme was created. The local mesh makes the code capable of handling large surveys, by splitting a large survey into several smaller sizes. The hybrid scheme boosts the convergence speed of the code, by utilizing numerically cheaper 1D calculations as a starter for the computationally more expensive 2D calculations.

Paper 3 presents a thin conductive sheet code, which is capable of modelling multiple sheets in a two-layered earth and includes variable overburden calculations. Thin sheet modelling is useful in mineral exploration, where mineralization can often be reasonably approximated by thin conductive sheets. In order to speed up the code, several optimization steps were developed, including a sophisticated adaptive frequency sampler, which uses task parallelization, and has general applicability for frequency domain calculations.

Paper 4 is primarily a theoretical paper, in which a novel approach to solving the quasi-static Maxwell equation is presented. The approach spectrally transforms the equation into an optimal basis, where the equations decouple and each timestep only requires one response calculation. The approach is successfully demonstrated for linear timestepping. Unfortunately, we were unable to find a stable approach to non-linear timestepping, and the question whether such a stable approach exist, remains unanswered at this point.

The Technical Report presents an OpenMP parallelization framework developed during my PhD, which enables a wide range of users and developers to work with AarhusInv in an easier way. The framework is modularized, and supports various parallelization schemes including nested parallelization. Furthermore, the Technical Report presents our block-parallel sparse iterative linear solver, which shows impressive scaling properties and is highly optimized for the geophysical EM problems, which we solve in AarhusInv. Both the parallelization framework and the iterative solver are created in Fortran and can be obtained from the HydroGeophysics Group at Aarhus University.

Resumé (Danish summary)

Luftbårne elektromagnetiske metoder er blevet en af de vigtigste metoder vi har til nær-overflade undersøgelser. Jeg præsenterer i denne afhandling, udviklinger lavet under mine PhD studier indenfor nær-overflade undersøgelser ved brug af elektromagnetiske metoder. Hovedparten af denne afhandling er de 4 artikler samt den tekniske rapport, der kan findes i appendikset. Afhandlingen begynder med en introduktion af luftbårne elektromagnetiske metoder, efterfulgt af en introduktion af de fundamentale ligninger, og hvordan de løses numerisk.

Artikel 1 er en summering af, hvad der er sket indenfor luftbårne elektromagnetiske metoder i løbet af de sidste 10 år med fokus på geotekniske og hydrologiske anvendelser. Artiklen kigger både på fremskridt indenfor de fysiske systemer, der foretager målingerne, samt de numeriske koder, der anvendes til tolkning af data. Fokuset i anmeldelsen er at give læseren et overblik over feltet og at sætte de forskellige fremskridt ind i en overskuelig sammenhæng.

Artikel 2 præsenterer en 2D kode til modellering af luftbårne elektromagnetiske data. Kodens formål var at kunne modellere stor-skala undersøgelser. For at nå dette mål, udviklede vi forskellige værktøjer, blandt andet lokal modellering og hybrid modelling. Lokal modellering gør koden i stand til at håndtere stor-skala undersøgelser ved at splitte det i mange mindre modeller. Hybrid modellering hjælper med at gøre koden hurtigere, ved at kombinere numerisk "dyre"metoder med billigere metoder.

Artikel 3 præsenterer en kode, der kan modellere tynde ledende lag. Koden kan håndtere flere lag og modellere dem i en to-lags jord med variabel overbelastning. Koden er optimeret på forskellige måder, blandt andet ved brug af en adaptiv frekvens-udvælger. Frekvens-udvælgeren benytter job-parallelisering og kunne have relevans for andre frekvensdomæne koder, hvor der transformeres fra frekvensdomæne til tidsdomæne.

Artikel 4 er primært en teoretisk artikel, der præsenterer en ny måde at løse den kvasi-statiske Maxwell ligning på. Metoden spektral-transformerer ligningerne over i en optimal basis, hvori ligningerne er afkoblede, men stadigvæk kun kræver én udregning per tidsskridt. Metoden demonstreres succesfuldt for lineære tidsskridt. Desværre var vi ikke i stand til at finde en stabil måde at bruge metoden for ikke lineære tidsskridt, og hvorvidt dette er muligt er stadigvæk uafklaret.

Den tekniske rapport præsenterer en OpenMP paralleliserings skabelon, der gør det nemmere for både brugere og udviklere at arbejde med AarhusInv. Skabelonen er modulbaseret og understøtter forskellige paralleliserings metoder, blandt andet sammenflettet parallelisering. Ydermere præsenterer den tekniske rapport vores blok parallelle iterative lineære ligningssytem løser, der har imponerende skaleringsevner og er optimeret til at løse den type geofysiske problemer, der løses i AarhusInv.

Chapter 1

Introduction

Near-surface geophysics is an area with wide reaching applications, both in academia and outside academia. In near-surface geophysics, electromagnetic (EM) methods are among the most important tools for near-surface determination, and within EM methods no methods have seen as much advancement in the past decade as airborne EM (AEM) methods (Legault, 2015). The advancements of AEM methods have taken place on two fronts; interpretive software has advanced in: acccuracy, speed, and automation, while the data gathering hardware has become more: powerful, reliable, and precise.

In the early days of AEM, data quality was rather poor, which meant that AEM could be used for detection of large conductive bodies, but lacked the precision for reliable mapping of the underground. Thus, AEM was useful for mineral prospecting, but otherwise of limited use (Allard, 2007). However, with the improvement of AEM hardware over the last few decades, the data quality has become good enough to map the underground accurately, which has vastly expanded the list of applications to include: ground water mapping (Høyer et al., 2015), geo-technical application (Pfaffhuber et al., 2017), oil exploration (Zhdanov et al., 2013), Saltwater intrusion (Pedersen et al., 2017), Ice thickness determination (Vöge et al., 2015), and unexploded ordnance mapping (Doll et al., 2008) to mention a few.

Historically, 1D approximate models were the only viable and sensible way of interpreting surveys, both because of poor data quality, but also because of limited computational power. However, with the continued exponential growth in computer power and the higher data quality, more advanced interpretation schemes have finally become both feasible and sensible. So while 1D modelling is the de facto workhorse in EM modelling, and is likely to remain so in the foreseeable future, other more advanced modelling schemes are being developed and employed, where 1D modelling fails to produce satisfactory results (Ullmann et al., 2016; Scheunert et al., 2016).

This thesis starts with a short introduction to how an AEM system works, followed by a presentation of AEM methodology. This includes the underlying theory behind forward modelling, a section about inversions, how the for-

ward differential equations are numerically solved, as well as an introduction to numerical optimizations, and in particular parallelization. Following this, is a summary of Paper 1, which is a review of Airborne EM, to which I have provided a major contribution, and which is to be published in Advances in Geophysics. After this, I present three extended summaries for the articles I have authored during my Phd, all of which are submitted. Paper 2 describes a hybrid 1D/2D airborne frequency domain EM modelling and inversion code we have developed jointly with Norwegian Geotechnical Institute. Paper 3, describes a thin sheet modelling code, which includes a layered background and variable overburden. In both cases, I have spent considerable time optimizing and parallelizing these codes. Paper 4 presents a novel approach to solving the quasi-static Maxwell equations, which shows some promising results, but unfortunately suffers from a numerical instability which we have been unable to resolve. Finally this thesis ends with a summary of a Technical Report. The technical report describes an OpenMP parallel framework I have created and implemented in AarhusInv (Auken et al., 2014). Furthermore, it includes a block-parallel iterative sparse linear solver that I created in the early parts of my PhD, which is capable of solving very large sparse linear systems, and is currently used in AarhusInv as the default linear solver. Both the Technical Report as well as the source code for the two Fortran modules can be found on: `http://hgg.au.dk/publications/reports/`.

1.1 Airborne EM systems

A wide range of AEM systems exists (Legault, 2015). In the following, I will focus on helicopter transient EM (HTEM) systems, since all the cutting edge systems are of this type, and because it is the most relevant system for the work done in this thesis. However, most of the underlying theory explained here, is also applicable or easily adaptable to the vast majority of AEM systems.

A HTEM system consists of a transmitter loop and a receiver, both towed by a helicopter, as illustrated in Figure 1.1. The transmitter loop is energized through a high current, which creates the primary magnetic field (shown with blue field lines in Figure 1.1). The primary magnetic field is rapidly turned off, in order to induce a current in the ground that in turn generates secondary magnetic fields (shown with purple field lines in Figure 1.1). The strength and direction of these secondary fields depend on the resistivity of the ground, which in turn depends on the geological composition of the ground. Thus, by measuring the secondary fields, information about the underground is gathered. The secondary fields are measured using a small receiver loop, which is placed and calibrated such that it ideally does not measure the primary field, but only the secondary field emanating from the ground.

While this is simple in theory, there are several caveats, which complicate the matter significantly. First, many different materials have similar resistivities, thus some prior geological knowledge of the area is required in order to do a geological interpretation (Barfod et al., 2016). In some cases having the prior

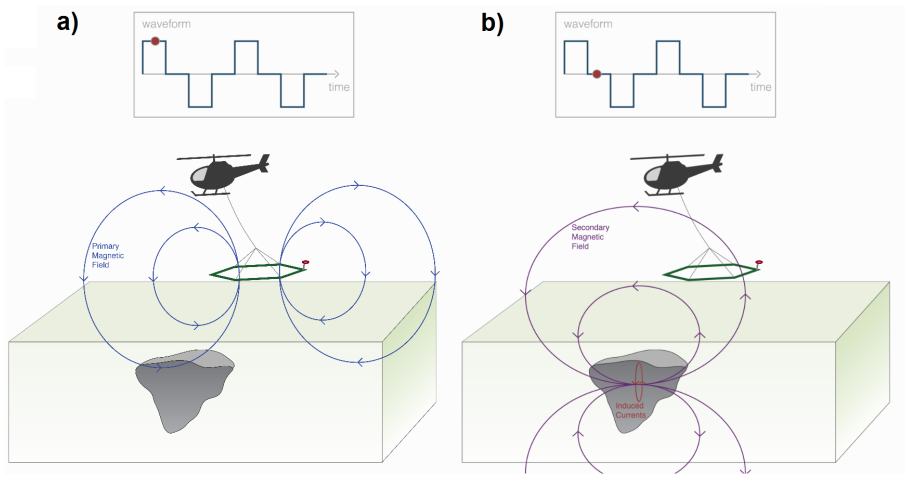

Figure 1.1: A helicopter transient EM system. The box at the top indicates the waveform as a function of time, with the red dot signalling the current time for the figure shown. The green hexagon underneath the helicopter is the transmitter loop, the small red dot at the back of the transmitter loop is the receiver loop. a) shows the system with the primary field on. b) shows a short time later, when the primary field has been turned off, and the resulting secondary field is measured by the receiver. (Modified from `https://em.geosci.xyz`, and used under Creative Commons Attribution 4.0 International License.)

geological knowledge is insufficient to uniquely identify the different materials in an area, and thus additional identifying parameters, like chargability or magnetization, have to be included (Chongo et al., 2015; Pfaffhuber et al., 2017). Secondly, there is generally an infinite number of earth resistivity compositions, which can give rise to the field measured in the receivers, thus constraints and prior information have to be imposed on the models in order to arrive at a likely earth model (Smith, 2014). Finally, there is the engineering problem of building an AEM system. While the system is simple to design in theory, it is extremely difficult to build in reality. The reasons for this are many, but to mention a few: the secondary earth response is roughly a million times weaker than the primary field, and is difficult to detect, due to remnants of the primary field as well as background noise. The frame either has to be very rigid or well determined at all points in time, and the primary field has to be well known, in order to model the resulting secondary field accurately.

Nevertheless, it is possible to design and build these systems, and today they provide a powerful tool for near-surface exploration.

1.2 Data interpretation

In the early days of geophysical EM exploration, interpretations were drawn directly on the voltage measured in the receiver; if a location provided a significant boost in the receiver signal, it was concluded that a conductive anomaly was present near this location. Since then, interpretations have come a long way. Today, interpretations are not performed directly on the receiver signal. Instead the receiver signals are jointly used in the creation of an earth resistivity model, and interpretations are then performed on the resulting resistivity model instead. This allows much more subtle receiver signals to have an impact, and furthermore reduces subjectivity from the interpretation, by transforming the EM data to something that is much closer to the geological interpretation. In order to do these more advanced interpretations; an EM forward modelling algorithm is required, as well as an inversion method.

1.2.1 Forward modelling

The question we seek to answer in EM forward modelling is this.

Given a source signal $\boldsymbol{j}_{em}(\boldsymbol{r}_0, t)$ and an earth model $\boldsymbol{m}$, what would the resulting signal measured in a receiver $\boldsymbol{s}_{fwd}(\boldsymbol{r}, t)$ be.

Mathematically we can write this as:

$$\boldsymbol{s}_{fwd} = \boldsymbol{f}_{\boldsymbol{j}_{em}}[\boldsymbol{m}] \tag{1.1}$$

where $\boldsymbol{f}_{\boldsymbol{j}_{em}}$ is the functional that transforms the model parameters, $\boldsymbol{m}$, to a receiver signal, $\boldsymbol{s}_{fwd}$, under the constraints of the source current $\boldsymbol{j}_{em}$.

The exact expression of $\boldsymbol{f}_{\boldsymbol{j}_{em}}$ depends on the modelling approximation employed. Common for all of them is that they are derived from Maxwell's equations, which in time domain can be written as (Ward and Hohmann, 1988):

$$\nabla \times \boldsymbol{e} = -\partial_t \boldsymbol{b} + \boldsymbol{j}_m, \tag{1.2}$$

$$\nabla \times \boldsymbol{h} = \partial_t \boldsymbol{d} + \boldsymbol{j} + \boldsymbol{j}_e, \tag{1.3}$$

where $\boldsymbol{b}$ is the magnetic induction field, $\boldsymbol{e}$ the electric field, $\boldsymbol{d}$ the dielectric displacement, $\boldsymbol{h}$ the magnetic field, $\boldsymbol{j}$ the electric current, and $\boldsymbol{j}_e$, $\boldsymbol{j}_m$ are electric- and magnetic-source currents. And given the constituent relations:

$$\boldsymbol{j} = \sigma \boldsymbol{e}, \tag{1.4}$$

$$\boldsymbol{d} = \epsilon \boldsymbol{e}, \tag{1.5}$$

$$\boldsymbol{b} = \mu \boldsymbol{h}, \tag{1.6}$$

where σ is the electric conductivity, ϵ the electric permittivity, and μ is the magnetic permeability, all of which we usually assume are isotropic. By combining

the differential Maxwell equations 1.2-1.3 with the constituent relations 1.4-1.6, it is possible to create a partial differential equation for either the electric or magnetic field.

By assuming zero magnetic source current, the electric field in time domain can be written as (Haber, 2014, p. 13)

$$\epsilon\partial_t^2\boldsymbol{e}(\boldsymbol{r},t) + \sigma\partial_t\boldsymbol{e}(\boldsymbol{r},t) + \nabla\times\mu^{-1}\nabla\times\boldsymbol{e}(\boldsymbol{r},t) = \partial_t\boldsymbol{j}_e. \tag{1.7}$$

Thus, given: the electric source current, the earth conductivity, as well as the permeability and permittivity; the electric field can be determined everywhere.

For geophysical EM it can generally be assumed that $\epsilon\partial_t^2\boldsymbol{e}(\boldsymbol{r},t)$ is negligible compared to the other terms, and thus the equation can be simplified to:

$$\sigma\partial_t\boldsymbol{e}(\boldsymbol{r},t) + K\boldsymbol{e}(\boldsymbol{r},t) = \partial_t\boldsymbol{j}_e, \tag{1.8}$$

where

$$K = \nabla\times\mu^{-1}\nabla\times\,. \tag{1.9}$$

Equation 1.8-1.9 is an example of a differential 3D solution in time domain. Furthermore, they are the governing equations used in Paper 4. Numerically, equation 1.8 is typically solved by: assuming a uniform magnetic permittivity, discretizing time, and sequentially stepping the electric field forward in time. However there are also other alternative ways of solving these equations. One method is to recast the equations into frequency domain, which removes the time derivatives, but comes with the cost of needing to be calculated for many frequencies, in order to be accurately transformed back to time domain (Christensen, 1990). This is done in Paper 2, where considerable time is spent reducing the number of frequency calculations required. Another approach involves the integral formulation instead of the derivative formulation of Maxwells equation, this approach is used in Paper 3, where a thin conductive sheet is considered.

All the above mentioned methods can be approximated to 1D or 2D, meaning that variables are assumed to be constant in one or both of the horizontal directions. Such assumptions can significantly speed up the calculations.

1.2.2 Inverse modelling

In the previous, the receiver signal $\boldsymbol{s}_{fwd}$ was found, given an earth model $\boldsymbol{m}$ and a source signal $\boldsymbol{j}_{em}$, as described in equation 1.1.

However, normally the receiver signal is known, while the earth model is not. Thus the relevant problem is:

$$\boldsymbol{f}_{\boldsymbol{j}}^{-1}[\boldsymbol{s}_{fwd}] = \boldsymbol{m} \tag{1.10}$$

Unfortunately, no closed form expression generally exists for $\boldsymbol{f}_{\boldsymbol{j}}^{-1}$, and hence the earth model $\boldsymbol{m}$ cannot be determined directly. Instead we attempt to estimate the model $\boldsymbol{m}$ given the observed data $\boldsymbol{s}_{fwd}$, and the forward model expressed

in equation 1.1. Estimating the earth model in this way is commonly referred to as solving the inverse problem (Haber, 2014, p. 91).

The typical way of estimating the earth model, is to transform the problem into an optimization problem by introducing an objective function, which is sought to be minimized (Haber, 2014, p. 101).

$$q = q_{obs} + q_r, \tag{1.11}$$

where

$$\begin{aligned} q_{obs} &= N_d^{-1} \left\| \boldsymbol{C}_{obs}^{-\frac{1}{2}} \delta \boldsymbol{d} \right\|_{W_{obs}} \\ &= N_d^{-1} \delta \boldsymbol{d}^T \boldsymbol{W}_{obs}^T \boldsymbol{C}_{obs}^{-1} \boldsymbol{W}_{obs} \delta \boldsymbol{d}, \end{aligned} \tag{1.12}$$

$$\begin{aligned} q_r &= N_c^{-1} \left\| \boldsymbol{C}_r^{-\frac{1}{2}} \delta \boldsymbol{m} \right\|_{W_r} \\ &= N_c^{-1} \delta \boldsymbol{m}^T \boldsymbol{R}^T \boldsymbol{W}_r^T \boldsymbol{C}_r^{-1} \boldsymbol{W}_r \boldsymbol{R} \delta \boldsymbol{m}, \end{aligned} \tag{1.13}$$

where N_d is a normalization to the number of data points, N_c is a normalization to the number of constraints, $\delta \boldsymbol{d}$ is the misfit of the forward response, $\delta \boldsymbol{m}$ is the variation in the model vector, $\boldsymbol{W}_i$ is a weight matrix, $\boldsymbol{C}_i$ is a covariance matrix, and $\boldsymbol{R}$ is a roughness matrix, detailing which model parameters are bound together. Thus, q_{obs} gives a weighted measure of the difference between the measured receiver signal, and the signal predicted by the earth model considered. While, q_r gives a weighted measure of how well the earth model matches the constraints and prior information imposed on it.

Once the objective functions have been specified, a minimization scheme is needed. As detailed in Paper 1 there are many different minimization schemes, which are used in EM inversion. The most common schemes use a linearized minimization, which requires a sensitivity analysis of the model parameters at each iteration, usually the Jacobian, $\boldsymbol{G}$. In the work I have done during this PhD, a modified Tikhonov regularization was combined with quasi-Gauss-Newton minimization schemes, which result in the following model update:

$$\boldsymbol{m}_{n+1} = \boldsymbol{m}_n + (\hat{\boldsymbol{G}}_n^T \boldsymbol{C}_n \hat{\boldsymbol{G}}_n + \boldsymbol{\Gamma}^T \boldsymbol{\Gamma})^{-1} \hat{\boldsymbol{G}}_n^T \boldsymbol{C}_n^{-1} \delta \hat{\boldsymbol{d}}_n, \tag{1.14}$$

where $\boldsymbol{\Gamma}$ is known as the Tikhonov matrix, $\hat{\boldsymbol{G}}$ is the extended Jacobian, which includes additional rows related to regularization as well as the standard Jacobian, and $\delta \hat{\boldsymbol{d}}$ is the extended misfit of the forward response.

In Paper 3, we use this inversion method, with the Tikhonov matrix being diagonal and dependent on the parameter types. In Paper 2, the Tikhonov matrix is set equal to a scaled identity matrix, which results in the modified Levenberg-Marquardt minimization scheme (Pujol, 2007):

$$\boldsymbol{m}_{n+1} = \boldsymbol{m}_n + (\hat{\boldsymbol{G}}_n^T \boldsymbol{C}_n \hat{\boldsymbol{G}}_n + \lambda_n \boldsymbol{I})^{-1} \hat{\boldsymbol{G}}_n^T \boldsymbol{C}_n^{-1} \delta \hat{\boldsymbol{d}}_n, \tag{1.15}$$

where λ_n is a tuning scalar from the Tikhonov matrix. In both cases the inversion schemes iteratively minimize the objective function to a local minimum. If the resulting data-residual is sufficiently low, we have found a likely earth-resistivity model, from which we can make the geological interpretation.

1.2.3 Numerical modelling

Physical equations, like equation 1.1-1.8, generally exist in a continuum space. In simple cases, such equations can be solved analytically - for instance when utilizing the 1D approximation, as is done for the background response in Paper 3. However, when analytical solutions are not available there are two standard approaches. The first one involves integral equation formulations, where a number of integral equations can be established but not solved directly. In this case an approximate numerical integral is often evaluated. This is the case in Paper 3, where a system of integral equation is established for thin conductive sheets. In this case the integrals are solved by discretizing the sheet into cells and integration over all cells in a sheet, in this way a discretization is only needed on the sheet. The second standard approach to numerical modelling relies on differential equations. In this approach the whole modelling space needs to be discretized, as well as a considerable boundary region. Discretization is commonly done by defining a mesh and recasting the continuous variables into discrete variables living on the mesh. The mesh and the resulting discretization can be done in many ways. The three most common choices are finite difference (FD), finite element (FE) or finite volume (FV). In the following the FD and FE methods will both be introduced since both of these methods are used in the articles presented in this thesis.

Finite difference

Finite difference (FD) is the most straightforward discretization approach. The approach relies on Taylor expansion, to approximate any continuous variable with its discrete counterpart. In EM modelling, FD meshing is typically done on a staggered grid (Yee, 1966), which can be seen in Figure 1.2. Using a staggered grid allows for a natural and accurate formulation of the discontinuous electromagnetic fields (Haber and Ascher, 2001). Using equation 1.8, as an example, and assuming an isotropic conductivity σ, and isotropic permeability μ; the discretized curl operator can be written as a matrix (Haber, 2014), and hence the whole equation can be recast as:

$$\boldsymbol{M}_\sigma \partial_t \boldsymbol{E} + \boldsymbol{K}_\mu \boldsymbol{E} = \partial_t \boldsymbol{J}_e, \tag{1.16}$$

where $\boldsymbol{M}_\sigma$ is the discretized conductivity - commonly referred to as the mass-matrix, and $\boldsymbol{K}_\mu$ is the discretized curl-curl operator given in equation 1.9 - commonly referred to as the stiffness-matrix. $\boldsymbol{E}$ is the discretized electric field, $\boldsymbol{J}_e$ is the discretized electric source current, and ∂_t depends on the precision used during the taylor approximation. Thus, the hyperbolic partial differential equations given in 1.8, have been discretized and by chosing a finite difference approximation for the time derivative, the system can effectively be transformed into a system of linear equations, which a computer can solve efficiently. This is exactly the method used in Paper 4.

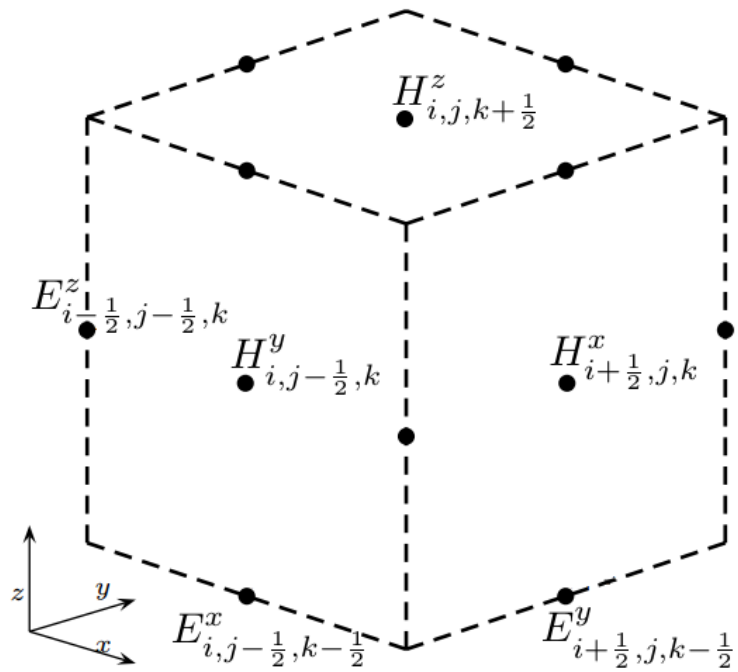

Figure 1.2: A 3D staggered grid with the discretized electric field on the edges, and the discretized magnetic field on the faces.

Finite element

Finite element (FE) methods generally use an adaptive unstructured mesh. This makes the method particularly useful for complicated geometries. FE discretization is done using an integrated average. For EM problems it is generally advisable to use edge-element (Nédélec, 1980), since these naturally enforce the tangential continuity, while allowing discontinuities in the normal direction, which is observed in EM. Finite element discretization is a general technique, where the continuous equations are recast into local equations. A standard way of doing this is by multiplying equation 1.8 with the complex conjugate of a smooth vector test function, $\boldsymbol{\phi}$, and integrating over the volume (Börner, 2010):

$$\int_\Omega \left[\sigma\partial_t \boldsymbol{e} + \nabla \times \mu^{-1}\nabla \times \boldsymbol{e}\right] \cdot \bar{\boldsymbol{\phi}} dV = \int_\Omega \partial_t \boldsymbol{j}_e \cdot \bar{\boldsymbol{\phi}} dV, \tag{1.17}$$

where Ω is the volume of interest, and $\bar{\boldsymbol{\phi}}$ is the complex conjugate of $\boldsymbol{\phi}$. Using integration by parts and the divergence theorem on the left gives:

$$\int_\Omega \left[\sigma\partial_t \boldsymbol{e} \cdot \bar{\boldsymbol{\phi}} + (\mu^{-1}\nabla \times \boldsymbol{e}) \cdot (\nabla \times \bar{\boldsymbol{\phi}})\right] dV - \int_\Gamma (\boldsymbol{n}\times\boldsymbol{\phi})\cdot(\mu^{-1}\nabla\times\boldsymbol{e}) dA = \int_\Omega \partial_t \boldsymbol{j}_e \cdot \bar{\boldsymbol{\phi}} dV \tag{1.18}$$

where Γ is the surface of Ω, and $\boldsymbol{n}$ is a normal vector to Γ. The surface integral can be removed by a clever choice of ϕ and appropriate boundary conditions (Börner, 2010). The local equations can be found by splitting the volume Ω according to each finite element:

$$\Omega = \bigcup_{i=1}^{N_e} \Omega_i, \tag{1.19}$$

with N_e being the number of elements. In a similar fashion the global electric field is expressed as local electric fields on each finite element, through a set of basis functions, $\{\boldsymbol{\psi}\}_{i=1}^{N}$

$$\boldsymbol{e} = \sum_{i=1}^{N} E_i \boldsymbol{\psi}_i \tag{1.20}$$

By setting the test functions equal to the basis functions, $\phi = \psi$ and discretizing the variables, a linear system of equations can be created based on equation 1.18:

$$\boldsymbol{M}_\sigma \partial_t \boldsymbol{u} + \boldsymbol{K}\boldsymbol{u} = \boldsymbol{f} \tag{1.21}$$

where

$$[\boldsymbol{u}]_i = E_i, \tag{1.22}$$

$$[\boldsymbol{M}]_{j,i} = \int_\Omega \sigma \boldsymbol{\phi}_i \cdot \bar{\boldsymbol{\phi}}_j dV, \tag{1.23}$$

$$[\boldsymbol{K}]_{j,i} = \int_\Omega (\mu^{-1} \nabla \times \boldsymbol{\phi}_i) \cdot \nabla \times \bar{\boldsymbol{\phi}}_j dV, \tag{1.24}$$

$$[\boldsymbol{f}]_j = \int_\Omega \partial_t \boldsymbol{J}_e \cdot \bar{\boldsymbol{\phi}}_j dV. \tag{1.25}$$

Equation 1.21-1.25 represent equation 1.8 recast to discretized localized equations using the finite element approach. Note the similarity with equation 1.16, which is the similar expression using finite difference. In Paper 2, we use the finite element method to establish the governing equations for our 2D frequency domain code.

1.2.4 Numerical optimization & parallelization

The continued growth in computational power, enables ever more realistic models, which consequently makes numerical modelling an increasingly important tool for any scientist.

Unfortunately, the growth in computational power no longer happens through an increase in the central processing units (CPU) clock rate, which would automatically result in faster models. Instead the increase happens primarily through additional cores being added to the CPU, or through an increase in a CPU's vectorization capabilities, both of which require parallelization to be

utilized. Making simulations which can utilize parallelism adds another layer of complexity to numerical programming. While some algorithms can be trivially parallelized (example: inner product of two vectors), others require a completely different approach (example: sorting algorithms (Bozidar and Dobravec, 2015)), while others still are inherently sequential and thus impossible to parallelize (example: calculate $f^{1000}(x)$.). In general sequential problems or problems with large amounts of information-transfer parallelize poorly.

Parallelization can be broadly categorized in three levels.

- Level 1, is instruction-level parallelization within a CPU.
- Level 2, is task-level parallelization within a CPU or GPU.
- Level 3, is parallelization among various computers.

Level 3 parallelization is commonly called distributed memory parallelization, such parallelization covers computers connected over a network in grids or clusters (Gropp et al., 1999), and can combine any number of systems to create almost arbitrary powerful systems. However, their communication bandwidth is rather low and comes with high latency and overhead. Level 2 is parallelization of processing units on individual systems, which can either be CPU or GPU(Dagum and Menon, 1998; Nickolls et al., 2008). Since all cores exist on the same system, communication bandwidth is usually high, while latency is low. Level 1 is instruction-parallelization and happens within a processing unit, it is commonly referred to as vectorization. Vectorization allows identical operations to be performed on multiple elements in an array at the same time. This is a very restrictive kind of parallelization in comparison to task parallelization, however it is also very fast, since the overhead is practically non-existent. In general it is advisable to start any parallelization from the lowest level, since this will best utilize the computational power of the modelling hardware. If utilized properly, parallelization (level 1 and 2) on a single modern computer can provide speedup of $\sim 500x$ (Sodani et al., 2016). Parallelization is further explained in the Technical Report, where a level 2 parallelization framework is created in OpenMP.

Chapter 2

Summary of: A review of Airborne Electromagnetic methods with focus on geotechnical and hydrological applications from 2007-2017 (Paper 1)

2.1 Introduction

Reviews provide a way of getting a holistic overview of significant advancements happening in a research area. For non-experts, reviews can provide an easy introduction to a research area, while experts can use reviews as a way of making sure they have not missed anything important in their field. Airborne electromagnetics (AEM) is an area, which has received a lot of attention in the last decade, both from within EM/geophysics community but also outside the community. Because of this, it is no surprise that several reviews detailing AEM have been made within the last decade.

On the software side: Börner (2010); Everett (2012) have made in-depth reviews of numerical EM modelling in geophysics, Smith (2014) has made a review of electromagnetic induction methods in mining, and Chang-Chun et al. (2015) have made a review of airborne electromagnetic inversion and its applications.

On the hardware side: Hardware advances are primarily driven by private enterprises, which makes it hard to find reliable peer-reviewed information. However, the academic EM geophysics community is essentially relying on data from these systems, and as such are reliant on these systems. Because of this, reviews

of survey systems are especially relevant, since they aim to offer an unbiased holistic view of an area that can otherwise be hard to gain reliable information about. Allard (2007) has made a review of helicopter transient EM systems, which we used as a foundation for the hardware chapter of our review, with the intent of extending it into the decade that has passed since it was published. Vallée et al. (2011) provide a holistic overview of the various EM systems available for mineral prospecting, while Legault (2015) gives a broad overview of the various airborne EM systems, both passive and active systems.

So while AEM has had several reviews in the last decade, none of them have been focused on groundwater exploration, or have included both the hardware and software development. We believe that the distance between the modelling community and the data gathering industry is already larger than is healthy, and being from the Aarhus HydroGeophysics Group, which was the birthplace of SkyTEM Surveys, we are in a unique position with regard to knowledge about both hardware and software.

In light of all this, our review is focused on both hardware and software, which is only natural, given the symbiotic relationship between the two.

Following the hardware and software advances, is a list of various case examples, which show the diversity and robustness of AEM methods. This list contains examples in various conditions like: deserts, permafrost regions, volcanoes, and urban areas. It involves fresh/sea-water intrusion, distinguishing various types of clay, detection of groundwater under icecaps, mapping complex buried valley networks, and huge area mappings.

2.2 Hardware

Historically, groundwater exploration and other near surface mappings, have been dominated by airborne frequency domain systems. However, with the advancements of airborne transient EM (ATEM) systems within the last two decades, this is no longer so. ATEM systems have seen significant advancement in: reliability, depth of investigation, early-time information, and overall data quality within the last decade. ATEM surveys are offered commercially by many different companies. However, most ATEM systems are designed for mineral exploration, which means the systems have been made to probe as deeply as possible. For groundwater and geotechnical exploration, the emphasis is usually not on probing as deeply as possible, instead the focus is on gathering as accurate data as possible. This requires a much more sophisticated and well-controlled survey system. In the review we go through the key characteristics required for a groundwater and geotechnical survey system, and list the systems we believe are currently suitable for these kinds of explorations.

To round off the hardware section, we look at the few system comparisons, which have been made over the last decade. Of special interest is the comparison made by Bedrosian et al. (2016), which compares several different systems thoroughly.

2.3 Software

Advancements in EM modelling and inversions are often intricately coupled. In this review, considerable time has been spent decoupling the various aspects, in order to provide as holistic an overview of EM modelling and inversion as possible.

Modelling

Modelling generally covers various ways of manipulating the governing equation resulting from Maxwell's equation. Advancements in modelling are typically done with the goal of boosting either speed or accuracy. While groundwater exploration typically involves more smoothly varying conductivity contrasts than some of the other applications of AEM, higher dimensional modelling schemes are still very relevant for groundwater exploration. This section also includes modelling of induced polarization and superparamagnetic effects, which can introduce significant errors in any near surface mapping, if not properly accounted for.

Inversion

Inversions can be done in a variety of ways. Broadly speaking, inversion techniques can be split into two groups. Those that perform a linearization in order to find a local minimum, and those that perform some kind of Monte Carlo (MC) inversion, in order to find a global or semi-global minimum. The difference between the two approaches is that a linearization approach can usually be done in $\sim 10 - 50$ iterations, while an MC inversion takes between $\sim 10^3 - 10^5$ iterations to run. Thus, MC inversions take significantly longer to perform than linearized inversions, but have the benefit of finding a global minimum, as well as being able to give more qualified uncertainties on the model parameters.

Following this, recent advancements in regularizations are introduced. This involves regularizations which tie soundings together in a quasi-2D or quasi-3D inversion (Auken and Christiansen, 2004; Viezzoli et al., 2008), as well as Lelièvre et al. (2009) where the geological interpretation is tied into the regularization.

Local meshing is introduced next, which is a way of handling large surveys, by splitting the large survey into several smaller surveys, often with overlap or communication between the smaller surveys in order to ensure some kind of continuity.

This is followed by hybrid schemes, which in our review is defined as a multi-stage process that starts with relatively cheap and inaccurate models, and while the inversion converges it progresses to more expensive and accurate modelling methods, with the goal of boosting the computational speed, while retaining the same level of accuracy, compared to traditional modelling methods.

Other advances

Some advances cannot adequately be classified as either a modelling or inversion advancement, yet are somehow significant for either.

Automated processes are crucial, both because they can significantly speed up the total time it takes to interpret data, but also because they can help remove the inevitable subjectivity that human processing and interpretation introduce on a survey. We predict that in the coming decade machine learning and automated processes will be among the key advances.

Optimizations, in this review, focuses on three distinct areas: sparse linear solvers, parallelism, and multigrid methods. EM problems tend to involve huge sparse linear problems, and especially in 2D or 3D modelling, the majority of the computational time in an EM inversion is usually spent solving linear systems. Hence, advancements in sparse linear solvers are of interest to numerical EM modelling. Parallelization is important, since most advancements in computational speed within the last decade require parallelization to be utilized. Multigrid methods involve the combination of meshes with various coarseness. The idea is that by switching between the various meshes, convergence can be achieved faster.

Finally, various advances in depth of investigation (DOI) are presented. DOI is an attempt to quantify how trustworthy the models we get through inversions are. More specifically, it involves determining the depth at which the model is data driven rather than regularization driven. We look at new DOI concepts as well as a comparison of existing schemes.

2.4 Closing remarks

AEM is developing rapidly, and thus far, nothing is indicating that this will slow down any time soon.

The vision in AEM modelling is a truly autonomous code that can take raw survey data, and produce accurate geological interpretations without any user input, in reasonable time. While this vision is far away, we have seen the coarse fundamental building blocks for such a code emerge within the last decade. What the next decade brings no one knows, but it is likely to bring us closer to that vision.

Finally, I want to mention that in the last decade, multiple open source codes have also emerged. If this trend continues, and true collaboration across universities starts, it could reshape the academic EM modelling landscape as we know it today.

Chapter 3

Summary of: An efficient 2D inversion scheme for airborne frequency domain data (Paper 2)

3.1 Introduction

1D inversions have proven themselves to be extremely fast and reliable when the geology is simple and not rapidly changing. Unfortunately, this is not always the case. Wilson et al. (2012); Yang and Oldenburg (2012) both show examples of geology, where 1D modelling is insufficient. In such cases, more advanced modelling methods are required to provide an acceptable model, with 2D modelling being the natural advancement in most cases.

Airborne EM surveys are flown as discrete lines, where the distance between soundings in a line typically range between $\sim 5 - 25$ m, while the average distance between lines are between $\sim 100 - 500$ m. For this reason, 2D modelling is often the ideal compromise between speed and accuracy for airborne EM, since 2D modelling is able to utilize the in-line information, which is very high, because of the close proximity of neighboring soundings. While 3D modelling would be capable of utilizing the cross-line information, it comes at a higher computational cost, and since the cross line information is usually sampled much coarser, the value of 3D modelling over 2D modelling is in some cases limited.

In this paper we have sought to create a code, which is capable of performing rapid 2D inversion of large scale EM data.

3.2 Methodology

The Norwegian Geotechnical Institute created a finite element 2D EM modelling code, written in C++, which has been used successfully in Marine EM modelling (Vöge, 2010). The plan was to modify this 2D code and incorporate it into AarhusInv's inversion engine (Auken et al., 2014). Initially the development was designed around ground conductivity meter (GCM) data. Since our GCM equipment (a DUALEM421S) operates at a single frequency, we believed that this would be faster than airborne frequency EM data, which usually contains 4-6 different frequencies. However, this assumption turned out to be invalid, due to the low operational altitude of the GCM equipment (0.3 m). At such low altitudes, the finite element mesh required an extremely dense meshing in order to get accurate responses.

Once this was realized, the focus was switched to airborne frequency EM modelling. Since then, a lot of effort has been made to speed-up the code, in order to reach computational speeds, which would enable survey inversion in a matter of hours/days on a modern desktop computer. One of these optimizations is the 1D/2D hybrid inversion algorithm, which gives a significant speed-up and has general applicability in higher dimensional EM modelling.

2D algorithm

Our 2D modelling approach is based on the formulation proposed by Stoyer and Greenfield (1976), commonly referred to as the 2.5D formulation. In the 2.5D formulation the earth is modelled in 2D, while the source is modelled in 3D. The source needs to be modelled in 3D in order to approximate the sources used in airborne EM reasonably.

The 2D code is discretized using adaptive finite edge-elements (Nédélec, 1980). The benefit of finite element meshing is greatest in areas with complex geometry, which are usually the areas where higher dimensional modelling provides a clear advantage over 1D modelling. By using edge-elements, it is ensured that the basis functions are divergence-free, while retaining curl. This enforces tangential continuity, while allowing discontinuities in the normal direction, which is a known property of the EM field. The governing equations are derived following the standard finite element approach, in which the global governing equations are recast into local equations using an integrated average (Monk, 2003). During the derivation, the fields are split into primary and secondary fields, where the primary field analytically models a uniform full-space air model. This separation of the fields is done to reduce numerical errors introduced by the finite element discretization. The 2D derivative calculation needed for inversion, is performed using the adjoint-state method (Plessix, 2006).

For large modern surveys it is not feasible to model everything in one large finite element mesh. From a memory perspective, the finite element mesh and the resulting equations would take up terabytes of memory, which makes it impossible to model on any modern desktop system. Even if memory was not a concern, the scalability of finite element modelling is such that it is generally

favorable to make many small finite element meshes, as opposed to one big finite element mesh, due to the quadratic scaling in computational time, with the number of finite elements. In order to enable large scale inversion, a local meshing approach was introduced (Cox et al., 2010). Survey lines are split into smaller chunks called sections. In order to preserve in-line information across sections, each section includes an overlap region into the neighboring sections, as seen in Figure 3.1. The required overlap was investigated, by performing a sensitivity analysis on various half-space models. The overlap size was chosen such that 90 % of the total signal was preserved.

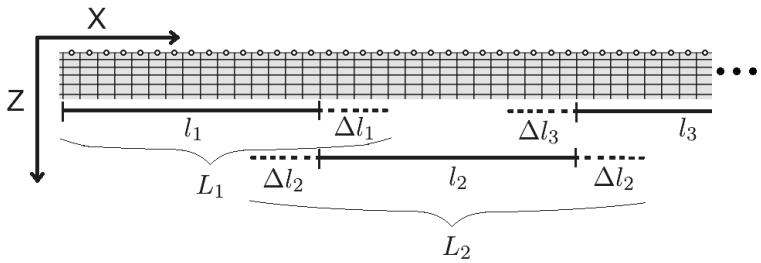

Figure 3.1: Sectioning of survey lines. Each section, L, consists of a core section, l, and overlap regions, Δl . Sections at the end of a survey line only have one overlap region, while all other sections have two overlap regions. The dots on top of the ground surface indicate the individual soundings.

The 2D algorithm was validated against AarhusInv (Auken et al., 2014) on various halfspace models, and the mesh density was set such that a misfit of less than 5 % was observed for all halfspaces.

Inversion

The inversions are done using AarhusInv's inversion engine, which is explained in full details in Auken and Christiansen (2004); Auken et al. (2014). Inversions are done on a regular grid using a linearized minimization following the Levenberg-Marquardt adaptive scheme (Pujol, 2007). The minimization is done on an objective function, which contains a misfit of both: data, prior information, and constraints. As noted in Kirkegaard and Auken (2015), AarhusInv's inversion engine scales linearly in memory and computational time, with the number of soundings. This enables all-at-once inversions even of large scale surveys.

In order to establish the 2D model parameters on the regular inversion grid, an interpolation is used. The interpolation is made trivial by incorporating the regular grid as a skeletal structure in the finite element mesh creation.

Hybrid scheme

The hybrid scheme is built on the conceptual idea of using cheaper approximate methods, in order to provide a better starting model for more computational

expensive and accurate methods. Christiansen et al. (2016) use such a method successfully in pure 1D modelling. In 2D, a similar method could be envisioned, where progressively finer meshes could be employed. However, our approach is fundamentally different, since we combine 1D and 2D modelling. 1D modelling is roughly three orders of magnitude faster than 2D modelling. Because of this, we believe our approach is superior to a pure 2D hybrid approach.

Our hybrid scheme consist of three stages:

1. 1D forward and derivative calculations
2. 2D forward, 1D derivative calculations
3. 2D forward and derivative calculations

The first stage happens practically instantaneously, since it consist of pure 1D calculations. The second stage is interesting in the fact that it combines 2D forward calculations with 1D derivative calculations. In theory such an approach has no guarantee of convergence. However, Christiansen et al. (2016) showed that as long as the forward modelling is done accurately, the derivative calculations can be somewhat inaccurate. Based on this experience, we created the second stage, which the empirical evidence shows to be working, and even if it should in some cases fail, the overall inversion will still succeed, since the second stage merely provides the starting model for the third stage. The third stage is a full 2D inversion, where convergence to a local minimum is assured. A crucial yet subtle point, is that it is suboptimal to run the first two stages to convergence. The optimal number of iterations each stage should run, was determined through empirical studies of various synthetic models. From these studies it was found that the first stage should be run for four iterations, the second stage for eight iterations, and the last stage until convergence is reached, which usually takes between 2-5 iterations.

Parallelization

The code is fully parallelized using OpenMP parallelization (Dagum and Menon, 1998), over both the sections as well as the frequencies. By making the parallelization over both, good scaling is ensured both for large surveys as well as small surveys.

3.3 Results & Discussion

Our hybrid 1D/2D code was demonstrated on various synthetic models as well as with a field example. Throughout the various examples, the hybrid code was consistently $\sim 2-6$ times faster than the pure 2D code, while producing models, with a similarly low misfit. In some cases the hybrid and 2D approach resulted in models, which were practically identical, while in other cases there were clear deviations between the models. In the case of deviations there were pros and cons with both models, as seen in Figure 3.2. In Figure 3.2 the hybrid

inversion results in a rather wide smearing zone compared to the 2D inversion, and furthermore it overshoots the conductivity on the left. On the other hand, the 2D inversion produces a rather well defined conductivity contrast, however it does produce a small artifact around 10 m depths. Looking at the data residuals the two methods perform rather equally.

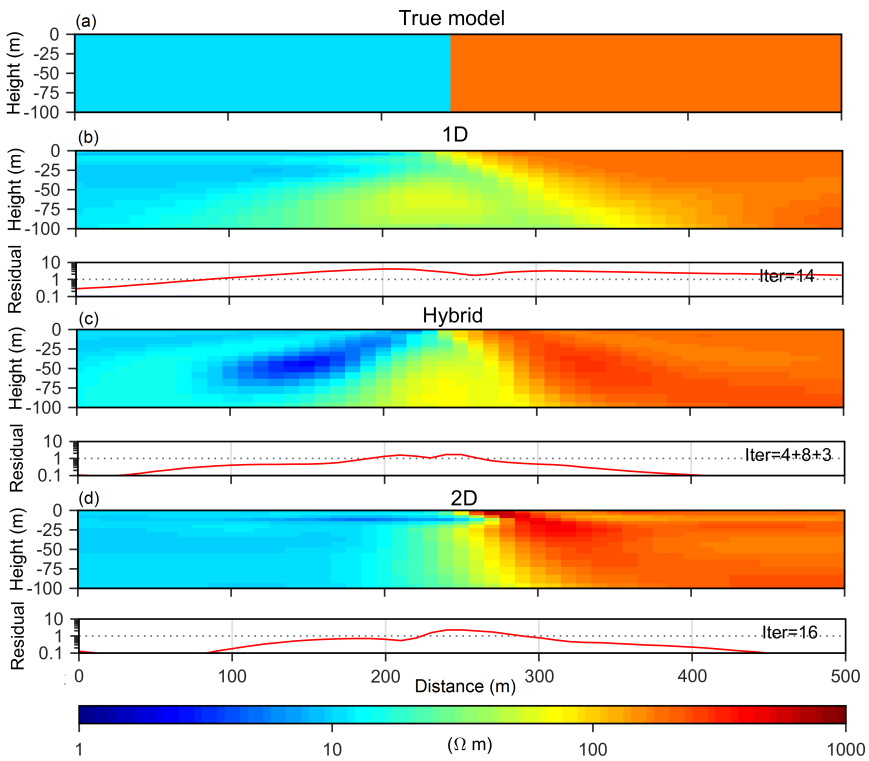

Figure 3.2: Inversion results for a horizontal conductivity contrast. (a) Illustrates the true model; the left side has a resistivity of 10 Ω m, while the right side has a resistivity of 200 Ω m. (b,c,d) Shows the earth resistivity model from a 1D/Hybrid/2D inversion, and the resulting data residual. The number of iterations until convergence is written inside the residual box.

Due to sectioning, the limiting factor for how large surveys our code can handle is the regularized all-at-once inversion approach, which we employ. However, Kirkegaard and Auken (2015) conclude that the memory consumption of AarhusInv in 1D is roughly 5 GB per 1000 line kilometers, for 19 layer models, with a sounding spacing of 25 m. In 2D this number would roughly be 10 times larger, due to the neighboring sensitivity elements present in the 2D Jacobian. Table 3.1 shows performance of our 2D code on 10k soundings, spread over 100 line km. Based on these numbers it is unlikely that the code will be used on surveys large enough for memory to become an issue.

Table 3.1: Runtime and iteration number for an inversion of a 100-line km survey conducted with the RESOLVE system. For the hybrid system, the iteration numbers and runtimes are given for each of the 3 stages.

Mode	Iterations	Runtime
1D	15	0.1h
Hybrid	$4 + 8 + 5$	36s+4.9h+26h= 31 h
2D	15	71h

Chapter 4

Summary of: A parallel computing thin sheets inversion algorithm for airborne time domain data utilizing a variable overburden (Paper 3)

4.1 Introduction

Airborne EM methods are used in a variety of places, but one of the most used places is mineral exploration (Smith, 2014). Mineral deposits have the peculiar characteristic that their conductivity is usually several orders of magnitude larger than their surrounding material. This makes mineralizations easy to detect using AEM methods, but at the same time the large conductivity contrasts also makes 1D modelling unreliable (Auken et al., 2008). In order to model these large conductivity contrasts accurately, one can either turn to higher dimensional modelling, or specialized parametric models specifically designed for such targets. While higher dimensional modelling is applicable in all cases, it is not always the smartest choice. In general, parametric modelling is much faster, and has the added benefit of drastically reducing the degrees of freedom in the model space, which usually improves convergence of the inversion, provided the parametric approximation is valid.

One of these parametric models is thin sheet modelling, where the conductive target is assumed to be reasonably modelled by a thin conductive sheet. This is often a reasonably approximation, especially if the mineralization is at least

moderately deep in the subsurface.

4.2 Methodology

The origin of our thin sheet code, can be traced back to Weidelt (1981) who derived the numerically stable theory. Zhou (1989) extended this theory and coded the foundation for the thin sheet code, which this paper describes. Since its inception, various people have upgraded the code. Today the code is capable of doing thin conductive sheet modelling and inversions, using a two-layered background model with a variable overburden. While the code is capable of modelling multiple sheets, inversions with multiple sheets have yet to be used successfully.

The code is capable of modelling both groundbased and airborne data, though its primary purpose is airborne data. It calculates the full system response following Auken et al. (2014), and includes altitude as a model parameter as suggested in Christiansen et al. (2011).

Variable overburden

The sheet is modelled in a two-layered background. In order to create this background, each sounding is assigned a 1D two-layer model. The common background model is created as a weighted average of all these 1D models, where the weight of each 1D model is proportional to the conductance of the sheet as well as the inverse square distance between the sheet and sounding. An illustration of this mapping can be seen in Figure 4.1

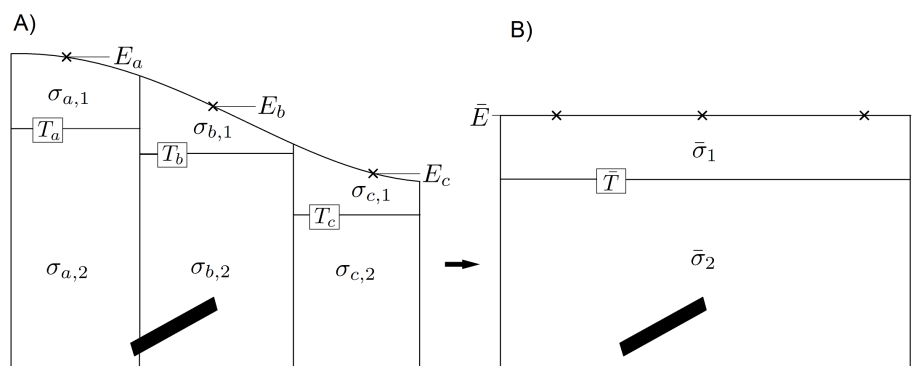

Figure 4.1: The mapping from individual 1D soundings, to an average background model used for sheet calculation. A) shows three individual 1D models, with unique: elevation, E, conductivities, σ, and thicknesses, T, for all soundings. B) shows the resulting average background model used for the sheet calculation, where all the shown parameters are now weighted mean values.

The variable overburden is included by removing the common background

response from the sheet response, and instead adding the layered 1D model response.

Inversion

Inversions are done on a regular grid using a linearized minimization following a Tikhonov regularization scheme with an L_2 norm (Engl et al., 1996):

$$\boldsymbol{m}_{n+1} = \boldsymbol{m}_n + \left(\hat{\boldsymbol{G}}_n^T \boldsymbol{C}_n^{-1} \hat{\boldsymbol{G}}_n + \lambda_n \boldsymbol{\Lambda}_n\right)^{-1} \cdot \left(\hat{\boldsymbol{G}}_n^T \boldsymbol{C}_n^{-1} \delta \hat{\boldsymbol{d}}_n\right) \tag{4.1}$$

which is similar to equation 1.14, where Λ is a diagonal scaling matrix. The diagonal scaling matrix is scaled individually for different model parameter types. The reason for this is that the different model parameter types have sensitivities that vary by several orders of magnitude, hence a uniform damping of all parameters would effectively lock certain parameters to their initial value, which is undesirable.

Optimizations

Depending on the number of cells in the sheet as well as the number of soundings; sheet modelling can take anywhere between minutes and days. As such it is imperative that the number of sheet cells is kept as low as possible and the code in general is optimized.

In order to keep the number of cells low, a dynamic cell discretization was created. With this the user specifies a desired cellsize as well as a cell-range. The cell discretization then creates approximately square cells with the desired cell size, if this results in a number of cells outside the cell-ranged, the cells are then scaled to fit within the cell-range. The cells are approximately square, since square cells provide the highest accuracy. The code also employs an adaptive frequency sampler, which helps reduce the number of sheet frequency responses needed to perform a Hankel transform back to time domain accurately. Finally, the code is fully parallelized using the latest OpenMP task directives. The parallelization is done over the frequencies, which enables a near linear scaling, provided the number of frequencies needed to be calculated are divisible by the number of threads employed.

Our sheet code has undergone rigorous validation, both against AarhusInv's 1D code (Auken et al., 2014) as well as Leroi Air (Raiche, 1998), which is a layered sheet code.

4.3 Results & Discussion

The code has been tested on various synthetic models, and its converging properties have been impressive. We show a synthetic model, containing two layers, with a conductive meadow striking through the top layer, as seen in 4.2 A). For the synthetic example a system similar to the new SkyTEM516 system was

used, with the earliest gate being at 0.22 ms. By disregarding earlier gates, we demonstrate that our code can be used not only with early-time systems. While early-time information in general is crucial for accurately mapping the underground, it is less important for sheet modelling, due to its high conductance. As seen in Figure 4.2 and Table 4.1, the inversion converges to the correct sheet, with high precision. Table 4.1 furthermore demonstrates how a similar inversion with a sheet in free-space would result. While the free-space inversion does a decent job of locating the sheet's position and shape, a clear improvement is seen when using the layered background with variable overburden.

Table 4.1: Details on the progression of the sheet parameters and the data residual during the inversion. The final sheet parameters are given for an inversion with both variable overburden and free-space. τ is the conductance of the sheet, (x, y, z) are coordinates of the center of the sheet, L_x,L_y are the length and width of the sheet, while θ, ϕ gives the strike and dip of the sheet. The standard deviation factors are determined by a linearized sensitivity analysis (Auken et al., 2014) of the parameters at the end of the inversion. Note that the data residual is normalized with the standard deviation, and 10 % noise is applied to the data.

			Variable overburden		Free-space
Sheet parameter	Starting	True	Final	STD factor	Final
τ(S)	15	30	30	1.01	24
x(m)	590	550	550	1.00	557
y(m)	510	470	469	1.00	468
z(m)	160	120	120	1.04	133
L_x(m)	100	200	200	1.01	220
L_y(m)	100	150	149	1.01	180
θ(°)	90	80	80	1.00	80
ϕ(°)	90	100	100	1.00	103
Data residual	5.56	-	0.11	-	1.6

As a field example the Valen mineral deposit in Australia is used. The Valen mineral deposit was flown with the VTEM survey system in 2011 (Eadie and Prikhodko, 2013), and was followed by two drillings, where one of the drillings located a graphite layer at around $\sim$ 90 m depth, which is believed to be responsible for the signal seen in the VTEM system. We were given access to the z component of the EM data from the VTEM survey, and used those for an inversion. Due to a combination of primary field contamination and induced polarization effects, we used a lowpass filter of 12 kHz, with a primary field damping of 90 %, and removed all gates before 0.25 ms. Much like the synthetic example, the inversion was done over three lines of data. However, in this case the mineralization was practically only visible in the central line, thus the surrounding lines merely provide constraints for the sheet, but do otherwise

not notably help determine the sheet.

With the variable background and the weighted mapping of the background, the code was able to produce acceptable inversion results from field data.

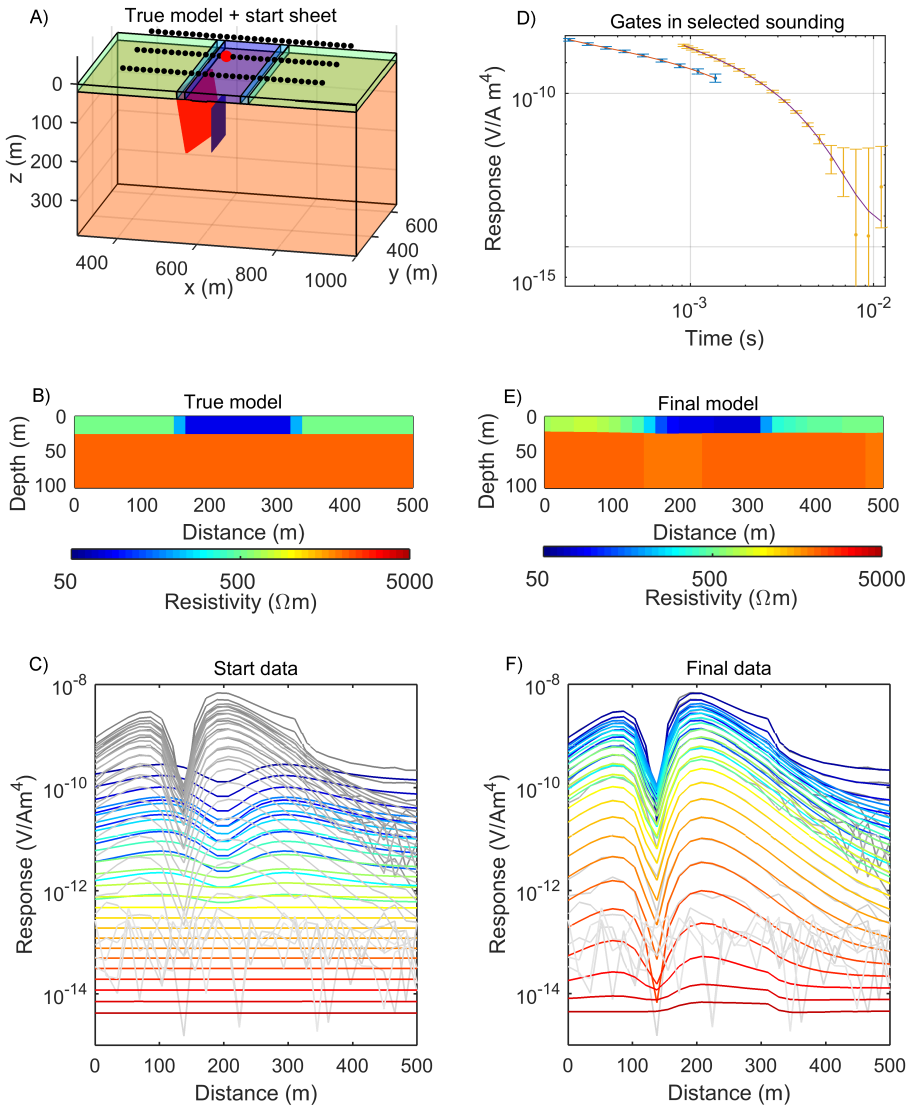

Figure 4.2: Synthetic sheet model. A) shows a 3D overview of the synthetic modelling system. The black dots indicate soundings, while the red dot is the selected sounding shown in D). The red sheet is the true sheet, while the blue sheet shows the sheet at the beginning of the inversion, (the final sheet is not shown as it coincides almost perfectly with the true sheet, see Table 2). B,E) shows the true/final resistivity model along the central flight line. C,F) shows data from all gates for all soundings in the central flight-line. Each line in the figure represents data from a particular gate shown across all soundings in the central flight-line. The grey lines are the true data, while the colored lines are the forward response from the starting/final model. D) shows the true data from a single sounding station with error bars, as well as the final forward response from the inversion. The location of the selected sounding is indicated by a red dot in A). Both high-moment (yellow) and low-moment (blue) data are shown. Note that only the z-component of the magnetic field has been used during this inversion.

Chapter 5

Summary of: A novel approach to solving the quasi-static electromagnetic problem (Paper 4)

5.1 Introduction

Common approaches to solving the quasi-static Maxwell equation in geophysical EM modelling can either be categorized as time domain approaches or frequency domain approaches. Both approaches have their pros and cons, making it case dependent which method is superior.

Time domain methods directly propagate the EM field through time, this usually results in significantly fewer calculations than a similar frequency domain calculation. One problem with this direct time domain approach is that parallelization is difficult, since the time propagation happens sequentially.

Frequency domain methods on the other hand, transform the sequential time propagation to independent frequency calculations, which are trivial to parallelize. The downside to frequency domain calculations is that they require a significant number of frequency calculations in order for the transformation back to time domain to be accurate. Börner et al. (2015) write that an accurate transformation back to time domain takes ~ 100 frequency responses, which is significantly more than the typical number of timesteppings required in time domain propagation.

In this paper we propose a novel approach, which we refer to as spectral-time approach. It relies on temporal periodic boundaries, which is effectively how EM measurements are made, when accounting for the remnant EM field from previous measurements in a stacking. The spectral-time approach performs a spectral transformation of Maxwell's equations, much like frequency domain approaches

does. The key difference is that the transformation is not to frequency domain, but rather to an optimal basis space. The result of this transformation is that each timestep propagation is transformed into exactly one, spectral-time calculation, thus the required number of calculations remain the same as in time domain. However, our method decouples the sequential timesteps, just like the frequency domain approach. Thus, the method has the benefit of both time domain and frequency domain approaches. Unfortunately, for general non-linear time propagation, the transformation back from spectral-time suffers numerical instabilities, which we have thus far been unable to overcome.

5.2 Methodology

The spectral-time method draws inspiration from the mathematical framework of circulant matrices (Gray et al., 2006), which are natural representations of propagation schemes with periodic boundaries. Though the theory is inspired by circulant matrices, it also extends beyond the propagation schemes that can be represented by circulant matrices.

By combining Maxwell's equations under the quasi-static approximation, the following is found (Haber, 2014):

$$\sigma \frac{\partial E}{\partial t} + KE = -\frac{\partial S}{\partial t}, \tag{5.1}$$

with

$$K = \nabla \times \mu^{-1} \nabla \times, \tag{5.2}$$

where σ is the conductivity, E the continuous electric field, K is the stiffness-matrix, S is the source term, and μ the magnetic permeability. The pivotal point in the derivation, is to transform the time differential into a finite difference differential, which can be expressed as a matrix $\boldsymbol{D}$, and is diagonalizable; such that it can be decomposed into an eigenvector matrix $\boldsymbol{V}$ and a diagonal eigenvalue matrix $\boldsymbol{\Lambda}$:

$$\boldsymbol{D} = \boldsymbol{V}\boldsymbol{\Lambda}\boldsymbol{V}^{-1}. \tag{5.3}$$

By utilizing this property, the quasi-static Maxwell equation can be discretized into:

$$(\lambda_i \boldsymbol{M_\sigma} + \boldsymbol{K})\bar{\boldsymbol{e}}_i = -\lambda_i \bar{\boldsymbol{s}}_i, \tag{5.4}$$

where i are the various timesteps, λ_i is the i'th diagonal element in $\boldsymbol{\Lambda}$, $\bar{\boldsymbol{e}}_{\boldsymbol{i}}$,$\bar{\boldsymbol{s}}_{\boldsymbol{i}}$ are the spectrally transformed discrete electric field and discrete source current for the i'th timestep, and $\boldsymbol{M_\sigma}$ is the discretized isotropic version of σ, commonly referred to as the mass-matrix.

For each timestep equation 5.4 forms a linear equation, which is decoupled from all other timesteps. The recoupling comes when the inverse spectral transform is applied in order to bring the electric field back to time domain. Coincidently, this is also where the numerical instability occurs. The instability is associated with the finite difference propagation method, and occurs because $\boldsymbol{D}$ is nearly singular, and thus $\boldsymbol{V}^{-1}$ is numerically unstable, which is the matrix used for applying the inverse spectral transform.

5.3 Results & Discussion

For linear timestepping with first order backward differential formula (BDF1), the propagation matrix looks like:

$$\boldsymbol{D} = \frac{1}{\Delta t} \begin{pmatrix} 1 & -1 & & & \\ & 1 & -1 & & \\ & & \ddots & \ddots & \\ & & & 1 & -1 \\ -1 & & & & 1 \end{pmatrix}, \tag{5.5}$$

where Δt is the constant timestep length. In this case, $\boldsymbol{D}$ is a circulant matrix, and thus its eigenvectors and eigenvalues are known analytically. Using this, the theory was validated against time domain propagation with Maxwelltime, which is an open source EM modelling extension of the code presented in Ruthotto et al. (2016). Figure 5.1 shows how propagation in time domain converges to the same EM field as the spectral-time method given enough initiating cycles to build up temporal periodic boundaries.

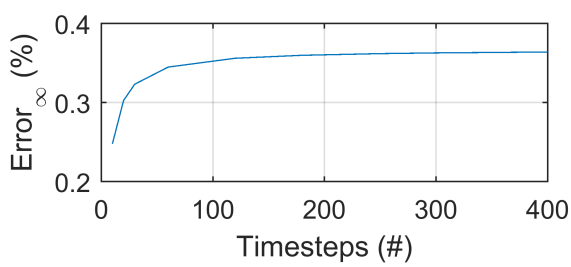

Figure 5.1: Shows the infinity norm deviation between propagation in time domain and the spectral-time method, as a function of the number of timesteps.

The fact that it works for linear timestepping shows that the theory is valid. However, in order to be a serious contender to the standard approaches of time/frequency propagation, a stable non-linear timestepping approach needs to be found. In the remainder of the article various different propagation schemes are tried, with logarithmic as well as uneven timestepping. Unfortunately, none of the approaches were able to circumvent the instability encountered in the eigendecomposition of the propagation matrix. It is possible that this may be an inherent instability, when moving beyond linear timestepping. However, if this is the case, we have been unable to prove it. Thus, this article ends with an open question to the scientific community, and we hope that others find the approach interesting and see the potential in investigating it further. Does a stable numerical solution exist for non-linear timestepping, or can anyone prove that such solutions cannot exist?

Chapter 6

Summary of: Numerical tools and optimizations for EM geophysical methods (Technical Report)

6.1 Introduction

This section is deliberately short to minimize repetitiveness with regards to the introductory chapter.

Numerical modelling often uses high-speed languages to make the code run as fast as possible. However, high-speed languages are mostly useless, if the programmer does not know how to create optimized algorithms. Writing optimized code takes time and requires intricate knowledge about both the numerical algorithm being designed, as well as the hardware on which it is meant to run on. Furthermore, there is always a balance between the amount of speed-up an optimization can give contra the time it takes to implement, and the additional complexity added to future maintenance of the code. Some optimizations are easy to implement and hardly worth mentioning, yet without intricate knowledge about the number of clock cycles various mathematical operations take, it is for instance tempting to expect multiplication and division to be roughly equal in speed, which is not the case. Other optimizations, like parallelization, are often complicated to implement. However, given that parallelization alone can speed up a program $\sim 500x$ on a modern CPU designed for numerical modelling (Sodani et al., 2016), it is in many cases worth implementing.

In this technical report I present an OpenMP parallelization framework that I have created during my PhD studies, and which is currently used in AarhusInv (Auken et al., 2014). Furthermore, I present a block-parallel sparse iterative linear solver that I created in the early parts of my PhD studies, which is also

used in AarhusInv. Both tools can be obtained from the HydroGeophysics Group at Aarhus University.

6.2 Parallel framework

Parallelization is becoming increasingly crucial for any numerical code, yet the technology is still heavily under development and the tools available are relatively primitive in many programming languages.

As a means to remedy this, I created our own OpenMP parallelization framework, with the following goals:

- Portability - make the code run optimally on various different systems and architectures (NUMA/UMA/Hyperthreading).
- Make the code run well on both shared and dedicated servers.
- Enable autonomous parallelization, as well full control for the expert user.
- Create a simple, yet general parallelization structure that can contain all our previously used parallelization schemes.
- Create a single parallelization module that contains all parallelization information, and sets all the global OpenMP directives needed, such that the general developer should never set these global directives manually.
- Create a dynamic parallelization structure, which removes the need for having multiple copies of the same routines for various degrees of parallelization.

These goals were created, based on the problems we observed in our code beforehand. Since the framework's inception, it has now been implemented in AarhusInv for well over a year, and has made the number of parallelization issues we experience significantly fewer, while making the autonomous parallelization that most non-expert users desire more optimized.

The parallelization framework works as a standalone module, and is released as open source for anyone to use or modify as they see fit. The module supports both nested and non-nested parallelization, and furthermore has the option of setting a different number of threads for memory-bandwith limited regions.

6.3 Sparse linear solvers

Many approaches to numerical modelling involves discretizing and transforming complicated equations into large systems of linear equations. For this reason, it is generally of high importance to be able to efficiently solve large systems of linear equations. In airborne electromagnetics the systems of linear equations are sparse, but can reach millions of equations and unknowns (Kirkegaard and Auken, 2015).

In order to handle such large linear systems, we have developed a custom built sparse iterative linear solver. The reason why we built our own linear solver is that AEM inversions lead to large sparse linear systems, with a characteristic structure, and by building our own linear solver, we are able to utilize this particular structure to gain good parallel scaling. Furthermore, a custom built solver allows all the tuning parameters to be optimally tweaked for our particular type of problem. One of the key features of our linear systems is that they are built based on reverse-Cuthill-Mckee (RCM) reordered soundings (Cuthill and McKee, 1969). This means that our linear systems cluster interacting soundings closely together, while retaining the individual sounding structure. The result of this is a linear system, which can more effectively be factorized due to the non-zero elements close proximity to the diagonal, as can be seen in Figure 6.1.

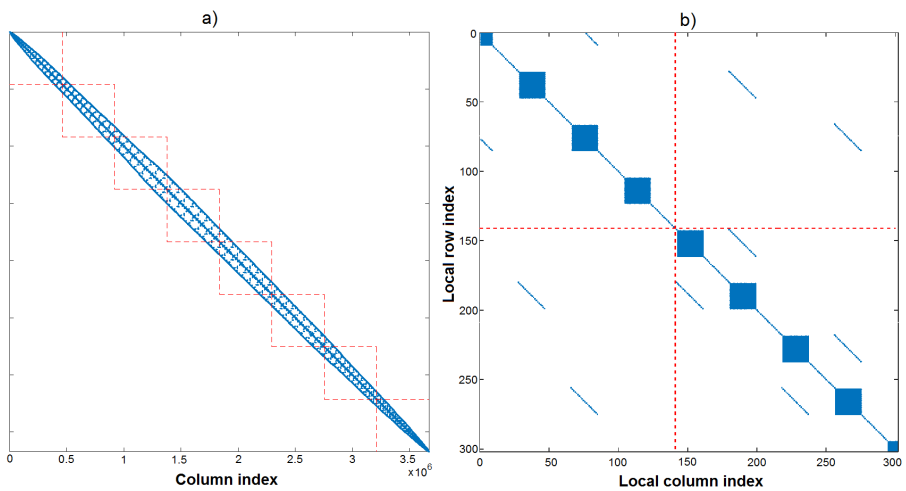

Figure 6.1: Characteristic matrix sparsity pattern. Non-zero elements of the matrix are shown as blue dots, while the striped red lines indicate block-splitting boundaries. a) shows a disjointed block-splitting b) shows a zoom-in near a block boundary. The filled blue squares near the diagonal represent data from individual soundings, while the off-diagonal blue lines represent constraints between soundings.

Our solver is iterative, and uses conjugate-gradient (CG) propagation (Hestenes and Stiefel, 1952), since this is both a fast and stable propagation routine. On top of the implicit RCM reordering, we furthermore employ the following optimization steps: the diagonal elements are normalized before starting the CG propagation, and during the propagation a preconditioner is used, which is either an incomplete Cholesky factorization or a symmetric Gauss-Seidel preconditioner, depending on the average diagonal dominance of the linear system. Since the linear system is RCM sounding reordered, the system can be split into disjointed blocks without any overlap, as seen in Figure 6.1. While this does

lose all the information outside the blocks during the preconditioning. It turns out that this information is not vital for solving the system of equations, though it does worsen the iterative convergence rate as seen in Figure 6.2 c).

A comparison of our solver with the well-known commercial solver Pardiso (Schenk et al., 2000) can be seen in Figure 6.2. The figure shows how our solver scales super-linearly with the number of threads, and how this results in our solver being faster than Pardiso, for large numbers of threads. The reason why Pardiso scales so poorly is that it performs a zero'th order reordering before factorization, which does not appear to be parallelized very effectively.

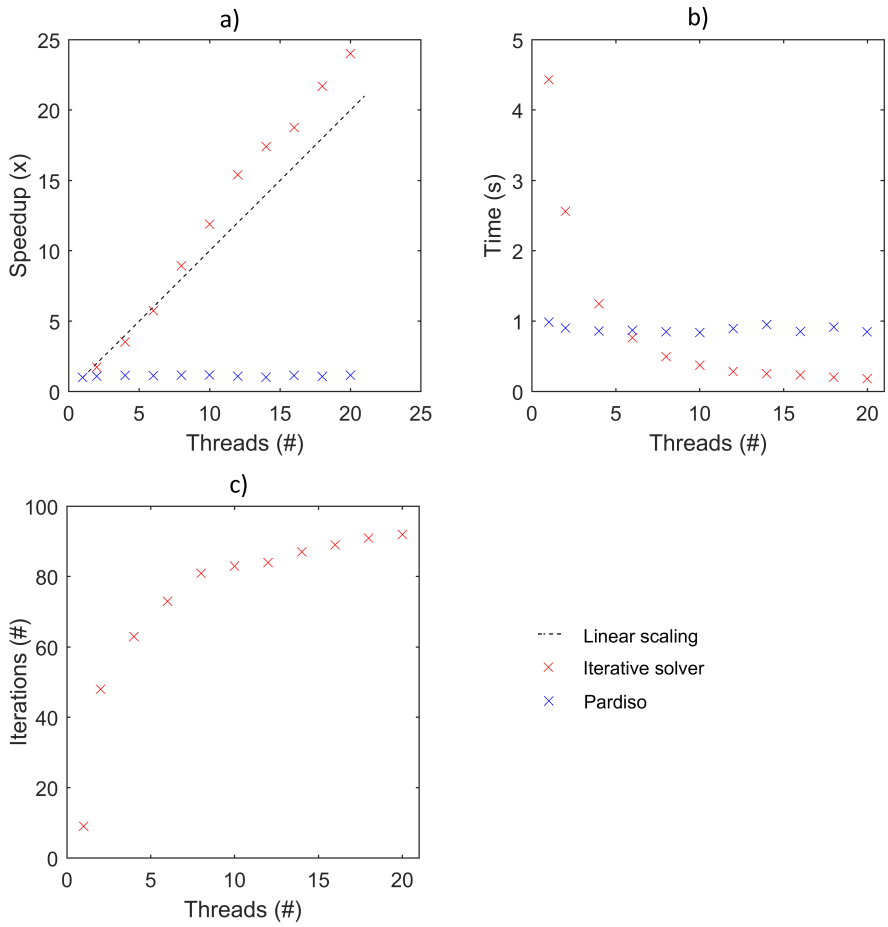

Figure 6.2: Benchmarking the iterative solver, on a system with a matrix containing $\sim 42k$ rows and columns, with $\sim 500k$ elements. a) shows the speedup of the iterative solver and Pardiso. While the iterative solver reaches super-linear scaling, Pardiso scales very poorly. b) shows solving time as a function of threads. Pardiso is faster for low thread numbers, but because of its poor scaling the iterative solver outscales it around six threads. c) shows the number of propagation required for the iterative solver to reach convergence as a function of number of threads.

Chapter 7

Discussion and Outlook

In a time when the world is facing an imminent global fresh water crisis, the AEM method has developed to a point, where it will likely be the most important mapping tool to counteract the crisis on a global scale. While groundwater exploration is one usage of the AEM method, the current state of AEM enables the method to be used in a variety of other areas, with more areas likely to come as the method is further refined in the coming decades.

The interpretive software has shown some impressive advancements, but most of these advancements are still at a scientific-proof-of-concept level. As documented in Paper 1, the geophysical EM community has shown that EM modelling and inversion of AEM data works, both in: 1D, 2D, 3D, and through parametrizations. While new modelling methods can certainly arise, like the one suggested in Paper 4, and likely will; I believe that a more crucial thing for the general advancement of AEM at this point, is to develop an all encompassing open source code. This job is likely too big a challenge for any one scientific group, and in order to become a success it would need the collaboration of several groups. At the moment, I believe the codes that are closest to reaching such a goal are: AarhusInv (Auken et al., 2014), SimPEG (Cockett et al., 2015), and the EM modules based on Haber and Schwarzbach (2014) and built on top of jInv (Ruthotto et al., 2016). AarhusInv is likely still the leading scientific code, when it comes to robust large-scale EM mapping. Their code has been steadily developed over more than two decades, and has the distinct advantage that it is developed closely with SkyTEM, meaning that their code understands and accounts for the the subtle intricacies coming from the surveying hardware, and includes the full system transfer function. The code is specialized in 1D modelling, but is also capable of 2D modelling. It can perform quasi-2D and quasi-3D inversion, through the use of lateral constraints (Auken and Christiansen, 2004), or spatial constraints (Viezzoli et al., 2008), which both enable large scale inversions. While the age of the code certainly brings it maturity, it unfortunately also means that parts of the code are written with old obscure coding practices, which will likely need to be refactored if any significant changes are to be made. Furthermore the code is not open source, which makes any joint collaboration

unlikely, though it is freely available for any scientific group. While AarhusInv may be the most robust and leading code for large-scale EM mapping, SimPEG and the EM modules built on top of jInv (Ruthotto et al., 2016) are new open source projects, which show huge potential, and will be formidable codes once they reach full maturity. SimPEG already contains 1D, 2D, and 3D modelling, as well as a Gaussian parametrization (McMillan et al., 2015), however they are lacking large-scale support, as well as the inclusion of the full system transfer function. This makes their code great for synthetic studies and teaching purposes, but makes it lacking in applicability on field data. However, given the short time these codes have thus far existed, and their current development trend, they are likely to remedy this rather soon.

In a world where computer power is growing to a point that 3D modelling and inversions are becoming possible, it is tempting to ask why 1D modelling is relevant. However, 1D modelling is still an invaluable first approach tool, and has a variety of uses even in recent advancements. Ullmann et al. (2016); Scheunert et al. (2016) demonstrate how a 1D code can be combined with a higher dimensional code in an automated process, where everything is initially modelled in 1D; areas where the 1D modelling proves insufficient are then automatically remodelled using a higher dimensional code. Such an approach could naturally be combined with the hybrid approach presented in Paper 2, and would be another way that higher dimensional codes can benefit from accurate lower dimensional modelling codes. In an ideal code, the dimensionality does not even have to be specified, but is rather automatically determined throughout the whole survey and increasingly made more accurate until sufficiently accurate.

One key issue, I have thus far found in the AEM community is that comparisons of different methods are either not done at all, or are often done subjectively and biased. This is especially true for the data gathering hardware, where the only independent unbiased comparison of any of the modern HTEM systems were done by Bedrosian et al. (2016). Companies have also made these comparisons themselves, but as is evident in the comparison of SkyTEM Surveys (Effersø and Sørensen, 2013) and Geotech (Eadie and Prikhodko, 2013) over the Valen deposit in Australia, the companies are more interested in promoting their system, than they are in presenting an objective comparison of their systems. The result is that both companies conclude their system to be the superior system, highlighting all the areas where their system is superior, while neglecting to mention the areas where their system falls short. While such behaviour is sadly somewhat expected from companies, this behaviour is also somewhat present within the scientific community.

One area where I been curious to see such a comparison for years, is among the various parametrized codes. Paper 3 presents, as far as I am aware, the first thin conductive sheet code, with an AEM field example. I believe a future comparison between this thin sheet code and the modern parametrization approach made by McMillan et al. (2015) could be very interesting, and likely illuminate both methods areas of strengths and weaknesses.

Irregardless of the future of AEM and its interpreting software, the future

of computers in general is likely to make parallelization ever more crucial to any high performance code. Maybe, this future will also bring efficient tools for parallelization. During my PhD studies such tools were limited and buggy in Fortran, and because of this I developed our own parallelization framework as documented in Technical Report.

Near surface EM modelling is currently a very interesting research area, which is rapidly developing and combines scientific research with practical applications in a most fascinating way. During my PhD studies I have tried to keep my work as general as possible, in the hope that some of the work I have done during my PhD studies, can be beneficial to others.

Chapter 8

Bibliography

Allard, M. (2007). On the origin of the htem species. In *Proceedings of exploration*, volume 7, pages 355–374.

Auken, E. and Christiansen, A. V. (2004). Layered and laterally constrained 2d inversion of resistivity data. *Geophysics*, 69(3):752–761.

Auken, E., Christiansen, A. V., Jacobsen, L. H., and Sørensen, K. I. (2008). A resolution study of buried valleys using laterally constrained inversion of tem data. *Journal of Applied Geophysics*, 65(1):10–20.

Auken, E., Christiansen, A. V., Kirkegaard, C., Fiandaca, G., Schamper, C., Behroozmand, A. A., Binley, A., Nielsen, E., Effersø, F., Christensen, N. B., et al. (2014). An overview of a highly versatile forward and stable inverse algorithm for airborne, ground-based and borehole electromagnetic and electric data. *Exploration Geophysics*, 46(3):223–235.

Barfod, A. A., Møller, I., and Christiansen, A. V. (2016). Compiling a national resistivity atlas of denmark based on airborne and ground-based transient electromagnetic data. *Journal of Applied Geophysics*, 134:199–209.

Bedrosian, P. A., Schamper, C., and Auken, E. (2016). A comparison of helicopter-borne electromagnetic systems for hydrogeologic studies. *Geophysical Prospecting*, 64(1):192–215.

Börner, R.-U. (2010). Numerical modelling in geo-electromagnetics: advances and challenges. *Surveys in Geophysics*, 31(2):225–245.

Börner, R.-U., Ernst, O. G., and Güttel, S. (2015). Three-dimensional transient electromagnetic modelling using rational krylov methods. *Geophysical Journal International*, 202(3):2025–2043.

Bozidar, D. and Dobravec, T. (2015). Comparison of parallel sorting algorithms. *arXiv preprint arXiv:1511.03404*.

Chang-Chun, Y., Xiu-Yan, R., Yun-He, L., Yan-Fu, Q., Chang-Kai, Q., and Jing, C. (2015). Review on airborne electromagnetic inverse theory and applications. *Geophysics*, 80(4):W17–W31.

Chongo, M., Christiansen, A. V., Fiandaca, G., Nyambe, I. A., Larsen, F., and Bauer-Gottwein, P. (2015). Mapping localised freshwater anomalies in the brackish paleo-lake sediments of the machile–zambezi basin with transient electromagnetic sounding, geoelectrical imaging and induced polarisation. *Journal of Applied Geophysics*, 123:81–92.

Christensen, N. B. (1990). Optimized fast hankel transform filters. *Geophysical Prospecting*, 38(5):545–568.

Christiansen, A. V., Auken, E., Kirkegaard, C., Schamper, C., and Vignoli, G. (2016). An efficient hybrid scheme for fast and accurate inversion of airborne transient electromagnetic data. *Exploration Geophysics*, 47(4):323–330.

Christiansen, A. V., Auken, E., and Viezzoli, A. (2011). Quantification of modeling errors in airborne tem caused by inaccurate system description. *Geophysics*, 76(1):F43–F52.

Cockett, R., Kang, S., Heagy, L. J., Pidlisecky, A., and Oldenburg, D. W. (2015). Simpeg: An open source framework for simulation and gradient based parameter estimation in geophysical applications. *Computers & Geosciences*, 85:142–154.

Cox, L. H., Wilson, G. A., and Zhdanov, M. S. (2010). 3d inversion of airborne electromagnetic data using a moving footprint. *Exploration Geophysics*, 41(4):250–259.

Cuthill, E. and McKee, J. (1969). Reducing the bandwidth of sparse symmetric matrices. In *Proceedings of the 1969 24th national conference*, pages 157–172. ACM.

Dagum, L. and Menon, R. (1998). Openmp: an industry standard api for shared-memory programming. *IEEE computational science and engineering*, 5(1):46–55.

Doll, W. E., Gamey, T. J., Beard, L. P., Sheehan, J. R., and Norton, J. (2008). Advances in airborne geophysical systems for ordnance mapping and detection. *The Leading Edge*, 27(11):1463–1469.

Eadie, T. and Prikhodko, A. (2013). Vtem - skytem survey comparison over valen cu-ni deposit.

Effersø, F. and Sørensen, K. (2013). Skytem case study: The valen survey comparison with vtem.

Engl, H. W., Hanke, M., and Neubauer, A. (1996). *Regularization of inverse problems*, volume 375. Springer Science & Business Media.

Everett, M. E. (2012). Theoretical developments in electromagnetic induction geophysics with selected applications in the near surface. *Surveys in geophysics*, 33(1):29–63.

Gray, R. M. et al. (2006). Toeplitz and circulant matrices: A review. *Foundations and Trends® in Communications and Information Theory*, 2(3):155–239.

Gropp, W., Lusk, E., and Skjellum, A. (1999). *Using MPI: portable parallel programming with the message-passing interface*, volume 1. MIT press.

Haber, E. (2014). *Computational methods in geophysical electromagnetics*. SIAM.

Haber, E. and Ascher, U. M. (2001). Fast finite volume simulation of 3d electromagnetic problems with highly discontinuous coefficients. *SIAM Journal on Scientific Computing*, 22(6):1943–1961.

Haber, E. and Schwarzbach, C. (2014). Parallel inversion of large-scale airborne time-domain electromagnetic data with multiple octree meshes. *Inverse Problems*, 30(5):055011.

Hestenes, M. R. and Stiefel, E. (1952). *Methods of conjugate gradients for solving linear systems*, volume 49. NBS.

Høyer, A.-S., Jørgensen, F., Sandersen, P., Viezzoli, A., and Møller, I. (2015). 3d geological modelling of a complex buried-valley network delineated from borehole and aem data. *Journal of Applied Geophysics*, 122:94–102.

Kirkegaard, C. and Auken, E. (2015). A parallel, scalable and memory efficient inversion code for very large-scale airborne electromagnetics surveys. *Geophysical Prospecting*, 63(2):495–507.

Legault, J. M. (2015). Airborne electromagnetic systems–state of the art and future directions. *CSEG Recorder*, 40(06):38–49.

Lelièvre, P. G., Oldenburg, D. W., and Williams, N. C. (2009). Integrating geological and geophysical data through advanced constrained inversions. *Exploration Geophysics*, 40(4):334–341.

McMillan, M. S., Schwarzbach, C., Haber, E., and Oldenburg, D. W. (2015). 3d parametric hybrid inversion of time-domain airborne electromagnetic data. *Geophysics*, 80(6):K25–K36.

Monk, P. (2003). *Finite element methods for Maxwell's equations*. Oxford University Press.

Nédélec, J.-C. (1980). Mixed finite elements in r3. *Numerische Mathematik*, 35(3):315–341.

Nickolls, J., Buck, I., Garland, M., and Skadron, K. (2008). Scalable parallel programming with cuda. *Queue*, 6(2):40–53.

Pedersen, J. B., Schaars, F. W., Christiansen, A. V., Foged, N., Schamper, C., Rolf, H., and Auken, E. (2017). Mapping the fresh-saltwater interface in the coastal zone using high-resolution airborne electromagnetics. *First Break*, 35(8):57–61.

Pfaffhuber, A. A., Lysdahl, A. O., Sørmo, E., Skurdal, G. H., Thomassen, T., Anschütz, H., and Scheibz, J. (2017). Delineating hazardous material without touchingaem mapping of norwegian alum shale. *First Break*, 35(8):35–39.

Plessix, R.-E. (2006). A review of the adjoint-state method for computing the gradient of a functional with geophysical applications. *Geophysical Journal International*, 167(2):495–503.

Pujol, J. (2007). The solution of nonlinear inverse problems and the levenberg-marquardt method. *Geophysics*, 72(4):W1–W16.

Raiche, A. (1998). Modelling the time-domain response of aem systems. *Exploration Geophysics*, 29(1/2):103–106.

Ruthotto, L., Treister, E., and Haber, E. (2016). jinv–a flexible julia package for pde parameter estimation. *arXiv preprint arXiv:1606.07399*.

Schenk, O., Gärtner, K., and Fichtner, W. (2000). Efficient sparse lu factorization with left-right looking strategy on shared memory multiprocessors. *BIT Numerical Mathematics*, 40(1):158–176.

Scheunert, M., Ullmann, A., Afanasjew, M., Börner, R.-U., Siemon, B., and Spitzer, K. (2016). A cut-&-paste strategy for the 3-d inversion of helicopter-borne electromagnetic datai. 3-d inversion using the explicit jacobian and a tensor-based formulation. *Journal of Applied Geophysics*, 129:209–221.

Smith, R. (2014). Electromagnetic induction methods in mining geophysics from 2008 to 2012. *Surveys in Geophysics*, 35(1):123–156.

Sodani, A., Gramunt, R., Corbal, J., Kim, H.-S., Vinod, K., Chinthamani, S., Hutsell, S., Agarwal, R., and Liu, Y.-C. (2016). Knights landing: Second-generation intel xeon phi product. *Ieee micro*, 36(2):34–46.

Stoyer, C. and Greenfield, R. J. (1976). Numerical solutions of the response of a two-dimensional earth to an oscillating magnetic dipole source. *Geophysics*, 41(3):519–530.

Ullmann, A., Scheunert, M., Afanasjew, M., Börner, R.-U., Siemon, B., and Spitzer, K. (2016). A cut-&-paste strategy for the 3-d inversion of helicopter-borne electromagnetic dataii. combining regional 1-d and local 3-d inversion. *Journal of Applied Geophysics*, 130:131–144.

Vallée, M. A., Smith, R. S., and Keating, P. (2011). Metalliferous mining geophysicsstate of the art after a decade in the new millennium. *Geophysics*, 76(4):W31–W50.

Viezzoli, A., Christiansen, A. V., Auken, E., and Sørensen, K. (2008). Quasi-3d modeling of airborne tem data by spatially constrained inversion. *Geophysics*, 73(3):F105–F113.

Vöge, M. (2010). ngi25em version 4.0 user documentation. Technical report, Norwegian Geotechnical Institute.

Vöge, M., Pfaffhuber, A., Auken, E., Kirkegaard, C., Boesen, T., Hendricks, S., and Hunkeler, P. (2015). 2.5 d inversion of sea ice thickness from helicopter em data. In *First European Airborne Electromagnetics Conference*.

Ward, S. H. and Hohmann, G. W. (1988). Electromagnetic theory for geophysical applications. In *Electromagnetic methods in applied geophysics*, volume 1, pages 131–311.

Weidelt, P. (1981). Report on dipole induction by a thin plate in a conductive halfspace with an overburden: Fed. *Inst. Earth Sci. and Mate. Report*, 89727.

Wilson, G. A., Cox, L. H., Čuma, M., and Zhdanov, M. S. (2012). Inverting airborne geophysical data for mega-cell and giga-cell 3d earth models. *The Leading Edge*, 31(3):316–321.

Yang, D. and Oldenburg, D. W. (2012). Three-dimensional inversion of airborne time-domain electromagnetic data with applications to a porphyry deposit. *Geophysics*, 77(2):B23–B34.

Yee, K. (1966). Numerical solution of initial boundary value problems involving maxwell's equations in isotropic media. *IEEE Transactions on antennas and propagation*, 14(3):302–307.

Zhdanov, M., Cox, L., and Rudd, J. (2013). Paradigm change in 3d inversion of airborne em surveys: Case study for oil sands exploration near fort mcmurray, alberta. *First Break*, 31(4).

Zhou, Q. (1989). Audio-frequency electromagnetic tomography for reservoir evaluation. Technical report, Lawrence Berkeley Lab., CA (USA).

Appendix A

Paper 1

Submitted and accepted by Advances in Geophysics.

2017

A review of Airborne Electromagnetic methods with focus on geotechnical and hydrological applications from 2007-2017

ESBEN AUKEN, TUE BOESEN, ANDERS VEST CHRISTIANSEN

1. Contents

1. Contents 1
2. Pretext 2
3. Introduction 2
4. AEM systems – Hardware 3
Advancements in the last decade 5
Depth of investigation 5
Surface resolution 6
Current state of AEM systems 7
Frequency domain systems 7
Time domain systems 8
System comparison studies 10
5. Software 10
Modelling 10
1D Modelling 10
2D Modeling 11
3D Modelling 11
Induced polarization and superparamagnetic effects 12
Inversion 14
Objective functions 14
Minimization schemes 14
Regularizations 17
Local mesh 19
Hybrid schemes 19
Other advances 20
Automated processes 20
Optimizations 20
Depth of investigation 22
6. Case examples 23
Finding quick clay 23
Delineating hazardous material 23
Mapping the fresh-saltwater interface 23
Deep groundwater mapping in Antarctica 24
3D geological modelling of complex buried-valleys 24

Environmental assessments and hydrologic mapping in Africa 25
Measurements of a collapse-prone volcano 26
7. Conclusion & Outlook 27
8. Bibliography 28

2. Pretext

The purpose of this review is to report the major advancements that have been made within the area of airborne electromagnetics (AEM) between 2007 and 2017, with a focus on geotechnical and hydrological applications. Older articles will be listed in order to provide context for recent advancement, or when describing the underlying methodology.

The review is structured such that each section can be read independently, and each section starts out with a brief introduction to establish a common ground.

References are inserted where relevant, and as such some articles are cited multiple times, since they are relevant in multiple sections.

3. Introduction

Electromagnetic (EM) methods are among the most important tools we have for exploring the subsurface. Among the geophysical EM methods, no area has seen more advancement within the last decade than airborne EM (AEM) systems and the accompanying interpreting software (interpretive software in this context includes numerical modelling codes). Applications are wide-spread and they range from regional scale groundwater studies and mineral exploration to mapping of thin shallow layers or location of unexploded ordnance. AEM methods have been used for groundwater and geotechnical studies for several decades, but lately, worldwide recognition of the importance of the method has increased greatly. One reason for this is the maturity of hardware systems, which are now capable of providing accurate and low-bias data. This can be used in the increasingly sophisticated interpretation software solutions developed within the last decade, which when combined with high quality data have been able to produce impressive results.

Now and in the future the world will face wide-spread fresh water scarcity, which is starting to be generally acknowledged, and currently AEM methods are the only viable approach to provide mapping solutions to address these problems on a global scale. In light of this, we believe AEM will be a crucial method in the future, and likely the most important investigative method for groundwater management.

The purpose of this review is to give the reader an overview of the AEM area, from a geotechnical and groundwater perspective. The technologies, both hardware and interpretive software, have developed so rapidly that even among scientists and professionals, very few have a complete overview of the state of AEM technologies and their areas of applicability.

Hardware and interpretive software developments are in a symbiotic relationship. However, very few people are experts in both areas and this knowledge-gap gives disjointed development to the detriment of both areas, which is something we hope to help mend with this review. Hardware development is as important as software development, and both need to be understood in order to fully utilize the capabilities of the AEM method.

Hand in hand with the development in computer power and AEM hardware, operational 3D modelling and inversions codes for transient EM data now exist, and some even in open source. Thanks to local meshing technologies, 3D codes are capable of handling large surveys in principle. However, the computational demands for modelling a full AEM survey are still so large, that only a few companies do this in practice.

4. AEM systems – Hardware

AEM systems include any airborne system that uses inductive electromagnetics to measure the earth's resistivity. Examples of helicopter transient EM (HTEM) and helicopter frequency EM (HFEM) systems can be seen in Figure 1. While the systems may look simple, successfully designing such systems has proven quite an engineering challenge.

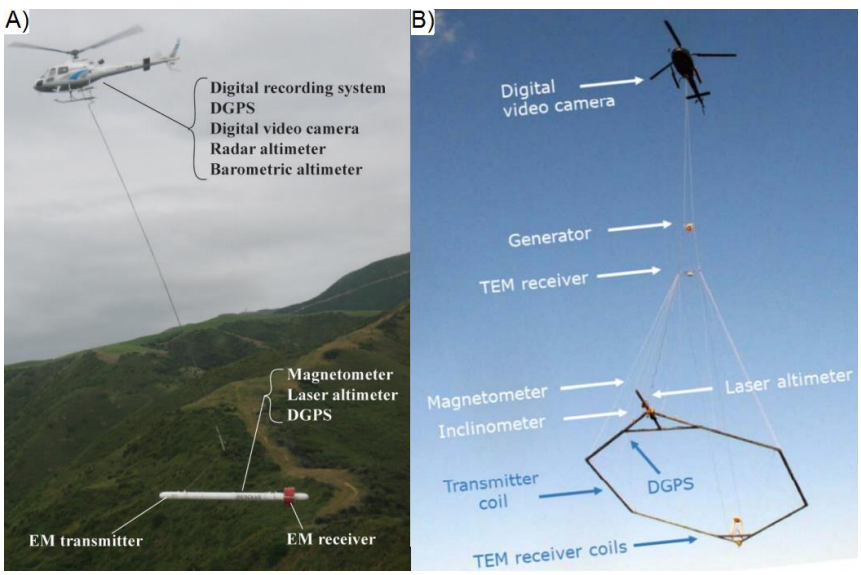

Figure 1 Examples of Helicopter AEM systems. A) shows the RESOLVE frequency EM system, Source: (Ball et al. 2011). B) shows a SkyTEM transient EM system (courtesy of SkyTEM Surveys).

AEM systems have seen tremendous advancements within the last decade, and with these advancements, more applications have been unlocked. While software development is primarily driven by academics, hardware development is almost exclusively driven by private enterprises. This means that hardware development is less transparent and in many cases, information is not readily available in scientific publications, but has to be found on homepages or in conference proceedings.

Traditionally, AEM systems are first categorized as either frequency domain (FEM) or time domain systems (TEM), depending on whether they do constant measurements at a few select frequencies, see Figure 2 A), or they fire discrete electromagnetic pulses and measure their decay curves, see Figure 2 B). Historically, airborne FEM (AFEM) systems are considered to have a better resolution in the near surface, but a lower depth of investigation compared to airborne TEM (ATEM) systems. Within the last decade however, the

heavy development in ATEM systems have made their near surface resolution sufficiently accurate such that modern ATEM systems are able to resolve the shallow surface as well as AFEM systems.

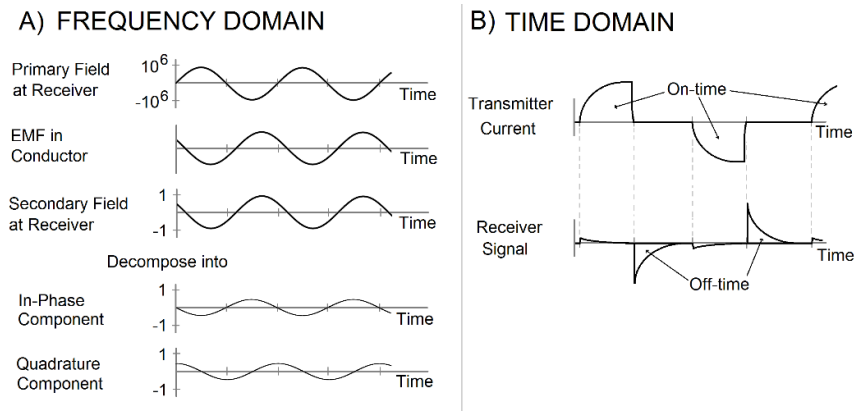

Figure 2 Schematic representation of FEM and TEM. A) shows a frequency domain system's primary and secondary fields at the receiver. B) shows the transmitter current for a time domain system with square waveform, and the resulting receiver signal.

The last major historical categorization of AEM systems is whether the system is attached to an airplane, called a fixed-wing system, or whether it is attached underneath a helicopter. Fixed-wing systems need to fly fast in order to remain in the air, which can be both a blessing and a curse. High operational speeds are beneficial when the goal is to cover large areas fast and cheaply. Lower operational speeds are beneficial when high precision measurements are desired. Furthermore, fixed-wing systems generally fly at higher altitudes than helicopter systems due to their limited maneuverability.

In the mid 00's ATEM systems were the up-and-coming systems, which showed promising characteristics compared to well-established AFEM systems. However, which system would ultimately prove the de-facto standard EM exploration system was yet to be determined. Today, ATEM systems are well-established, and most often the method of choice, with powerful system characteristics concerning: depth of investigation, shallow surface resolution, operational speed, and data accuracy.

The ideal AEM system for a given problem depends on the purpose of the survey. Broadly speaking, survey goals can be either detection or mapping. This results in two different types of AEM systems, one system type that focuses on strength/speed and probes the earth as deep/fast as possible, and another system type that focuses on finesse and probes as accurately as possible. However, recent advancements have brought these two separate system types closer together, to the point where there now exist sophisticated systems capable of both deep/fast detection, as well as accurate mapping.

Detection surveys are most commonly used in mineral prospecting. Here AEM has primarily been used as an effective first approach tool for covering large areas. Traditionally this has been accomplished by using deep probing fixed wing systems, with the receiver towed behind the aircraft (Smith 2014). However, since around 2000 the helicopter systems have moved into this area with similar or greater probing capabilities.

Mapping surveys generally require the capability to measure small resistivity contrasts, and hence the focus is less on probing deeply, and more on controlling the system transfer function and the sensor itself. Thus, mapping surveys generally use more sophisticated, but less powerful hardware, which has been employed mostly from helicopter platforms. Typical targets in mapping surveys are low contrast groundwater

mapping and geotechnical applications. The helicopter systems for these applications started to appear in the mid 00's.

The most important factors controlling the shallow resolution of an ATEM system are:

- A rigid or well-determined system, with sufficient magnetic moment to probe to the depth of interest.
- A high bandwidth of the system. The bandwidth is set by both the receiver coil and the receiver instrumentation and should be well above 300 kHz.
- The shape of the transmitter waveform, which needs to have a fast turn-off in order to energize the earth with high frequency energy.
- Unbiased and uncontaminated early- and late-time gates for a good resolution of the shallow geological layers.

Advancements in the last decade

Within the last decade, no AEM system type has seen as much advancement as the helicopter-TEM systems (Legault 2015), and with these developments the focus has broadened. Systems used to be specialized for a particular field, but today, primarily due to multi-moment or multi-pulse technologies, general systems designed to service as many markets as possible are seen.

Depth of investigation

Depth of investigation (DOI) is often the main focus in mineral exploration, where the philosophy is generally that deeper is better. In groundwater and geotechnical explorations, a large DOI is less important, as long as the signal is strong enough to provide sufficient information at the depth of interest.
DOI depends on many parameters. The most important ones, which can be influenced, are the magnetic moment, the noise level of the receiver system, and the flight altitude.

The magnetic moment is the strength of the signal emitted from the system, and thus in order to achieve deeper DOIs, there has been focus on increasing the moment. Allard (2007) showed how the moment of AEM systems steadily grew from less than 100,000 Am^2 to an excess of 500,000 Am^2, in the period 2000-2007. Within the last decade the moment has continued to grow, and today the major companies now all present at least one system with a dipole moment in excess of 1,000,000 Am^2, and in the case of HELIGEOTEM and MEGATEM the dipole moment has been pushed in excess of 2,000,000 Am^2 (though both those systems are designed for mineral exploration).

In order to achieve a large DOI, the noise level of the receiver system is also important, even though very little has been published about it. Receiver noise originates from the electronics of the receiver system and from the motion of the receiver coil in the earth's magnetic field. Assuming the electronic noise is at a fixed level, the only way to lift the signal above this noise is by increasing the area of the receiver loop, either by making the area of the loop large, or by adding more turns to the loop. However, the area of the receiver loop usually has to remain rigid and hence small in order to avoid primary field contamination, thus the choice is often to increase the number of turns in the loop. The drawback of this is that increasing the number of turns in the receiver loop decreases the bandwidth of the coil, which results in a worse shallow layer resolution (Effersø et al, 1999). Alternatively, sophisticated coil suspension systems can be employed in order to reduce the electronic noise (Nyboe and Sørensen 2012).

Surface resolution

Achieving a good subsurface resolution is a product of many different components and parameters, which must all be precisely balanced.

Instabilities and uncertainties can lead to smeared or unreliable data. A common way to counteract this is through deconvolution techniques to obtain early time measurements (Legault et al. 2012, Sattel and Battig 2016). Though deconvolution is commonly used to increase the apparent bandwidth of a system and push the early-gate information, Rasmussen et al. (2017) demonstrate how deconvolution is not always the best approach for handling the waveform.

Christiansen et al. (2011) show the resulting modelling errors, which would result from various inaccurate system descriptions. The paper highlights the importance of: using low-pass filters, accurately modelling the system geometry, and to include altitude as an inversion parameter. Similar work was performed on frequency domain systems in Minsley et al. (2014) using Monte Carlo methods.

Early-time gates provide the clearest information about the upper layers of the earth. Because of this, being able to measure as close to the ramp-off as possible is important for groundwater and geotechnical AEM systems.

ATEM receivers are generally not able to measure the earth response before the primary field is completely shut off, since the primary field is many orders of magnitudes larger than the secondary earth response. However, the primary signal takes longer to turn off for large currents, as shown in Figure 3. Thus, a system can either run with a low current and get a low DOI and early-time gate information, or run with a large current, but then loose the early-time information. This changed when SkyTEM introduced a dual-moment system, which allowed both a high DOI, from a high-moment transmitter pulse, as well as good shallow surface resolution, from a low-moment, fast-turn-off transmitter pulse (Sørensen and Auken 2004). Since then other approaches to achieving similar results have been developed. Prikhodko et al. (2013) use a full waveform approach in order to retain the high frequency component of the signal, and Chen et al. (2014) employ a multi-pulse approach.

In order to get as early gate information as possible, the receiver is usually placed in a zero-field position, such that the remnant of the primary field has the least influence on the receiver. Broadly speaking, there are three transmitter/receiver configurations employed in HTEM. The first one is to have the receiver placed in the center of the transmitter coil, shielded by a bucking coil. Conceptually, this method provides a desirable symmetry to the system, but in practice this method has some problems since the receiver is placed where the primary field is strongest – neglecting the bucking coil. Due to small movements of the systems as well as geometric inaccuracies, the shielding from the bucking coil is hard to get perfect. This can lead to primary field contamination. The second approach is to place the receiver in a natural off-center zero-position. The benefit of this approach is that even if the receiver moves slightly or is placed slightly off the zero-position, the field is naturally zero in this position (Auken et al. 2015), and hence small perturbations will give significantly less primary field contamination than in a center loop configuration. The third approach is to place the receiver far offset from the transmitter (Hunkeler et al. 2015). However, this approach makes accurate system geometry modelling particularly troublesome, since transmitter and receiver are no longer rigidly fixed. The TEMPEST survey system is one system that uses this method (Lane et al. 2000).

Around 2007, the earliest time gates ATEM systems could measure were $\sim 20\ \mu s$ after beginning of turn-off, which roughly corresponded to the turn-off time of the primary signal. Since then significant improvements have happened to measure earlier times.

As an example of the developments, early SkyTEM systems removed the early time gates. Instead, in order to push towards earlier times, SkyTEM Surveys developed field compensation schemes. These were built around coil response compensation, where the primary field was measured at a high altitude in order to get free-space primary field response and compensate for that by entering it as a factor in the inversion (Schamper et al. 2014). The second iteration, dubbed primary field compensation (PFC), employs the same high altitude measurement method, but in conjunction with a measurement of the coupling between the transmitter and receiver. The latest iteration of this measures the full impulse response of the system, and employs this directly on the hardware side. This allows data to be measured during the turnoff, hence gates can start measuring from 0 µs (Andersen et al. 2015).

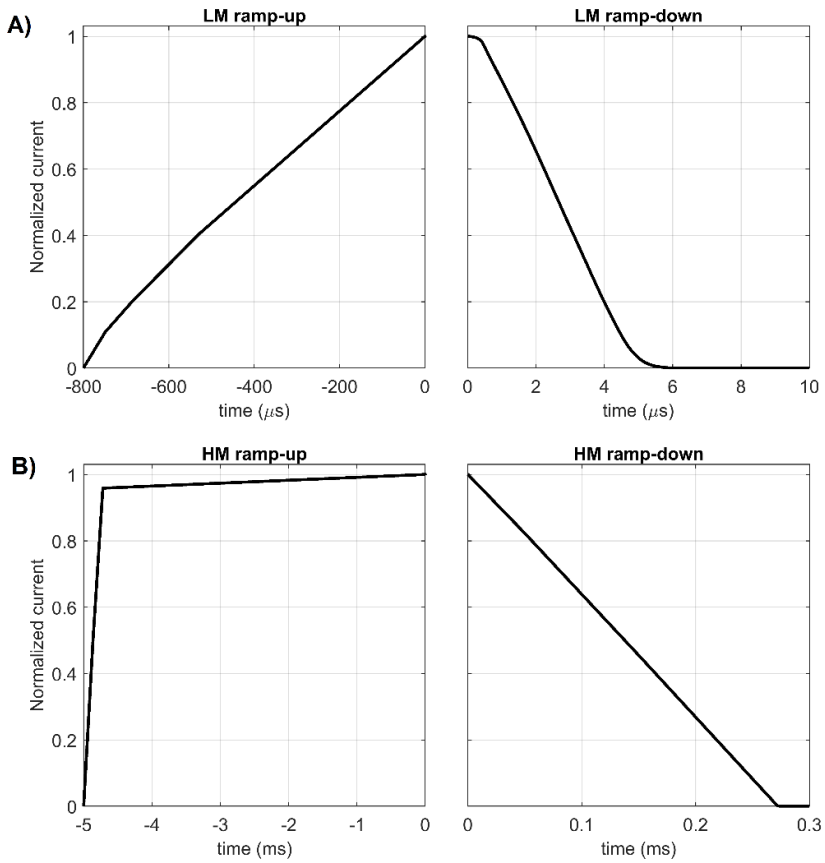

Figure 3 Turn-on and Turn-off ramps for the new SkyTEM306HP system, presented in Gisselø and Nyboe (2017). A) shows the low moment ramps. B) shows the high moment ramps. Note the difference in timescale between high moment and low moment. (courtesy of SkyTEM Surveys).

Current state of AEM systems

Frequency domain systems

Development of airborne frequency domain EM (AFEM) systems have been limited within the last 10 years. This is reflected in several ways:

- Legault (2015) reports that of the 70 papers presented at the South African AEM conference in 2013, only two of these papers dealt with frequency domain systems. A similar count of the 2017

EAGE Near Surface AEM conference revealed 21 abstracts concerning time domain, and 6 concerning frequency domain.

- The only notable development that has been made in AFEM systems within the last decade was made by Smiarowski and Macnae (2013), but despite successfully making a new AFEM design, which promised deeper DOI, the system never made it past prototype.

Today, the following general purpose AFEM systems are in operation: RESOLVE, DIGHEM, IMPULSE, and GEM-2A, are all HTEM systems, while Sander and GeoTechnologies operate a fixed wing FEM system, and GeoTechnologies operates the EM-4H system, which can be flown by both helicopter and plane. In addition, the Norwegian Geotechnical Institute (NGI) has developed a HFEM system specially designed for mapping of sea ice, called MAiSIE. A comparison of all these systems can be found in Table 1.

Frequency domain systems							
System name	IMPULSE	DIGHEMV	RESOLVE	GEM-2A	SGFEM	EM-4H	MAiSIE
Company	Geotech	CGG	CGG	Geophex	Sander & Geotechnologies	Geo Technologies	NGI
Method	HEM	HEM	HEM	HEM	Fixed-wing	Both	HEM
Frequencies (#)	6	5	6	3	4	4	broadband
Frequency range (kHz)	0.87-23.0	0.9-56.0	0.4-127.0	0.3-10	0.9-24.5	0.13-8.3	0.5-8
Configuration (Hor/Ver)	3H/3V	3H/2V	1H-5V	3H	4V	4V	H
Coil spacing (m)	6,5	6.3-7.9	7.9-9.0	5.1	21,3	6,5	2.7

Table 1 A comparison of the frequency domain systems currently commercially employed. Data are extracted from Kirsch et al. (2009), (Pfaffhuber et al. 2012), and company websites.

Time domain systems

There is a vast number of companies maintaining and developing airborne systems, but the three most significant players in the field at the moment are: Geotech, CGG, and SkyTEM Surveys. Geotech's and CGG's initial focus was mineral exploration systems, while SkyTEM's initial focus was groundwater exploration. All the systems have come a long way since then, and all three now have systems capable of both mapping and deep detection, but their initial focus is still apparent in their modern systems. A comparison of their current mapping systems can be seen in Table 2.

Time Domain systems, with accurate mapping capabilities from the 3 major companies									
Name	TEMPEST	AeroTEM	VTEM	VTEM+	$VTEM^{MAX}$	SkyTEM301	SkyTEM304	SkyTEM312Fast	SkyTEM516
Company	CGG	Geotech	Geotech	Geotech	Geotech	SkyTEM	SkyTEM	SkyTEM	SkyTEM
Method	Fixed-wing	HEM	HEM	HEM	HEM	HEM	HEM	HEM	HEM
Base freq (Hz)	25	90	30	30	30	325/75	270/22.5	270/30	275/25
Tx area pr turn (m^2)	244	110	240	540	960	341	341	341	536
Tx turns (#)	1	5	4	4	4	1	1/4	2/12	2/16
Waveform	Square	Triangular	Polygonal	Polygonal	Polygonal	Square	Square	Square	Square
Peak current (A)	300	410	250	310	335	6/95	9/110	5/120	3.5/120
Peak moment ($k\mathrm{Am}^2$)	73,2	220	240	625	1300	2/320	2.7/150	3/490	4/1000
Transmitter altitude (m)	120	30	30	30	30	30	30	35	30
Speed (m/s)	65	21	25	25	25	33	33	42	33

Off-time channels (#)	15	17	32	32	32	19/20	22/23	18/20	15/19
Earliest channel (µs)	13	87	21	21	21	4.2	5	9.2	10.2
Receiver component	XYZ	XZ	Z	XYZ	XYZ	XYZ	XYZ	XYZ	XYZ

Table 2 A comparison of Geotech's, CGG's and SkyTEM's ATEM systems. Information for the TEMPEST system is from Mulè et al. (2012), while information on VTEM and SkyTEM systems are from their respective webpages. SkyTEM's dual moment systems, are presented as the values for the low moment-/high moment-system.

According to their webpage, Geotech currently offers 3 different version of the VTEM system: VTEM, VTEM+, and VTEM^{MAX}. All the systems have an operational speed of 90 km/h, and have the receiver in the center of the transmitter loop. Their smallest system (VTEM) only has a vertical receiver, while the others offer horizontal configurations as well. Traditionally the VTEM systems have been designed with focus on high moment and late time-gate quality for deep mineral exploration. Their VTEM^{MAX} was the first AEM system to detect the Caber North deposit, which is a well-known and notoriously difficult site to detect, since it is buried at a depth of more than 300m and below a conductive overburden (Killeen 2013). The VTEM systems are single moment systems, which gives them limited resolution in the upper layers, though the resolution has been significantly improved by including more early-time information (Prikhodko et al. 2013). While the AeroTEM system (Balch et al. 2003) is not listed on Geotech's website, many surveys have been flown using the system in the last decade. The latest development from Geotech was presented at EAGE 2017, where Eadie et al. (2017) presented the VTEM Early Time (ET); which focuses on further improving VTEMs early time capabilities. VTEM ET enables 500 μs ramp-off times, which is roughly three times faster than traditional VTEM systems. Furthermore, the new design increases the receiver bandwidth to allow more early time information.

Historically, CGG has offered a variety of fixed wing and helicopter ATEM systems with a focus on mineral exploration, such as their well-known MEGATEM II, and HELITEM systems. In order to map the shallow near-surface they use a multipulse approach (Chen et al. 2014). CGG also operates the TEMPEST fixed-wing system, which carries a towed receiver bird. The system is described in great detail in Lane et al. (2000). Christiansen et al. (2016b) show that it is possible to get accurate modelling with the TEMPEST system. Their new GRYPHON system combines TDEM, magnetics, gravity-gradiometry, laser-scanning, and radiometrics into one system (Killeen 2014).

SkyTEM's original system was designed for groundwater mapping, but has since been upgraded in several ways and is now used in a wide variety of geophysical cases. SkyTEM systems place their receiver in a zero position slightly above and behind the transmitter. Furthermore, SkyTEM introduced the multi-moment feature. This allows systems to have both a large DOI and shallow surface resolution. According to SkyTEM's webpage they currently offer services with five different system types: SkyTEM301, SkyTEM304, SkyTEM312, SkyTEM312Fast, and SkyTEM516. The first four systems use the same size frame, while the latter, SkyTEM516, uses a significantly larger frame, which allows it to reach a dipole moment in excess of 1M NIA. This gives them a DOI deep enough to detect and resolve the Caber north deposit. The SkyTEM301, SkyTEM304, and SkyTEM312, are modified versions of essentially the same system, with a slightly different DOI and resolution. SkyTEM312Fast is operated at up to 150 km/h, but is otherwise similar to SkyTEM312. The latest development from SkyTEM was presented at EAGE 2017, where Nyboe and Mai (2017) showed how the receiver bandwidth was considerably increased, and Gisselø and Nyboe (2017) presented the new SkyTEM-high-power variants, which are similar to the traditional systems, but have an increased dipole moment, lower weight, and faster ramp-off times.

While these are the leading companies in the field, there exists a variety of other companies with ATEM systems, though the vast majority are focused on mineral exploration. In our opinion the only other system designed for geotechnical and groundwater exploration surveys is the Xcite system, by New Resolution Geophysics of Cape Town, South Africa. This is a rigid inflatable HTEM system (Combrinck and Wright 2016).

System comparison studies

Over the years there have been a number of tests and comparisons of different AEM systems.

Steuer et al. (2009) compares a SkyTEM system with a German frequency domain system (based on the RESOLVE system) on a survey in Germany, where the geology targets are buried valleys. They conclude that the two systems provide comparable results, though the SkyTEM system of that time is not able to resolve the shallow area, but does provide a deeper DOI.

Abraham et al. (2012) tested the AFEM system RESOLVE, and concluded that the system showed excellent stability, and great agreement with ground truth. They furthermore concluded that their confidence in HEM systems greatly improved during the course of their study.

A more recent comparison was carried out by Bedrosian et al. (2016), which compares three different AEM systems over two different test areas in Nebraska, USA. The three systems are SkyTEM304, RESOLVE, and AeroTEM IV. The two test sites are characterized by shallow and deep alluvial aquifer systems. In the comparison they note that the RESOLVE and AeroTEM systems both display some level of coupling bias in the data near power lines, despite processing attempts to remove it, they conclude that the bias is apparent because data stacking is done before processing removes the coupled data. Despite this, they conclude that all three systems are capable of detecting and discriminating the large scale aquifer base, though the RESOLVE system is unable to constrain the base of the aquifer below a depth of 60 m, due to its shallow DOI. Furthermore they conclude that AeroTEM IV results show discrepancies at the shallow surface, due to their lack of early time gates. They finally estimate that this is also the reason why the AeroTEM IV system is overestimating the thickness of aquifer. Overall, the SkyTEM304 system corresponds well with the ground truth, but has trouble resolving the top 10 m of the subsurface.

5. Software

EM modelling is done in a variety of ways, but most approaches fall within one of four different categories: integral equation or differential equation, in either time domain or frequency domain. Generally, each of the different approaches has strengths and weaknesses.

Modelling

The following provides an overview of various significant advancements within AEM modelling within the last decade. For additional information on recent advancements in AEM modelling, the reader is referred to the reviews by Börner (2010) and Everett (2012).

1D Modelling

The governing equations resulting from the 1D approximation were developed in the 1980's, and are built on the integral formulation of Maxwell's equations (Ward and Hohmann 1988). 1D modelling is the de facto workhorse when it comes to AEM, and will remain so for a while. The reason for this is that 1D modelling is several orders of magnitude faster than either 2D or 3D modelling, and thus making it an invaluable first approach tool. Advancements made to 1D AEM modelling today are mostly about increasing the computational speed, and system modelling. Kirkegaard et al. (2015b) explain how 1D

calculations can be vectorized and parallelized. By deviating from the intuitive recursive way of calculating the 1D kernel, it is possible to make an algorithm that is both parallelizable and vectorizable.

Christensen et al. (2009) developed a fast 1D approximate method, which uses an iterative process to calculate an apparent earth conductivity. Christensen (2016a) refines this method by choosing an optimal starting guess for the apparent conductivity, which significantly speeds up the approximation as well as making it more accurate. The refined method claims an impressive speed-up of 50 times compared to the normal 1D approximation, while keeping the additional modelling error below 1 %.

2D Modeling

The 2D approximation used in AEM, assumes a 2D earth and a 3D source, and is commonly referred to as the 2.5D formulation (Stoyer and Greenfield 1976). The 2.5D approximation resembles situations encountered in AEM, but is less commonly used because of its considerable computational burden, due to the expensive inverse Fourier transformation.

The most common method is to split the total field into a primary and secondary field. The reason for doing this is that the discretization will inevitably introduce a small error, so rather than introducing this error on the total field, which is several orders of magnitude larger than the secondary field of interest, the primary field is calculated analytically, and the error is only introduced on the secondary field. Li et al. (2016) use this approach in conjunction with a finite element mesh and operate in the frequency domain. Their code uses a damped least square inversion algorithm based on the single value decomposition principle. Yu and Haber (2012) use a finite volume approach in frequency domain, with a limited-BFGS inversion algorithm. Vöge et al. (2015) use 2D modelling to model sea-ice thickness with a finite element code operating in frequency domain. Their code was extended in Boesen et al. (2017) to include local meshing, and optimized in several ways, to enable accurate modelling of much larger surveys.

3D Modelling

With the increase in computer power, 3D modelling and inversion have become feasible, and several research groups are now actively developing various kinds of 3D codes. The group at University of British Columbia have two separate code repositories, capable of doing full 3D modelling and inversion. Their newest code is built in the new high-performance scientific programming language Julia (Bezanson et al. 2012). The code is open-source, and is built on a general partial differential equation solving framework called jInv (Ruthotto et al. 2016). jInv currently supports both finite difference and finite volume meshing, as well as adaptive octree meshing. The 3D EM modules built upon this framework, can handle 3D simulations using both the frequency- and time-domain approach and is described in Haber and Schwarzbach (2014). The other 3D open-source code, is built in python and is called SimPEG (Cockett et al. 2015). SimPEG is a general purpose inversion framework, capable, among other things, of doing 3D EM simulations, as demonstrated in Heagy et al. (2016). SimPEG is not designed for large surveys, but rather for academic studies as well as educational purposes.

Börner et al. (2008) have built a 3D forward modelling code with a finite element mesh. The code operates in the frequency domain, by projecting the Helmholtz equation onto a Krylov subspace using the Arnoldi process. The transformation back to time domain is handled through a Hankel transform. The code was later expanded to include time domain propagation as detailed in Börner et al. (2015), which they argue is generally computationally superior.

Mulder (2008) has built a 3D frequency domain forward modelling code using the multigrid method with a generalized finite volume mesh. He concludes that multigrid methods perform excellently when used with a constant grid spacing, but have a less than satisfactory performance when used on stretched cells.

Cox et al. (2010) introduced the moving footprint approach, which allowed them to handle much larger surveys than would otherwise be possible. They used it in conjunction with a 3D integral equation scheme, which allowed them to present a full 3D modelling and inversion code, capable of handling large surveys. The code was originally only able to handle frequency domain systems, but was later upgraded to also handle time domain, as detailed in Cox et al. (2012). While integral equation approaches generally have trouble with large conductivity contrasts, their code showed some promising results on field data as seen in Wilson et al. (2012), though data misfits were not shown.

Yin et al. (2016) have created a 3D code that uses the finite element approach and allows electrical anisotropy to be included in their modelling. This opens the possibility for more accurate modelling of distinct dipping stratifications, which are commonly found in mineral explorations or faults. They model their system in the time domain.

Ansari et al. (2017) demonstrate a 3D modelling code, using a gauged finite element potential. The code simulates both the inductive and galvanic part of the EM field using edge-based finite elements. Because of the edge-based finite elements, the code is subject to numerical leakage, which does contaminate the models. Despite this, they showed that the code is capable of modelling the Ovoid ore deposit at Voisey's Bay, Canada.

Cai et al. (2017) demonstrate a 3D modelling code, using edge-based finite elements, and a hybrid boundary condition. Their approach uses implicit time propagation and is demonstrated on synthetic data.

Induced polarization and superparamagnetic effects

Converting resistivity to geology can be tricky, since it is well-known that different materials can exhibit similar resistivities. Induced polarization (IP) can help alleviate this problem by introducing more parameters to distinguish subsurface materials. Not only can IP modelling help distinguish subsurface materials, but IP-effects can also be a major issue if not included in areas with strong IP effects, since these can disturb the other modelling parameters. IP occurs when a material is capable of retaining a charge for a significant amount of time after being subjected to an electromagnetic field. The two main mechanisms that cause IP effects are membrane- and electrode-polarization (Kratzer 2013). IP has been studied for decades, using grounded electrodes, despite these having been observed frequently in airborne surveys (Weidelt 1982, Smith and Klein 1996, Kang and Oldenburg 2015).

Superparamagnetic effects are similar to those of IP in many ways. They are both late time effects that significantly disturb the data and the resulting model if not properly accounted for, but the driving mechanism for superparamagnetic effects is completely different from that of IP. Superparamagnetic effects are caused by small para- or ferromagnetic particles, which because of their small size have the freedom to flip their magnetic field randomly. Given enough superparamagnetic material, this flipping gives rise to a significant magnetic signal which appears similar to the discharge of a large buried conductor (Kratzer 2013).

Several cases of superparamagnetic effects have been studied recently. Kratzer et al. (2013) studied the effect of SPM, and conclude that by using a uniform SPM time constant distribution of t^{-1}, they are able to model the SPM effects in the field examples shown. Sattel and Mutton (2014) modelled SPM effects using a Chikazumi susceptibility model (Chikazumi and Graham 2009), and they furthermore suggest several ways

to reduce SPM effects. Macnae (2016b) develops a model for fitting both IP and SPM effects simultaneously, using a Cole-Cole model for the IP effect. Note that the IP and SPM effect produce similar signals, but with opposite signs, and can thus be distinguished. The effectiveness of this method is demonstrated in both Macnae (2016a) and Hine and Macnae (2016).

The latest significant development on SPM is from Bournas et al. (2017), where an innovative dual receiver EM system is used for attenuating SPM effects, see Figure 4. Furthermore SPM effects are predicted using a pattern recognition effect, based on supervised classification.

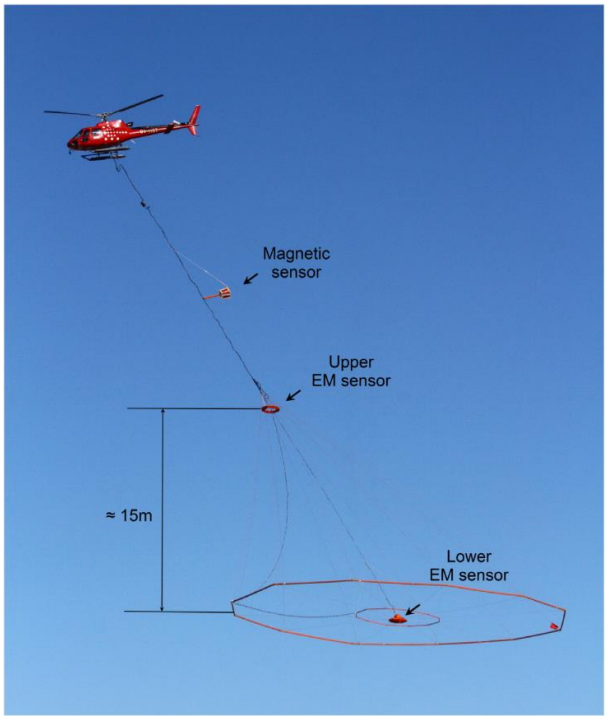

Figure 4 A dual receiver EM system, with a lower and upper EM receiver. From Bournas et al. (2017), (courtesy of Elsevier).

Marchant et al. (2012) use a 3D method, with an approximate IP-current, and showed that it was possible to measure pure IP signals in airborne systems by combining data collected at two frequencies. Furthermore it was shown that the IP signal could be inverted, and the 3D subsurface chargeability recovered. Marchant et al. (2014) extended the method into time domain. In Marchant (2015) the work is finalized, and it is concluded, that while it is possible to do inductive-source IP, there is still significant work left before this approach can be used in practice. Following this, Kang and Oldenburg (2016), built on the experiences gathered in Marchant (2015), and made a new three step method for approximating the IP effect.

The latest development in airborne IP comes with the two papers by Viezzoli et al. (2017) and Kaminski and Viezzoli (2017), in which airborne IP effects are included in 1D modelling. This method, unlike the previous one, does not try to decouple the IP signal from the EM signal, but rather treats everything together. While it is theoretically possible to extend their method to the full 3D modelling case, it is not a trivial extension. The method is successfully tested on field data with convincing results.

Inversion

In the following section, the various inversion techniques commonly used today will be presented. We have tried to summarize and modularize what is needed, in order to do an inversion, as well as provide the latest advancements within each area. For additional information about recent development in inversion, Chang-Chun et al. (2015) have written a review of airborne inversion.

Apart from imaging techniques, which strictly speaking do not perform an inversion, most other inversion techniques are done by defining an objective function, and thus turning the inversion problem into a minimization problem. In general a minimization needs: an objective function to minimize, a minimization scheme, and a forward modelling method.

Objective functions

Objective functions quantify the goal of an inversion. In the literature, people use various objective functions, but most of the objective functions can be written in the following general form:

$$q = q_{obs} + q_r, \tag{1}$$

where q_{obs} gives the misfit between model data and observed data, and q_r gives the regularization misfit, which contains any prior information, as well as roughness constraints. In matrix form the misfits can generally be written as:

$$q_{obs} = N_d^{-1} \delta \boldsymbol{d}^T \boldsymbol{W}_{obs}^T \boldsymbol{C}_{obs}^{-1} \boldsymbol{W}_{obs} \delta \boldsymbol{d}\,, \tag{2}$$

$$q_r = N_r^{-1} \delta \boldsymbol{m}^T \boldsymbol{R}^T \boldsymbol{W}_r^T \boldsymbol{C}_r^{-1} \boldsymbol{W}_r \boldsymbol{R} \delta \boldsymbol{m}, \tag{3}$$

where N_d, is a normalization to the number of data points, while N_r is a normalization to the number of regularizations used, $\delta \boldsymbol{d}$ is the misfit of the forward response, $\delta \boldsymbol{m}$ is the variation in the model vector, $\boldsymbol{W}_i$ is a weight matrix, $\boldsymbol{C}_i$ is a covariance matrix, and $\boldsymbol{R}_i$ is a roughness matrix, detailing which model parameters are bound together. The weight matrix determines the normalization scheme, and is commonly chosen as: a minimization of the squared differences between observed and forward data, L_2, (Constable et al. 1987), absolute differences, L_1, (Farquharson and Oldenburg 1998), or schemes favoring more blocky models like sharp SCI (Vignoli et al. 2015).

While most objective functions can be described using equation 1-3, there are exceptions. Abubakar et al. (2008) use a multiplicative objective function, with L_2-norm. One advantage of using a multiplicative objective function, is that they avoid the ad-hoc specification of balance between the different misfit terms. Their regularization term can be chosen to either favor smooth or blocky conductivity models.

Minimization schemes

In the following we go through different minimization schemes. The most common one for 1D modelling, are quasi-Gauss-Newton schemes, while for 2D/3D modelling the most common are BFGS schemes. For the sake of brevity, the schemes are presented without regularization constraints.

Gradient descent

The simplest scheme is the gradient descent scheme, where the model update, $\boldsymbol{m}_{n+1}$, is given as (Saad 2003):

$$\mathbf{m}_{n+1} = \mathbf{m}_n + \gamma_n \nabla(\delta \boldsymbol{d}_n), \tag{4}$$

with γ being a line search length.

Conceptually, the method follows the gradient towards a local minima. While convergence to a local minima is assured, the convergence rate is usually low near the local minima, and as such other methods are generally considered superior (Press et al. 1992).

Quasi-Gauss-Newton

Tikhonov regularization methods are the most commonly used in geophysical EM, and are often combined with a Gauss-Newton minimization:

$$\mathbf{m}_{n+1} = \mathbf{m}_n + \left(\boldsymbol{G}_n^T \boldsymbol{C}_n \boldsymbol{G}_n + \boldsymbol{\Gamma}^T \boldsymbol{\Gamma}\right)^{-1} \boldsymbol{G}_n^T \boldsymbol{C}_n^{-1} \delta \boldsymbol{d}_n, \tag{5}$$

where $\boldsymbol{G}$ is the Jacobian, and $\boldsymbol{\Gamma}$ is known as the Tikhonov matrix.

A particular interesting special case, comes from setting the Tikhonov matrix to a scaled identity matrix. In that case the Levenberg-Marquardt method arises, which combines gradient descent with the Gauss-Newton method, in an effort to get the best convergence rate from both methods. The Levenberg-Marquardt model update is given as:

$$\mathbf{m}_{n+1} = \mathbf{m}_n + \left(\boldsymbol{G}_n^T \boldsymbol{C}_n \boldsymbol{G}_n + \lambda_n \boldsymbol{I}\right)^{-1} \boldsymbol{G}_n^T \boldsymbol{C}_n^{-1} \delta \boldsymbol{d}_n, \tag{6}$$

where λ is a tuning parameter, which determines the amount of influence the gradient descent and the Gauss-Newton method have on the current step. Levenberg-Marquadt, or other similar methods, gives reasonable convergence and are often used, though the cost of computing the Jacobian can be very high and make other methods more attractive.

Nonlinear Conjugate gradient

The nonlinear conjugate gradient method (Hestenes and Stiefel 1952), or a nonlinear Bi-Conjugate gradient method for complex matrices (Van der Vorst 1992), are popular minimization methods, which perform a Gram-Smith-like orthonormalization search towards a local minima. Nonlinear conjugate gradient methods are typically combined with a preconditioner in order to speed up the process of convergence.

BFGS / Limited-BFGS

BFGS, and especially limited-BFGS methods are among the most successful, when it comes to quasi-Newton methods - that is, methods that use an approximation to compute either the Jacobian or the Hessian. Quasi-Newton methods are especially relevant for full 3D inversions, where calculating the Jacobian is often extremely expensive. The usability of the BFGS methods stands or falls with its convergence rate. Convergence rates of iterative methods appear to be highly problem dependent and difficult to pin down. Lewis and Overton (2013) offer a nice overview of the potential of BFGS methods and believe it should be possible to determine a class of problems for which the BFGS methods will have a good convergence rate, but so far no such classification has been successfully made. Nash and Nocedal (1991) give a convergence comparison between nonlinear conjugate gradient methods, Gauss-Newton methods, and BFGS methods. They conclude that the convergence rate of BFGS methods are comparable or slightly better than the others. On the other hand Haber (2004) reports unsatisfactory convergence rates using pure Limited-BFGS methods on EM-problems, and instead suggests using BFGS methods as a preconditioner for other inversion schemes as detailed in Haber et al. (2007).

Monte Carlo

Finally, there are various Monte Carlo (MC) methods, which rely on an element of randomness to perform an inversion. The strength of MC methods are that they enable the code to find the global minimum, whereas all the other methods only lead to a local minimum, and thus MC methods are less dependent on the starting model. Furthermore, MC methods provide full parameter estimation information, as exemplified in Figure 5. Finally, it is possible to create MC methods that do not require calculations of the

Jacobian or Hessian, though such methods are rarely favorable. The downside to all this is that MC based inversions typically require 1,000-1,000,000's of forward computations. Thus, the total cost of performing an MC inversion is inevitably high, and as such they are often only used as a benchmark tool. While many approaches to MC inversion exist, the dominating algorithm in AEM seems to be the Metropolis-Hasting Monte Carlo (MHMC) algorithm, which is a special case of Markov-chain Monte Carlo simulations.

Minsley (2011) presented a MHMC inversion method for airborne frequency domain data, which is used successfully to model permafrost thaw in Minsley et al. (2015).

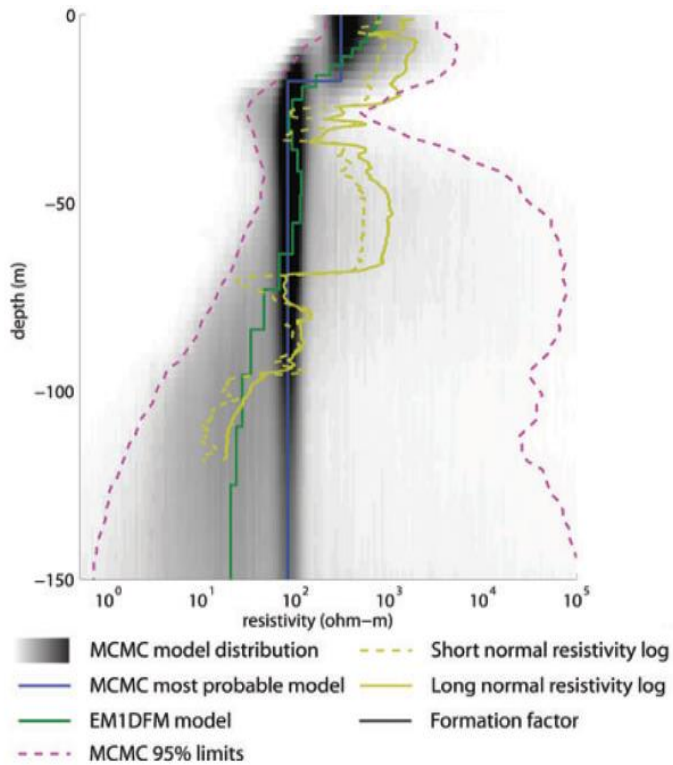

Figure 5 Distribution of MCMC models. Modified from Minsley (2011), (courtesy of Oxford University Press).

Brodie and Sambridge (2012) and Brodie and Richardson (2013) have also presented a MHMC inversion code, which was originally designed for seismic tomography, but has been redesigned for AEM use. They primarily use the code for testing parameter resolvability, but note that the method can be used to invert full flight lines at a reasonable cost.

Another MC approach is referred to as simulated annealing, which is an adaptation of the MHMC method, with roots in thermodynamic modelling, and based on the Boltzmann cooling principle. Yin and Hodges (2007) demonstrate the use of simulated annealing on synthetic data, see Figure 6, and with a field example. They use an objective function with no traditional regularization, and instead rely on the Boltzmann cooling to handle the regularization. Their approach is demonstrated successfully on inversions of 2 and 3 layer models.

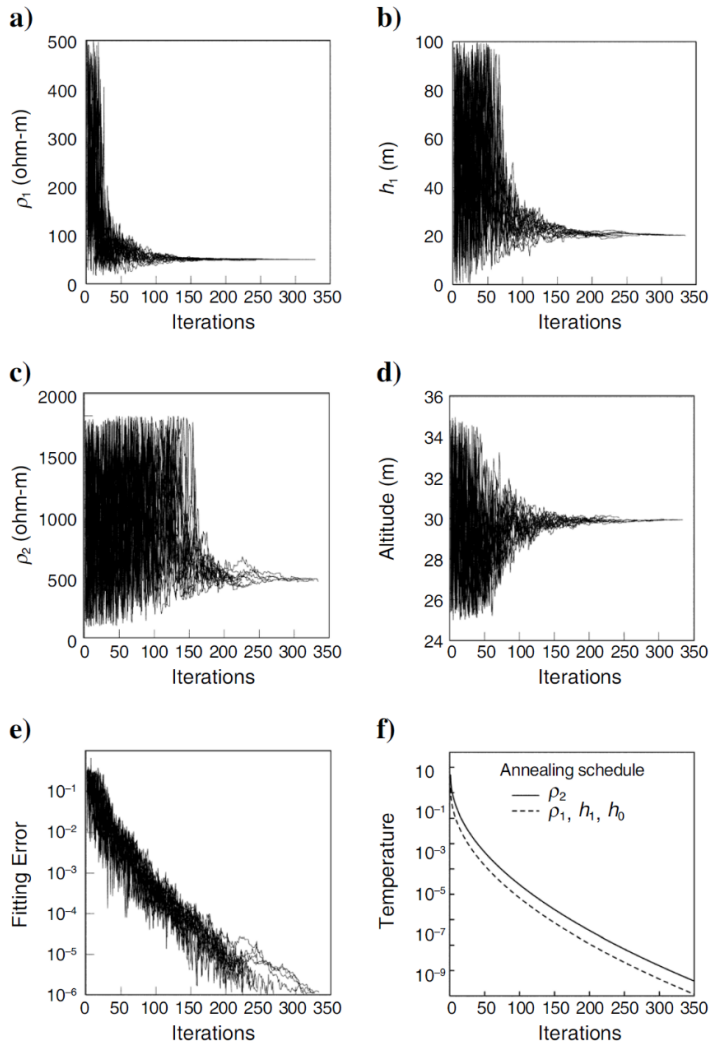

Figure 6 Simulated annealing for a 2 layer model. a-d) Show the resistivities, thickness, and altitude as a function of iterations. e) Shows the resulting data residual, while f) shows the exponential cooling scheme employed to slowly freeze the variables to a minima (h_0 is the altitude). From Yin and Hodges (2007).

Regularizations

In 1D inversions, regularizations are crucial, since they are the only thing connecting the various soundings internally and externally, and thus the only thing imposing any semblance of continuity into the inversion model. In higher dimensional modelling, regularizations are less critical since inversions generally contain inter-sounding information through the Jacobian. Even then, regularizations are generally used for all inversions, due to their stabilizing effect on what is otherwise an ill-conditioned problem, as clearly demonstrated by Ley-Cooper et al. (2014), in which the following inversion codes are compared on the same survey: EMFlow (Macnae et al. 1998), GA-LEI (Brodie 2012), AarhusInv (Auken et al. 2014), a 2D code from Guillemoteau et al. (2011), and Cox et al. (2010) 3D inversion code.

Auken and Christiansen (2004) introduced laterally-constrained inversion (LCI), which is used with 1D modelling codes, to create a quasi-2D inversion, by including lateral regularization. The usabilities and

limitations of this method were later examined using synthetic studies in Auken et al. (2008), and on field data in Ley-Cooper et al. (2010) and Siemon et al. (2009), and it was found that the LCI method introduced a significant advancement compared to single-site or stitched-together inversions on both field data and in synthetic studies. Another similar approach dubbed lateral parameter correlation (LPC) was developed by Christensen and Tølbøll (2009). In this approach the models are first inverted individually without any constraints. Next, a laterally smooth version of the models are found by solving a linear equation. Finally, a covariance analysis of the constrained and unconstrained model parameters is performed and is the basis for a third and final inversion. LPC had some initial trouble with topography, which introduced artifacts, however these artifacts are removed in the extension presented in Christensen (2016b).

Viezzoli et al. (2008) introduce spatially-constrained inversion (SCI), which extends the LCI regularization to a quasi-3D inversion, by finding the nearest neighbors - not just along flight lines, but also across. This is done by using a Delaunay triangulation on the soundings of the whole survey. In order to be able to handle large surveys, while preserving continuity, the SCI method initially required two inversions to be run. However, this was changed in Kirkegaard and Auken (2015), where various optimization techniques for the SCI methods are explained. After implementing the optimizations, they demonstrate that SCI inversion scales linearly, in both memory and time consumption with survey size.

While regularization schemes like LCI and SCI help bring a sense of continuity to an inversion, such a trait is not always desirable. In mineral deposits, for instance, the conductivity structure will often have sharp discontinuities. In order to correctly model such structures, Vignoli et al. (2015) introduce sharp inversions, which still retain the regularization, but have a max cost to conductivity contrasts, which means that small conductivity contrasts will still be constrained much like in the LCI and SCI case, while large conductivity contrasts will no longer incur a huge regularization cost. Thus continuity is still enforced for small conductivity contrasts, while at the same time enabling the freedom to have large conductivity contrasts.

The holistic approach is designed to wrap processing, and inversion, into one automatic process, and thus avoid multi-stage error propagation through the standard sequential processing approach. Brodie and Sambridge (2009b), which is an extension of the well-known holistic code presented in Brodie and Sambridge (2006), use an objective function similar to equation 1, with the regularization containing a channel bias roughness term, which is included in an attempt to shift some of the work normally done in processing, to inversion. The code operates in the frequency domain, and uses 1D forward responses. In Brodie and Sambridge (2009b) a large survey example, with ~ 8 million datapoints and a corresponding ~ 3.4 million model parameters, is successfully inverted. Brodie and Sambridge (2009a) extend the method to transient systems.

Christensen et al. (2017) presented a Voxel inversion, which decouples the inversion model parameters from the soundings. This enables multiple datasets to be combined in a true joint inversion with constraints. In their example, they combine a geophysical inversion of AEM data with a hydrological inversion of hydraulic conductivity fields, where the link between hydrological parameters and resistivity parameters are given through a spatially varying petro-physical relationship.

Finally, Lelièvre et al. (2009) should be mentioned, since they integrate geological and geophysical data through advanced constrained inversions. While we believe a more likely approach to combining geological and geophysical data is through machine learning after the inversion, this is certainly an interesting approach, which warrants further investigation.

Local mesh

In AEM, surveys commonly reach sizes too large for an all-at-once modelling and inversion (in 2D and 3D), as proposed in Haber et al. (2004). In order to counteract this, local meshing was created. Local meshing relies on the assumption that any sounding has a finite sensitivity range. Thus anything further away from the sounding than this range, can reasonably be assumed to negligible. For additional information on sensitivity functions, Christensen et al. (2017) have investigated sensitivity functions in both 1D, 2D, and 3D and show how they deviate from each other.

Cox et al. (2010) introduced the concept of moving footprints, which utilizes the finite sensitivity range of any EM system to significantly reduce the number of interactions that needs to be computed. This enabled them to perform 3D modelling and inversion of surveys larger than anything previously done, though the quality of their inversion results were disputed by Viezzoli et al. (2010).

Another local meshing approach is developed in Yang and Oldenburg (2012a), and Yang et al. (2014), and expanded to octree meshes in Haber and Schwarzbach (2014). Their implementation involves a global mesh, and a local mesh for each sounding, see Figure 7. While the forward problem is handled on the local meshes, the inversion is made by randomly subsampling the global mesh, this way they make the inversion more manageable, while remedying overfitting, which can often be a problem in inversions.

Boesen et al. (2017) introduced a local mesh for 2D modelling, which groups soundings in optimized bundles, where the size of a group depends on whether forward or derivative calculations are performed. Each group has an overlap with its neighboring group in order to preserve inline information.

Caudillo-Mata et al. (2016) have provided a general mathematical framework for upscaling, and while the primary ramifications of this work are related to multigrid methods, it is also significant for local meshing, since the method introduces an optimal framework for interpolation between the local- and global-meshes.

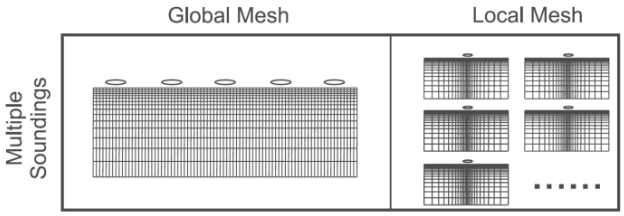

Figure 7 Local meshing, as implemented in Yang et al. (2014), (courtesy of Oxford University Press).

Hybrid schemes

Conceptually, a hybrid inversion is a multi-stage process, in which the early stages rely on some inexpensive approximate calculations, which are then, either gradually or abruptly, shifted towards more accurate and computationally expensive calculations at a later stage. By employing this method, less iterations of the more accurate and computationally expensive calculations are needed, at the cost of more iterations of lower accuracy calculations, with the overall effect of lowering the total computational time.

Yang and Oldenburg (2012b) presented a 3D multi-mesh approach, where they start off by using a coarse mesh, and as the inversion gets closer to convergence the mesh is refined to allow more accurate calculations.

Christiansen et al. (2016a) have presented a hybrid scheme, where an approximation is introduced in the early iterations during the calculations of the 1D derivatives. This makes the 1D derivatives less accurate; however as they note in the paper this has minimal effect on the actual inversion as long as the forward

modelling is done accurately. Nearing the end of the inversion, the code switches back to accurate derivatives in order to reach comparable levels of misfit as in the traditional approach. The result of this hybrid approach is a speed-up factor $\sim 3 - 7x$.

Boesen et al. (2017) have created a hybrid 1D/2D scheme with three stages. In the first stage, 1D forward and derivatives are employed. In the second stage, 2D forward and 1D derivatives are employed. In the third and final stage, 2D forward and derivative calculations are used. This approach gives models, which are comparable to a full 2D inversion, but computed ~2-6x faster.

Other advances

Automated processes

Geophysical EM methods are generally quite involved; meaning that once data have been recorded, it needs to be processed, a modelling and inversion scheme needs to be chosen, and finally the resulting model needs to be geologically interpreted. Each step requires time and introduces subjectivity into the data. In an ideal world all these choices and processes would be automated, thus saving time and removing subjectivity from the data analysis. This section looks at various advancements towards this goal.

The dual papers by Ullmann et al. (2016) and Scheunert et al. (2016), introduce the cut-&-paste approach. This seeks to automate the process of running 1D inversions on a large survey, and then if necessary selecting parts of this survey for more advanced 3D inversions. Their approach employs image processing algorithms to identify regions which need higher dimensional inversion. After the 3D inversions are performed the 3D models are recast and reintegrated into the 1D models. In the papers both a successful synthetic study and a field example are shown. Their current implementation works on frequency domain data.

Reninger et al. (2011) use singular value decomposition in order to perform a user-assisted de-noising of airborne TEM data and reduce processing time and subjectivity. Andersen et al. (2016) use a neural network to automate the processing task, and they conclude that while the method is able to reduce the processing time by more than 50 %, the neural network is locally dependent and thus needs to be trained on a subset of each individual survey before being useful. Friedel et al. (2016) use another machine learning technique called self-organizing map (SOM), which is an unsupervised machine learning technique. They use this method to automate the geological interpretation of inversion models in near real-time. To train their algorithm they use airborne frequency domain EM data, along with inverted resistivity profiles, geophysical borehole data, and hydrogeological data.

Optimizations

AEM surveys can reach huge sizes with millions of datasets and millions of model parameters, where modelling and inversion on such surveys can be a very computationally demanding task - even in 1D, but especially for 2D or 3D. As such, it is paramount that the codes used are as fast and efficient as possible. Towards this end there have been several significant advances in the last decade.

Parallelism

Since the advancement of computer clock frequency stalled with the introduction of the multi-core CPU in 2005, the theoretical performance of processors has continued to follow Moore's law, and increase with the same exponential rate as before, but in a fundamentally different way. Performance advancements in modern hardware no longer automatically translate into a performance increase for software. In order to utilize the increase in computational power within the last decade, software has to be specifically written to account for it. The modern scientist has to carefully design his code to not only make use of multiple cores,

but also to extract additional parallelism in the form of vectorization. Kirkegaard and Auken (2015) describes in great detail how they parallelized a 1D code, while Kirkegaard et al. (2015a) shows how vectorization and parallelization can be employed in 1D modelling to achieve a speedup of more than an order of magnitude using modern hardware. Another paper that goes into great details in designing EM codes optimized for parallelization is Haber and Schwarzbach (2014), where the focus is on cluster parallelization of the 3D EM problem.

Sparse linear solvers

Solving sparse linear systems efficiently is, for most modelling and inversion schemes, of vital importance. The linear systems in AEM can reach millions of equations and unknowns, which makes solving them efficiently a nontrivial issue. The methods for solving sparse linear systems are generally split in two categories: direct solvers and iterative solvers. While favor seems to have shifted towards direct solvers within the last decade, both methods have their strengths and weaknesses.

Direct solvers do a full factorization of the system matrix, which can take quite a while and use a lot of memory. However, once such a factorization is done, the system can efficiently be solved for any number of right-hand sides. For direct solvers a number of readymade libraries exist. This makes using direct solvers relatively straightforward. Amestoy et al. (2001) introduced the direct solver named MUMPS, which is fully parallelized using the MPI-interface, which makes it capable of operating in parallel on a cluster. Schenk et al. (2000) introduced the direct solver used in the Pardiso library, which is parallelized using the OpenMP interface, and thus making it capable of running in parallel on a single computer. MUMPS and Pardiso are currently the two state-of-the-art direct solvers, and which one you should employ depends on the level of parallelization you wish. A slightly outdated comparison of direct solvers can be found in Gould et al. (2007), while a more modern comparison can be found in Puzyrev et al. (2016). Their main conclusion is that the applicability and scalability of direct solvers have risen significantly and is nearing the theoretical limits. That being said, the biggest problem with direct solvers is still the fact that they are not efficient at handling very large linear systems. This is because even though the system matrix might be extremely sparse, there is no guarantee that the factorization matrix will remain sparse.

Iterative solvers on the other hand, use either no factorization, or at most a partial factorization, followed by multiple forward- and backward-substitutions, in order to iteratively find a solution to the linear system. Unlike direct solvers, there exists no efficient and ready to use library for iterative solvers. The main reason for this is probably the existence of many different algorithms, and which one is superior is heavily system dependent. Saad (2003) contains all the most common algorithms used for iteratively solving sparse linear systems. Oldenburg et al. (2012) compare the use of direct and iterative solvers for the case of 3D modelling and conclude that direct solvers are favorable for these kinds of problems. While this might indeed be the case, our personal experience with iterative solvers suggests that the computational times shown in Oldenburg et al. (2012) for iterative solvers can be improved significantly by applying more optimal preconditioners, and thus the question of which method is superior remains.

Kirkegaard and Auken (2015) describe the iterative linear solver they use for 1D problems in great detail. Their solver consists of applying the reverse Cuthill-Mckee reordering algorithm (Cuthill and McKee 1969), followed by a Bi-conjugate-gradient-stabilized algorithm, used in conjunction with an incomplete Cholesky factorization as preconditioner.

Multigrid methods

The idea behind multigrid methods stems from the fact that convergence on fine grids tends to stall after a few iterations. In fact, for many iterative methods, the number of iterations needed to reach convergence

is proportional to the number of nodes in a direction. A simple way of making sense of this is that during a convergence process, each iteration only allows information to travel from nodes to their neighbors. This, combined with the fact that reaching convergence generally requires information to be passed from one end of the grid to the other several times, explains the slow convergence. In an attempt to rectify this issue, multigrid methods use coarse meshes in conjunction with the normal mesh (see Figure 8). These coarse meshes allow information to be passed much further, and thus convergence can be reached much faster.

While multigrid methods have great potential for providing speedups, they also bring several issues that need to be addressed. First the non-trivial nullspace of the curl-curl operator needs to be dealt with in order for multigrid methods to be used in EM. Another issue is that multigrid methods are dauntingly difficult to implement and require interpolation schemes to downsample and upscale between the different meshes. Not only are such interpolations expensive, but until recently no optimal general mathematical framework for doing them existed. Caudillo-Mata et al. (2016) have provided a general mathematical framework for upscaling, which shows impressive improvements compared to traditional upscaling methods. Their approach recognizes the non-uniqueness of the upscaling problem, and rather than employing an analytical expression, they turn the problem into a parameter estimation problem, which can be solved using an optimization technique. This approach allows user-input and takes surrounding conductivities into consideration when making upscalings. In their paper the method is demonstrated on both 1D and 3D examples. In order to handle the nullspace, one of three different approaches is commonly employed. Haber and Heldmann (2007) use a Helmholtz decomposition of the discrete fields in order avoid the nullspace and stabilize the fields. The second approach explicitly compensates for it using a divergence correction (Hiptmair 1998). The third approach is to implicitly compensate for it by solving small local systems as done in Mulder (2008).

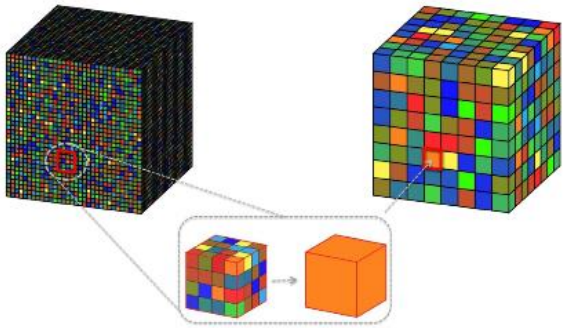

Figure 8 Upscaling process. Modified from Caudillo-Mata et al. (2016), (courtesy of Elsevier).

Depth of investigation

Depth of investigation (DOI) usually refers to the maximum depth at which data is sufficiently sensitive to the earth properties to affect the data above the noise level. Thus roughly speaking, DOI is an estimate for how deep a model can be trusted.

Several different approaches to estimating DOI exist. Early work on DOI estimation focused on a skin depth approach and effective model resistivities (Spies 1989). Another approach was suggested by Oldenburg and Li (1999), which involves starting two inversions from different halfspace resistivities. As noted in Christiansen and Auken (2012) both these approaches have limitations, which make them undesirable. Instead, they suggest a global 1D DOI, based on cumulative sensitivity from the Jacobian. This approach

gives a reasonable trade-off between accuracy and time consumption. Fiandaca et al. (2015) extend the global 1D DOI approach to multi-variate models, in which cross correlation between parameters is considered. This is particularly relevant for induced polarization or higher dimension modelling.

If Monte Carlo methods are employed, then parameter estimation as well as DOI information are usually inherently available, as seen in Figure 5.

Finally, a paper by Bin et al. (2014), presents an approach to DOI, which is based on following the position of the maximum electric field value, through a halfspace model. The DOI is then defined as the depth at which this maximum reaches the noise floor. In the paper, the method is not compared to any other DOI method, and the effectiveness of this approach seems questionable.

6. Case examples

We conclude this paper by showing a number of case studies exemplifying the wide area of applicability AEM methods have today.

Finding quick clay

In several parts of the world, quick clay is a serious geohazard. Quick clay is characterized by its very small remolded shear strength (Rankka et al. 2004). Due to this small shear strength, it is prone to cause retrogressive landslides, which have previously caused massive damage. Pfaffhuber et al. (2017b) showed how AEM can be used to delineate potential quick clay almost as well as ground based electrical resistivity tomography.

Delineating hazardous material

In Norway black shale cause a serious risk to human health, because of its geochemical composition, which includes significant amounts of sulphides and uranium. Furthermore, if exposed to air, the sulphides oxidize, which produce sulphoric acid that poses a hazard to both concrete and metal constructions as well as the environment. In Pfaffhuber et al. (2017a) AEM resistivity data is linked with geochemical compositions, allowing the black shale to be mapped using AEM.

Mapping the fresh-saltwater interface

In Holland saltwater intrusion into the coastal aquifers, which supply water to a large percentage of the population is a crucial issue. Pedersen et al. (2017) demonstrate how AEM mapping can provide unique insight into the water quality of the aquifers. During the survey they were able to distinguish the delicate balance between salt water and fresh water and track the salt-water intrusion several kilometers into the inland region, as seen in Figure 9.

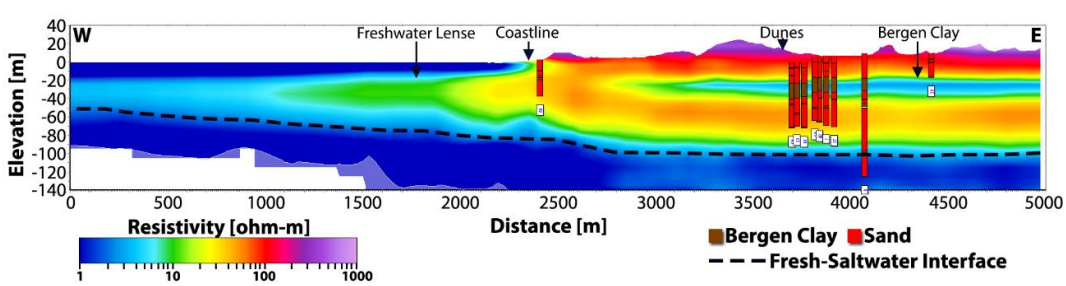

Figure 9 Salt water intrusion into the mainland, as well as the freshwater lens into the sea. The data shows excellent agreement with the drillings in the area. From Pedersen et al. (2017), (courtesy of First Break).

Deep groundwater mapping in Antarctica

One clear advantage of AEM methods over any alternative method is their ability operate in remote, uninhabitable areas. Mikucki et al. (2015) demonstrates how AEM methods have been used to map groundwater and tunnels beneath glaciers in Antarctica as seen in Figure 10. This mapping suggested a flow between Lake Hare and Lake Fryxell, lakes which were previously thought to be isolated. The ramifications of this are profound for the understanding of the geochemistry of the lakes. In a similar vein, there are several permafrost papers from Alaska (Minsley et al. 2012, Pastick et al. 2013, Minsley et al. 2015), which further demonstrate the robustness of the equipment and the applicability of AEM methods for cryospheric mapping.

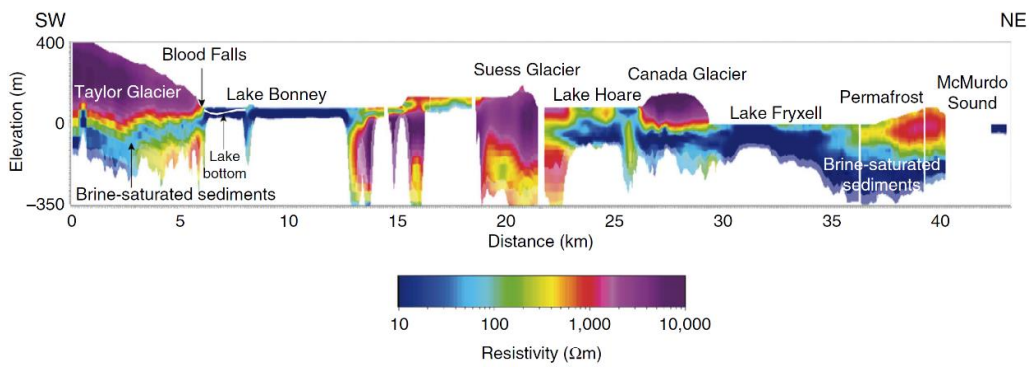

Figure 10 Resistivity profile along the length of the Taylor Valley. Low resistivities near McMurdo Sound to Lake Hoare is interpreted as hydrological connectivity of brine in sediments extending from the coastal margin inland and beneath the Canada Glacier. Taken from Mikucki et al. (2015), (licensed under Creative commons).

3D geological modelling of complex buried-valleys

While it is no surprise that AEM can be used in remote, uninhabitable areas, it can also be used successfully in areas with significant infrastructure like Denmark. Høyer et al. (2015) demonstrate how AEM data can be used to generate 3D models of complex buried-valley structures as seen in Figure 11, when the data are properly processed and the survey system properly accounted for.

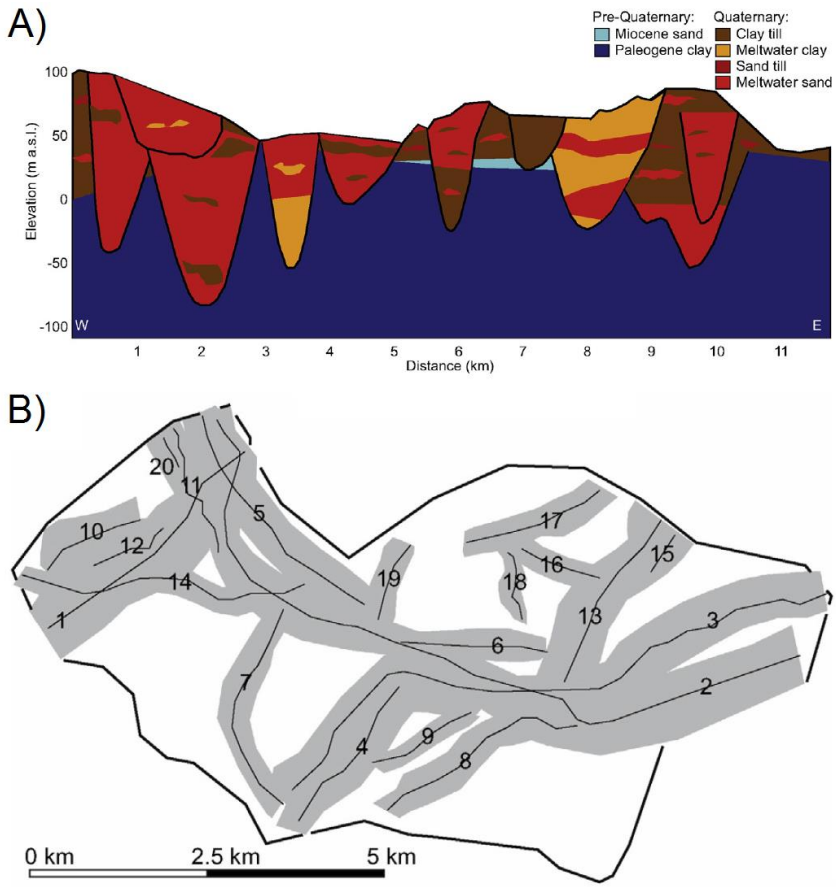

Figure 11 3D geological mapping of buried valleys. A) A profile sketch illustrating the conceptual model of the study area. B) Map of the interpreted buried valleys. The grey shadings show the extent of the valleys, whereas the lines mark the thalwegs for the individual valleys. Valley numbers are written on the figure. From Høyer et al. (2015), (licensed under Creative commons).

Environmental assessments and hydrologic mapping in Africa

A problem with some of the more powerful AEM systems has been that they do not properly remove or compensate for the primary field. While there have been significant improvements in the last decade, Podgorski et al. (2013) demonstrate on a survey from Botswana how even old surveys, with proper and careful processing, can be used for hydrologic mapping. In the paper, they demonstrate how a recalibrated signal goes from a root-mean-square error of 14.67 % to 0.51 %, as seen in Figure 12.

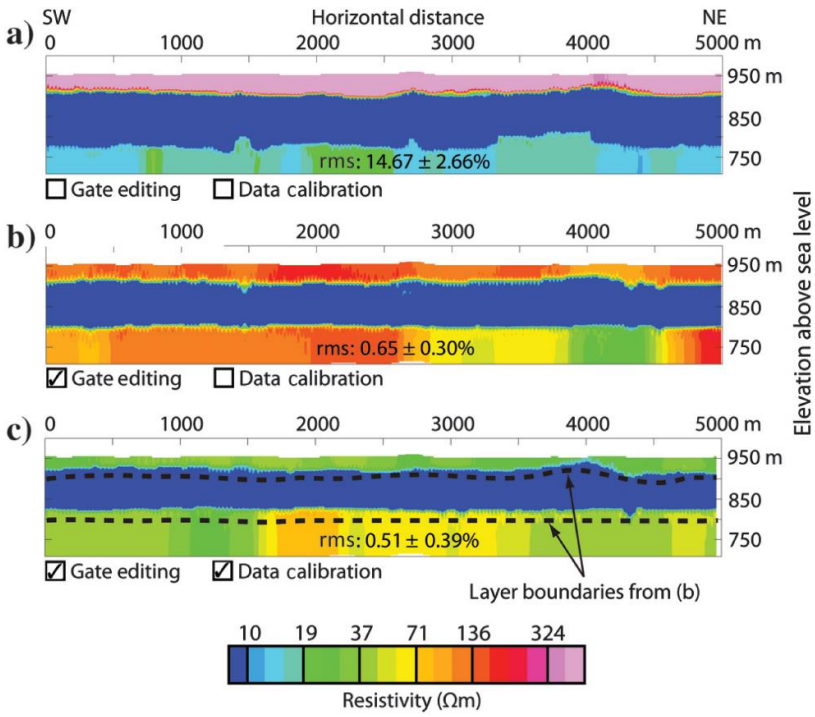

Figure 12 Inverted resistivity profile models. "Gate editing" refers to the removal of early gates affected by residual transmitter current and the elimination of noisy late gates. "Data calibration" refers to the incorporation of a 30 µs time shift and a 1.44 multiplicative amplitude factor. a) shows the resulting model without Gate editing or Data calibration. b) shows the resulting model with Gate editing. c) shows the resulting model with Gate editing and Data calibration. From Podgorski et al. (2013).

Measurements of a collapse-prone volcano

The danger from volcanoes is commonly associated with eruptions. However, another less known risk is catastrophic collapses the can lead to massive destructive debris flow. Finn et al. (2007) describe how hydrothermally altered rocks can lead to collapses, especially if they are water saturated. In the paper, they have conducted an AEM survey on Mount Adams, near Salt Creek Lahar, USA. Through the use of both EM data and magnetic data, they are able to find and map the regions that have hydrothermally been altered, as seen in Figure 13. From this, they predict the most likely places for a future collapse, as well as the scope of a collapse.

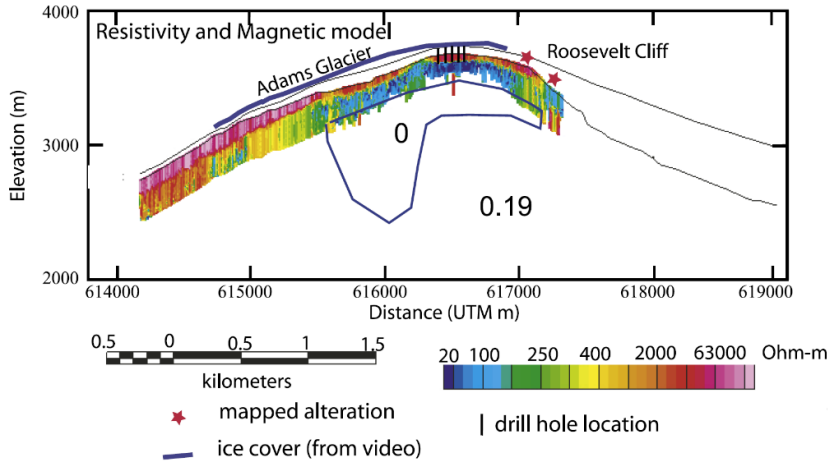

Figure 13 Resistivity and magnetic models. Thick blue lines indicate the extent of glacial ice. The blue area indicate a nonmagnetic region ("0" and "0.19" indicate the magnetic susceptibilities in these areas). Red stars indicate regions of mapped alteration, vertical black lines indicate the location of drill holes, and the blue outline (bottom) shows distribution of thick (>350 m) nonmagnetic material. From Finn et al. (2007), (courtesy of Wiley).

7. Conclusion & Outlook

AEM has developed rapidly within the last decade; both survey systems, but also their corresponding interpretive software. As the method develops, more and more applications become viable, as is apparent by the case examples given in this review. These applications require finesse in order to discriminate some of the low-conductivity contrasts presented, as well as a robust system capable of operating in some of the most hostile climates we have on this planet.

In the last decade HTEM systems have firmly established themselves as the system of choice for most applications. Looking at the latest developments presented by the various companies it is clear that they are becoming increasingly aware of the importance of early time information and are all investing considerable research in pushing for the earlier time-gate measurements.

Another exciting prospect is that currently advanced 3D EM modelling tools are available and actively developed using online distributed repositories. This enables various academic groups to work on the same software, instead of each group having to develop their own. Furthermore, it makes the software more persistent to the flux of people entering and leaving academia.

The vision in AEM modelling is a code that can directly take the survey data, automatically and objectively process the data, perform an appropriate inversion of the data and automatically transform the resistivity maps to a geological map. While no code capable of this yet exists, we are starting to see the various building blocks towards reaching that goal. Andersen et al. (2016) demonstrated how neural networks can be used to partly automate the processing, while Friedel et al. (2016) have shown how real-time geological interpretation can be accomplished using machine learning. Ullmann et al. (2016) and Scheunert et al. (2016) have demonstrated a method that automatically selects an appropriate modelling scheme. Thus the building blocks are there, though they will likely need further refinement and then finally to be combined before the vision comes alive. So while there is still a long way to go, it does not seem impossible that such codes could emerge in the coming decade.

8. Bibliography

Abraham, J.D., Cannia, J.C., Bedrosian, P.A., Johnson, M.R., Ball, L.B. & Sibray, S.S. 2012. Airborne electromagnetic mapping of the base of aquifer in areas of western Nebraska. US Geological Survey.

Abubakar, A., Habashy, T.M., Druskin, V.L., Knizhnerman, L. & Alumbaugh, D. 2008. 2.5 D forward and inverse modeling for interpreting low-frequency electromagnetic measurements. *Geophysics* **73**, F165-F177.

Allard, M. 2007. On the origin of the HTEM species. *Advances in Airborne Geophysics* **7**, 355-374.

Amestoy, P.R., Duff, I.S., L'Excellent, J.-Y. & Koster, J. 2001. A fully asynchronous multifrontal solver using distributed dynamic scheduling. *SIAM Journal on Matrix Analysis and Applications* **23**, 15-41.

Andersen, K.K., Kirkegaard, C., Foged, N., Christiansen, A.V. & Auken, E. 2016. Artificial neural networks for removal of couplings in airborne transient electromagnetic data. *Geophysical Prospecting* **64**, 741-752.

Andersen, K.K., Nyboe, N.S., Kirkegaard, C., Auken, E. & Christiansen, A.V. 2015. A system response convolution routine for improved near surface sensitivity in SkyTEM data. *First European Airborne Electromagnetics Conference*.

Ansari, S., Farquharson, C. & MacLachlan, S. 2017. A gauged finite-element potential formulation for accurate inductive and galvanic modelling of 3-D electromagnetic problems. *Geophysical Journal International* **210**, 105-129.

Auken, E. & Christiansen, A.V. 2004. Layered and laterally constrained 2D inversion of resistivity data. *Geophysics* **69**, 752-761.

Auken, E., Christiansen, A.V., Jacobsen, L.H. & Sørensen, K.I. 2008. A resolution study of buried valleys using laterally constrained inversion of TEM data. *Journal of Applied Geophysics* **65**, 10-20.

Auken, E., Christiansen, A.V., Kirkegaard, C., Andersen, K., Finadaca, G., Sørensen, K. & Nyboe, N. 2015. An overview of the newest SkyTEM and inversion technologies with focus on resolution of shallow geological layers. *EAGE/DGG Workshop on Airborne Geophysics 2015*.

Auken, E., Christiansen, A.V., Kirkegaard, C., Fiandaca, G., Schamper, C., Behroozmand, A.A., Binley, A., Nielsen, E., Effersø, F., Christensen, N.B. & others. 2014. An overview of a highly versatile forward and stable inverse algorithm for airborne, ground-based and borehole electromagnetic and electric data. *Exploration Geophysics* **46**, 223-235.

Balch, S., Boyko, W. & Paterson, N. 2003. The AeroTEM airborne electromagnetic system. *The Leading Edge* **22**, 562-566.

Ball, L.B., Smith, B.D., Minsley, B.J., Abraham, J.D., Voss, C.I., Astley, B.N., Deszcz-Pan, M. & Cannia, J.C. 2011. Airborne electromagnetic and magnetic geophysical survey data of the Yukon Flats and Fort Wainwright areas, central Alaska, June 2010. US Geological Survey, ISBN 2331-1258.

Bedrosian, P.A., Schamper, C. & Auken, E. 2016. A comparison of helicopter-borne electromagnetic systems for hydrogeologic studies. *Geophysical Prospecting* **64**, 192-215.

Bezanson, J., Karpinski, S., Shah, V.B. & Edelman, A. 2012. Julia: A fast dynamic language for technical computing. *arXiv preprint arXiv:1209.5145*.

Bin, C.H.E.N., Li-Feng, M.A.O. & Guang-Ding, L.I.U. 2014. Estimating Penetration Depth of the CHTEM-I System by the Diffusive Electric Field Method. *Chinese Journal of Geophysics* **57**, 112-119.

Boesen, T., Auken, E., Christiansen, A.V., Fiandaca, G., Kirkegaard, C., Pfaffhuber, A. & Vøge, M. 2017. An efficient 2D inversion scheme for airborne frequency domain data. *submitted to Geophysics*.

Bournas, N., Taylor, S., Prikhodko, A., Plastow, G., Kwan, K., Legault, J. & Berardelli, P. 2017. Superparamagnetic effects discrimination in VTEM data of Greenland using multiple criteria and predictive approaches. *Journal of Applied Geophysics* **145**, 59-73.

Brodie, R. 2012. Appendix 3: GA-LEI inversion of TEMPEST data. *The Frome airborne electromagnetic survey, South Australia: implications for energy, minerals and regional geology: Geoscience Australia Record*, 278-287.

Brodie, R. & Sambridge, M. 2006. A holistic approach to inversion of frequency-domain airborne EM data. *Geophysics* **71**, G301-G312.
Brodie, R. & Sambridge, M. 2009a. An example of holistic inversion of time domain AEM data. *ASEG Extended Abstracts* **2009**, 1-9.
Brodie, R. & Sambridge, M. 2009b. Holistic inversion of frequency-domain airborne electromagnetic data with minimal prior information. *Exploration Geophysics* **40**, 8-16.
Brodie, R.C. & Richardson, M. 2013. AEM system target resolvability analysis using a Monte Carlo inversion algorithm. In: *ASEG Extended Abstracts 2013*, pp. 1-4. Australian Society of Exploration Geophysicists (ASEG).
Brodie, R.C. & Sambridge, M. 2012. Transdimensional Monte Carlo inversion of AEM data. *ASEG Extended Abstracts* **2012**, 1-4.
Börner, R.-U. 2010. Numerical modelling in geo-electromagnetics: advances and challenges. *Surveys in Geophysics* **31**, 225-245.
Börner, R.-U., Ernst, O.G. & Güttel, S. 2015. Three-dimensional transient electromagnetic modelling using Rational Krylov methods. *Geophysical Journal International* **202**, 2025-2043.
Börner, R.-U., Ernst, O.G. & Spitzer, K. 2008. Fast 3-D simulation of transient electromagnetic fields by model reduction in the frequency domain using Krylov subspace projection. *Geophysical Journal International* **173**, 766-780.
Cai, H., Hu, X., Xiong, B., Auken, E., Han, M. & Li, J. 2017. Finite element time domain modeling of controlled-Source electromagnetic data with a hybrid boundary condition. *Journal of Applied Geophysics* **145**, 133-143.
Caudillo-Mata, L.A., Haber, E., Heagy, L.J. & Schwarzbach, C. 2016. A Framework for the Upscaling of the Electrical Conductivity in the Quasi-static Maxwell's Equations. *Journal of Computational and Applied Mathematics* **317**, 388-402.
Chang-Chun, Y., Xiu-Yan, R., Yun-He, L., Yan-Fu, Q., Chang-Kai, Q. & Jing, C. 2015. Review on airborne electromagnetic inverse theory and applications. *Geophysics* **80**, W17-W31.
Chen, T., Hodges, G. & Miles, P. 2014. MULTIPULSE--high resolution and high power in one TDEM system. *Exploration Geophysics* **46**, 49-57.
Chikazumi, S. & Graham, C.D. 2009. *Physics of Ferromagnetism 2e.* Oxford University Press on Demand, ISBN 0199564817.
Christensen, N.B. 2016a. Fast approximate 1D modelling and inversion of transient electromagnetic data. *Geophysical Prospecting* **64**, 1620-1631.
Christensen, N.B. 2016b. Strictly horizontal lateral parameter correlation for 1D inverse modelling of large datasets. *Near Surface Geophysics* **14**, 403-411.
Christensen, N.B., Reid, J.E. & Halkjær, M. 2009. Fast, laterally smooth inversion of airborne time-domain electromagnetic data. *Near Surface Geophysics* **7**, 599-612.
Christensen, N.B. & Tølbøll, R.J. 2009. A lateral model parameter correlation procedure for one-dimensional inverse modelling. *Geophysical Prospecting* **57**, 919-929.
Christensen, N.K., Ferre, T.P.A., Fiandaca, G. & Christensen, S. 2017. Voxel inversion of airborne electromagnetic data for improved groundwater model construction and prediction accuracy. *Hydrology and Earth System Sciences* **21**, 1321.
Christiansen, A.V. & Auken, E. 2012. A global measure for depth of investigation. *Geophysics* **77**, WB171-WB177.
Christiansen, A.V., Auken, E., Kirkegaard, C., Schamper, C. & Vignoli, G. 2016a. An efficient hybrid scheme for fast and accurate inversion of airborne transient electromagnetic data. *Exploration Geophysics* **47**, 323-330.
Christiansen, A.V., Auken, E., Ley-Cooper, A.Y. & Andersen, K.R. Year. Quantifying the Effect of Primary Field Modelling on TEMPEST Data—The Importance of Uncertainty. Conference Quantifying the Effect of Primary Field Modelling on TEMPEST Data—The Importance of Uncertainty, 719-723.

Christiansen, A.V., Auken, E. & Viezzoli, A. 2011. Quantification of modeling errors in airborne TEM caused by inaccurate system description. *Geophysics* **76**, F43-F52.

Cockett, R., Kang, S., Heagy, L.J., Pidlisecky, A. & Oldenburg, D.W. 2015. SimPEG: An open source framework for simulation and gradient based parameter estimation in geophysical applications. *Computers & Geosciences* **85**, 142-154.

Combrinck, M. & Wright, R. 2016. XciteTM: Great results require more than good data.

Constable, S.C., Parker, R.L. & Constable, C.G. 1987. Occam's inversion: A practical algorithm for generating smooth models from electromagnetic sounding data. *Geophysics* **52**, 289-300.

Cox, L.H., Wilson, G.A. & Zhdanov, M.S. 2010. 3D inversion of airborne electromagnetic data using a moving footprint. *Exploration Geophysics* **41**, 250-259.

Cox, L.H., Wilson, G.A. & Zhdanov, M.S. 2012. 3D inversion of airborne electromagnetic data. *Geophysics* **77**, WB59-WB69.

Cuthill, E. & McKee, J. 1969. Reducing the bandwidth of sparse symmetric matrices. *Proceedings of the 1969 24th national conference*, 157-172.

Eadie, T., Legault, J., Plastow, G., Prikhodko, A. & Tishin, P. 2017. An Improved Helicopter Time-domain EM System for Near Surface Applications. *Second European Airborne Electromagnetics Conference*.

Everett, M.E. 2012. Theoretical developments in electromagnetic induction geophysics with selected applications in the near surface. *Surveys in Geophysics* **33**, 29-63.

Farquharson, C.G. & Oldenburg, D.W. 1998. Non-linear inversion using general measures of data misfit and model structure. *Geophysical Journal International* **134**, 213-227.

Fiandaca, G., Christiansen, A.V. & Auken, E. 2015. Depth of investigation for multi-parameters inversions. *Near Surface Geoscience 2015-21st European Meeting of Environmental and Engineering Geophysics*.

Finn, C.A., Deszcz-Pan, M., Anderson, E.D. & John, D.A. 2007. Three-dimensional geophysical mapping of rock alteration and water content at Mount Adams, Washington: Implications for lahar hazards. *Journal of Geophysical Research: Solid Earth* **112**, 1-21.

Friedel, M.J., Esfahani, A. & Iwashita, F. 2016. Toward real-time three-dimensional mapping of surficial aquifers using a hybrid modeling approach. *Hydrogeology Journal* **24**, 211-229.

Gisselø, P. & Nyboe, N. 2017. SkyTEM High Power Systems–A New Generation of Airborne TEM Transmitters. *Second European Airborne Electromagnetics Conference*.

Gould, N.I.M., Scott, J.A. & Hu, Y. 2007. A numerical evaluation of sparse direct solvers for the solution of large sparse symmetric linear systems of equations. *ACM Transactions on Mathematical Software (TOMS)* **33**, 10.

Guillemoteau, J., Sailhac, P. & Béhaegel, M. 2011. Regularization strategy for the layered inversion of airborne transient electromagnetic data: application to in-loop data acquired over the basin of Franceville (Gabon). *Geophysical Prospecting* **59**, 1132-1143.

Haber, E. 2004. Quasi-Newton methods for large-scale electromagnetic inverse problems. *Inverse Problems* **21**, 305-323.

Haber, E., Ascher, U.M. & Oldenburg, D.W. 2004. Inversion of 3D electromagnetic data in frequency and time domain using an inexact all-at-once approach. *Geophysics* **69**, 1216-1228.

Haber, E. & Heldmann, S. 2007. An octree multigrid method for quasi-static Maxwell's equations with highly discontinuous coefficients. *Journal of Computational Physics* **223**, 783-796.

Haber, E., Oldenburg, D.W. & Shekhtman, R. 2007. Inversion of time domain three-dimensional electromagnetic data. *Geophysical Journal International* **171**, 550-564.

Haber, E. & Schwarzbach, C. 2014. Parallel inversion of large-scale airborne time-domain electromagnetic data with multiple OcTree meshes. *Inverse Problems* **30**, 1-28.

Heagy, L.J., Cockett, R., Kang, S., Rosenkjaer, G.K. & Oldenburg, D.W. 2016. A framework for simulation and inversion in electromagnetics. *arXiv preprint arXiv:1610.00804*.

Hestenes, M.R. & Stiefel, E. 1952. *Methods of conjugate gradients for solving linear systems.* NBS.

Hine, K. & Macnae, J. 2016. Comparing induced polarization responses from airborne inductive and galvanic ground systems: Lewis Ponds, New South Wales. *Geophysics* **81**, B179-B188.

Hiptmair, R. 1998. Multigrid method for Maxwell's equations. *SIAM Journal on Numerical Analysis* **36**, 204-225.

Hunkeler, P.A., Hendricks, S., Hoppmann, M., Farquharson, C.G., Kalscheuer, T., Grab, M., Kaufmann, M.S., Rabenstein, L. & Gerdes, R. 2015. Improved 1D inversions for sea ice thickness and conductivity from electromagnetic induction data: Inclusion of nonlinearities caused by passive bucking. *Geophysics* **81**, WA45-WA58.

Høyer, A.-S., Jørgensen, F., Sandersen, P., Viezzoli, A. & Møller, I. 2015. 3D geological modelling of a complex buried-valley network delineated from borehole and AEM data. *Journal of Applied Geophysics* **122**, 94-102.

Kaminski, V. & Viezzoli, A. 2017. Modeling induced polarization effects in helicopter time-domain electromagnetic data: Field case studies. *Geophysics* **82**, B49-B61.

Kang, S. & Oldenburg, D.W. 2015. Recovering IP information in airborne-time domain electromagnetic data. *ASEG Extended Abstracts* **2015**, 1-4.

Kang, S. & Oldenburg, D.W. 2016. On recovering distributed IP information from inductive source time domain electromagnetic data. *Geophysical Journal International* **207**, 174-196.

Killeen, P.G. 2013. Exploration Trends and Developments in 2012. *The Northern Miner*.

Killeen, P.G. 2014. Exploration Trends and Developments in 2013. *The Northern Miner*.

Kirkegaard, C., Andersen, K., Boesen, T., Christiansen, A.V., Auken, E. & Fiandaca, G. 2015a. Utilizing massively parallel co-processors in the AarhusInv 1D forward and inverse AEM modelling code. *ASEG Extended Abstracts* **2015**, 1-3.

Kirkegaard, C., Andersen, K., Christiansen, A.V., Auken, E. & Boesen, T. 2015b. Rapid Inversion of Large Airborne AEM Data Datasets Utilizing Massively Parallel Co-processors. *First European Airborne Electromagnetics Conference*.

Kirkegaard, C. & Auken, E. 2015. A parallel, scalable and memory efficient inversion code for very large-scale airborne electromagnetics surveys. *Geophysical Prospecting* **63**, 495-507.

Kirsch, R., Rabbel, W., Ernstson, K., Börner, F., Siemon, B., Christiansen, A.V., Auken, E., Sørensen, K., Blindow, N., Yaramanci, U., Hertrich, M., Tezkan, B., Gabriel, G., Dietrich, P., Leven, C. & Berthold, S. 2009. *Groundwater geophysics - a tool for hydrogeology.* Springer.

Kratzer, T. 2013. Late-time effects in airborne EM: induced polarisation, superparamagnetism and rotation.

Kratzer, T., Macnae, J. & Mutton, P. 2013. Detection and correction of SPM effects in airborne EM surveys. *Exploration Geophysics* **44**, 6-15.

Lane, R., Green, A., Golding, C., Owers, M., Pik, P., Plunkett, C., Sattel, D. & Thorn, B. 2000. An example of 3D conductivity mapping using the TEMPEST airborne electromagnetic system. *Exploration Geophysics* **31**, 162-172.

Legault, J.M. 2015. Airborne Electromagnetic Systems--State of the Art and Future Directions. *CSEG Recorder* **40**, 38-49.

Legault, J.M., Prikhodko, A., Dodds, D., Macnae, J.C. & Oldenborger, G.A. 2012. Results of recent VTEM helicopter system development testing over the Spiritwood Valley aquifer, Manitoba. *25th Symposium on the Application of Geophpysics to Engineering & Environmental Problems*.

Lelièvre, P.G., Oldenburg, D.W. & Williams, N.C. 2009. Integrating geological and geophysical data through advanced constrained inversions. *Exploration Geophysics* **40**, 334-341.

Lewis, A.S. & Overton, M.L. 2013. Nonsmooth optimization via quasi-Newton methods. *Mathematical Programming* **141**, 135-163.

Ley-Cooper, A.Y., Macnae, J. & Viezzoli, A. 2010. Breaks in lithology: Interpretation problems when handling 2D structures with a 1D approximation. *Geophysics* **75**, WA179-WA188.

Ley-Cooper, A.Y., Viezzoli, A., Guillemoteau, J., Vignoli, G., Macnae, J., Cox, L. & Munday, T. 2014. Airborne electromagnetic modelling options and their consequences in target definition. *Exploration Geophysics* **46**, 74-84.

Li, W.-B., Zeng, Z.-F., Li, J., Chen, X., Wang, K. & Xia, Z. 2016. 2.5 D forward modeling and inversion of frequency-domain airborne electromagnetic data. *Applied Geophysics* **13**, 37-47.

Macnae, J. 2016a. Fitting superparamagnetic and distributed Cole-Cole parameters to airborne electromagnetic data: A case history from Quebec. *Geophysics* **81**, B211-B220.

Macnae, J. 2016b. Quantitative estimation of intrinsic induced polarization and superparamagnetic parameters from airborne electromagnetic data. *Geophysics* **81**, E433-E446.

Macnae, J., King, A., Stolz, N., Osmakoff, A. & Blaha, A. 1998. Fast AEM data processing and inversion. *Exploration Geophysics* **29**, 163-169.

Marchant, D. 2015. Induced polarization effects in inductive source electromagnetic data. University of British Columbia.

Marchant, D., Haber, E. & Oldenburg, D.W. 2012. Inductive source induced polarization. *Geophysical Journal International* **192**, 602-612.

Marchant, D., Haber, E. & Oldenburg, D.W. 2014. Three-dimensional modeling of IP effects in time-domain electromagnetic data. *Geophysics* **79**, E303-E314.

Mikucki, J.A., Auken, E., Tulaczyk, S., Virginia, R.A., Schamper, C., Sørensen, K.I., Doran, P.T., Dugan, H. & Foley, N. 2015. Deep groundwater and potential subsurface habitats beneath an Antarctic dry valley. *Nature communications* **6**.

Minsley, B.J. 2011. A trans-dimensional Bayesian Markov chain Monte Carlo algorithm for model assessment using frequency-domain electromagnetic data. *Geophysical Journal International* **187**, 252-272.

Minsley, B.J., Abraham, J.D., Smith, B.D., Cannia, J.C., Voss, C.I., Jorgenson, M.T., Walvoord, M.A., Wylie, B.K., Anderson, L. & Ball, L.B. 2012. Airborne electromagnetic imaging of discontinuous permafrost. *Geophysical Research Letters* **39**, 1-8.

Minsley, B.J., Kass, M.A., Hodges, G. & Smith, B.D. 2014. Multielevation calibration of frequency-domain electromagnetic data. *Geophysics* **79**, E201-E216. 10.1190/geo2013-0320.1

Minsley, B.J., Wellman, T.P., Walvoord, M.A. & Revil, A. 2015. Sensitivity of airborne geophysical data to sublacustrine and near-surface permafrost thaw. *The Cryosphere* **9**, 781-794.

Mulder, W.A. 2008. Geophysical modelling of 3D electromagnetic diffusion with multigrid. *Computing and Visualization in Science* **11**, 129-138.

Mulè, S., Miller, R., Carey, H. & Lockwood, R. 2012. Review of three airborne EM systems. *ASEG Extended Abstracts* **2012**, 1-5.

Nash, S.G. & Nocedal, J. 1991. A numerical study of the limited memory BFGS method and the truncated-Newton method for large scale optimization. *SIAM Journal on Optimization* **1**, 358-372.

Nyboe, N. & Mai, S. 2017. Recent Advances in Skytem Receiver System Technologies. *Second European Airborne Electromagnetics Conference*.

Nyboe, N.S. & Sørensen, K. 2012. Noise reduction in TEM: Presenting a bandwidth-and sensitivity-optimized parallel recording setup and methods for adaptive synchronous detection. *Geophysics* **77**, E203-E212.

Oldenburg, D.W., Haber, E. & Shekhtman, R. 2012. Three dimensional inversion of multisource time domain electromagnetic data. *Geophysics* **78**, E47-E57.

Oldenburg, D.W. & Li, Y. 1999. Estimating depth of investigation in DC resistivity and IP surveys. *Geophysics* **64**, 403-416.

Pastick, N.J., Jorgenson, M.T., Wylie, B.K., Minsley, B.J., Ji, L., Walvoord, M.A., Smith, B.D., Abraham, J.D. & Rose, J.R. 2013. Extending airborne electromagnetic surveys for regional active layer and permafrost mapping with remote sensing and ancillary data, Yukon Flats Ecoregion, Central Alaska. *Permafrost and Periglacial Processes* **24**, 184-199.

Pedersen, J.B., Schaars, F.W., Christiansen, A.V., Foged, N., Schamper, C., Rolf, H. & Auken, E. 2017. Mapping the fresh-saltwater interface in the coastal zone using high-resolution airborne electromagnetics. *First Break* **35**, 57-61.

Pfaffhuber, A.A., Hendricks, S., Hunkeler, P. & Kvistedal, Y. 2012. Introducing a new generation multi-sensor airborne system for mapping sea ice cover of polar oceans. *First Break* **30**.

Pfaffhuber, A.A., Lysdahl, A.O., Sørmo, E., Skurdal, G.H., Thomassen, T., Anschütz, H. & Scheibz, J. 2017a. Delineating hazardous material without touching—AEM mapping of Norwegian alum shale. *First Break* **35**, 35-39.

Pfaffhuber, A.A., Persson, L., Lysdahl, A.O., Kåsin, K., Anschütz, H., Bastani, M., Bazin, S. & Löfroth, H. 2017b. Integrated scanning for quick clay with AEM and ground-based investigations. *First Break* **35**, 73-79.

Podgorski, J.E., Auken, E., Schamper, C., Christiansen, A.V., Kalscheuer, T. & Green, A.G. 2013. Processing and inversion of commercial helicopter time-domain electromagnetic data for environmental assessments and geologic and hydrologic mapping. *Geophysics* **78**. https://doi.org/10.1190/geo2012-0452.1

Press, W.H., Teukolsky, S.A., Vetterling, W.T. & Flannery, B.P. 1992. Numerical recipes in Fortran 77: the art of scientific computing. Cambridge university press.

Prikhodko, A., Legault, J.M., Kwan, K., Eadie, T., Oldenborger, G.A., Sapia, V., Viezzoli, A., Gloaguen, E., Smith, B.D. & Best, M.E. 2013. Recent AEM case study examples using a Full Waveform time-domain system for near-surface applications. *Symposium on the Application of Geophysics to Engineering and Environmental Problems 2013*, 377-386.

Puzyrev, V., Koric, S. & Wilkin, S. 2016. Evaluation of parallel direct sparse linear solvers in electromagnetic geophysical problems. *Computers & Geosciences* **89**, 79-87.

Rankka, K., Andersson-Sköld, Y., Hultén, C., Larsson, R., Leroux, V. & Dahlin, T. 2004. Quick clay in Sweden. *Swedish Geotechnical Institute Report* **65**, 145.

Rasmussen, S., Nyboe, N.S., Mai, S. & Larsen, J.J. 2017. Noise Properties of Fourier Deconvolution for Time-Domain EM Soundings. *Geophysics* **82**, 1-39.

Reninger, P.-A., Martelet, G., Deparis, J., Perrin, J.e. & Chen, Y. 2011. Singular value decomposition as a denoising tool for airborne time domain electromagnetic data. *Journal of Applied Geophysics* **75**, 264-276.

Ruthotto, L., Treister, E. & Haber, E. 2016. jInv--a flexible Julia package for PDE parameter estimation. *arXiv preprint arXiv:1606.07399*.

Sattel, D. & Battig, E. 2016. Reprocessing streaming MEGATEM data for square-wave EM, VLF, and AFMAG responses. In: *SEG Technical Program Expanded Abstracts 2016*, pp. 2144-2148. Society of Exploration Geophysicists, ISBN 1949-4645.

Sattel, D. & Mutton, P. 2014. Modelling the superparamagnetic response of AEM data. *Exploration Geophysics* **46**, 118-129.

Schamper, C., Auken, E. & Sørensen, K. 2014. Coil response inversion for very early time modelling of helicopter-borne time-domain electromagnetic data and mapping of near-surface geological layers. *Geophysical Prospecting* **62**, 658-674.

Schenk, O., Gärtner, K. & Fichtner, W. 2000. Efficient sparse LU factorization with left-right looking strategy on shared memory multiprocessors. *BIT Numerical Mathematics* **40**, 158-176.

Scheunert, M., Ullmann, A., Afanasjew, M., Börner, R.-U., Siemon, B. & Spitzer, K. 2016. A cut-&-paste strategy for the 3-D inversion of helicopter-borne electromagnetic data-I. 3-D inversion using the explicit Jacobian and a tensor-based formulation. *Journal of Applied Geophysics* **129**, 209-221.

Siemon, B., Auken, E. & Christiansen, A.V. 2009. Laterally constrained inversion of helicopter-borne frequency-domain electromagnetic data. *Journal of Applied Geophysics* **67**, 259-268.

Smiarowski, A. & Macnae, J. 2013. Detection of a perfect conductor with an airborne electromagnetic system: The Gemini Field Test. *Geophysics* **78**, E249-E259.

Smith, R. 2014. Electromagnetic induction methods in mining geophysics from 2008 to 2012. *Surveys in Geophysics* **35**, 123-156.

Smith, R.S. & Klein, J. 1996. A special circumstance of airborne induced-polarization measurements. *Geophysics* **61**, 66-73.

Spies, B.R. 1989. Depth of investigation in electromagnetic sounding methods. *Geophysics* **54**, 872-888.

Steuer, A., Siemon, B. & Auken, E. 2009. A comparison of helicopter-borne electromagnetics in frequency- and time-domain at the Cuxhaven valley in Northern Germany. *Journal of Applied Geophysics* **67**, 194-205.

Stoyer, C.H. & Greenfield, R.J. 1976. Numerical solutions of the response of a two-dimensional earth to an oscillating magnetic dipole source. *Geophysics* **41**, 519-530.

Sørensen, K.I. & Auken, E. 2004. SkyTEM--a new high-resolution helicopter transient electromagnetic system. *Exploration Geophysics* **35**, 194-202.

Saad, Y. 2003. *Iterative methods for sparse linear systems.* Siam, ISBN 0898715342.

Ullmann, A., Scheunert, M., Afanasjew, M., Börner, R.-U., Siemon, B. & Spitzer, K. 2016. A cut-&-paste strategy for the 3-D inversion of helicopter-borne electromagnetic data-II. Combining regional 1-D and local 3-D inversion. *Journal of Applied Geophysics* **130**, 131-144.

Van der Vorst, H.A. 1992. Bi-CGSTAB: A fast and smoothly converging variant of Bi-CG for the solution of nonsymmetric linear systems. *SIAM Journal on scientific and Statistical Computing* **13**, 631-644.

Viezzoli, A., Christiansen, A.V., Auken, E. & Sørensen, K. 2008. Quasi-3D modeling of airborne TEM data by spatially constrained inversion. *Geophysics* **73**, F105-F113. https://doi.org/10.1190/1.2895521

Viezzoli, A., Kaminskiy, V. & Fiandaca, G. 2017. Modeling induced polarization effects in helicopter time domain electromagnetic data: Synthetic case studies. *Geophysics* **82**, E31-E50.

Viezzoli, A., Munday, T., Auken, E. & Christiansen, A.V. 2010. Accurate quasi 3D versus practical full 3D inversion of AEM data–the Bookpurnong case study. *Preview* **2010**, 23-31.

Vignoli, G., Fiandaca, G., Christiansen, A.V., Kirkegaard, C. & Auken, E. 2015. Sharp spatially constrained inversion with applications to transient electromagnetic data. *Geophysical Prospecting* **63**, 243-255.

Vöge, M., Pfaffhuber, A., Auken, E., Kirkegaard, C., Boesen, T., Hendricks, S. & Hunkeler, P. 2015. 2.5 D Inversion of Sea Ice Thickness from Helicopter EM Data. *First European Airborne Electromagnetics Conference*.

Ward, S.H. & Hohmann, G.W. 1988. Electromagnetic theory for geophysical applications. *Electromagnetic methods in applied geophysics* **1**, 131-311.

Weidelt, P. 1982. Response characteristics of coincident loop transient electromagnetic systems. *Geophysics* **47**, 1325-1330.

Wilson, G.A., Cox, L.H., Čuma, M. & Zhdanov, M.S. 2012. Inverting airborne geophysical data for mega-cell and giga-cell 3D Earth models. *The Leading Edge* **31**, 316-321.

Yang, D. & Oldenburg, D.W. 2012a. Practical 3D inversion of large airborne time domain electromagnetic data sets. *ASEG Extended Abstracts* **2012**, 1-4.

Yang, D. & Oldenburg, D.W. 2012b. Three-dimensional inversion of airborne time-domain electromagnetic data with applications to a porphyry deposit. *Geophysics* **77**, B23-B34.

Yang, D., Oldenburg, D.W. & Haber, E. 2014. 3-D inversion of airborne electromagnetic data parallelized and accelerated by local mesh and adaptive soundings. *Geophysical Journal International* **196**, 1492-1507.

Yin, C. & Hodges, G. 2007. Simulated annealing for airborne EM inversion. *Geophysics* **72**, F189-F195. https://doi.org/10.1190/1.2736195

Yin, C., Qi, Y. & Liu, Y. 2016. 3D time-domain airborne EM modeling for an arbitrarily anisotropic earth. *Journal of Applied Geophysics* **131**, 163-178.

Yu, W.W. & Haber, E. 2012. A 2.5 D Inversion of Airborne Electromagnetic data. In: *SEG Technical Program Expanded Abstracts 2012*, pp. 1-5. Society of Exploration Geophysicists.

Appendix B

Paper 2

Submitted to Geophysics.

An efficient 2D inversion scheme for airborne frequency domain data

Authors:

Tue Boesen Tue@geo.au.dk, Aarhus University, Denmark

Esben Auken Esben.auken@geo.au.dk, Aarhus University, Denmark

Anders Vest Christiansen Anders.vest@geo.au.dk, Aarhus University, Denmark

Gianluca Fiandaca gianluca.fiandaca@geo.au.dk , Aarhus University, Denmark

Casper Kirkegaard, Casper.kirkegaard@gmail.com, QIAGEN Aarhus, Denmark

Andreas Aspmo Pfaffhuber Andreas.A.Pfaffhuber@ngi.no, Norwegian Geotechnical Institute, Norway

Malte Vöge Malte.voege@ngi.no, Norwegian Geotechnical Institute

Running head: 2D Hybrid HEM inversion

Corresponding author: Tue Boesen, Aarhus University, Denmark

Email: tue@geo.au.dk

Submission date: 05-05-2017

Key words:

2D, HEM, Hybrid, Finite element, inversion, modelling.

ABSTRACT

In many cases, inversion in 2D gives a better description of the subsurface compared to 1D inversion, but computationally 2D inversion is expensive, and it can be hard to employ for large-scale surveys. We present an efficient hybrid 2D airborne frequency-domain electromagnetic inversion algorithm. Our hybrid scheme combines 1D and 2D inversions in a three-stage process, where each step is progressively more accurate and computationally more expensive than the previous. This results in a $\sim 2x - 6x$ speedup compared to full 2D inversions, and with only minor changes to the inversion results. Our inversion structure is based on a regular grid, where each sounding is discretized individually. The 1D modelling code uses layered models with derivatives derived through the finite difference method, while our 2D modelling code uses an adaptive finite element mesh, and the adjoint-state method to calculate the derivatives. By incorporating the inversion grid structure into the 2D finite element mesh, interpolation between the different meshes becomes trivial. Large surveys are handled by utilizing local meshing to split large surveys into small sections, which retains the 2D information. The algorithm is heavily optimized, and parallelized over both frequencies and sections, with a good scalability even on non-uniform memory architecture systems, on which it is generally hard to achieve a satisfactory scaling. The algorithm has been tested successfully with various synthetic studies as well as field examples, of which results from two synthetic studies and a field example are shown.

INTRODUCTION

Airborne electromagnetic surveys typically contain thousands of line kilometers of data, and are routinely flown for mapping of geology, groundwater, saltwater intrusion, etc. Most data are inverted using 1D model algorithms, which have proven to be robust and computationally fast. However, specific targets with a high conductivity contrast between undulating bedrock and sediments, or conductive sheet-like mineralizations, need higher dimensionality in the underlying model to be resolved accurately (Wilson et al. 2012, Doyle, Kivi, and BH 1999, Yang and Oldenburg 2012b). The challenge in moving beyond 1D modeling is that it is prohibitively computationally expensive to invert for a 2D or a 3D model and this limits the usage of these inversion algorithms on a routine basis, even for frequency domain-electromagnetic datasets of just a few discrete frequencies.

Full 3D EM inversion algorithms have existed for more than a decade (Haber, Oldenburg, and Shekhtman 2007), and with the concept of moving footprint (Cox, Wilson, and Zhdanov 2010), several 3D codes using local meshes have been presented (Cox, Wilson, and Zhdanov 2012, Yang, Oldenburg, and Haber 2014). All these algorithms are capable of handling large surveys, in time- or frequency-domain, by sectioning the survey into smaller parts using a local meshing approach. Local meshing means that the survey is split into smaller parts, where each part contains a small subset of transmitter-receiver pairs, as well as all the models within their footprint domain (Liu and Becker 1990, Beamish 2003, Reid, Pfaffling, and Vrbancich 2006). Here, the footprint is defined as the area of significant lateral sensitivity of the survey system, and its size is thus dependent upon both the system itself and the resistivity of the earth. Reid, Pfaffling, and Vrbancich (2006) showed that, for a frequency domain system, the footprint may be as large as 10 times the flight altitude for low induction numbers. Common survey systems operate either in time-domain, or with multiple frequencies spread across the frequency spectrum, and while these latter systems usually have one transmitter frequency operating within the low induction approximation, the majority of their transmitter frequencies operate at higher induction numbers, for which the footprint is much smaller. From this, we argue that when a survey is flown with a line separation of 200-500 m, the majority of any

crossline information is lost, and the survey results are essentially reduced to only contain inline information. Considering this and the inherent computational burden of doing full 3D inversions, it is clear that there are areas where it is sufficient, and even desirable to operate within a 2D formulation. Several 2D inversion algorithms have been presented over the years: Mitsuhata and Uchida (2002), Wilson, Raiche, and Sugeng (2006), Li et al. (2016), Key and Ovall (2011) have all developed 2D finite element algorithms, while Abubakar et al. (2008) uses a finite difference approach, and Yu and Haber (2012) present a finite volume approach. In general, finite difference approaches are considered the most simple and inaccurate of the three approaches, but can sometimes be justified due to their superior parallel scaling. The finite element is the most accurate of the methods, but also the most computationally heavy, and at large the question of whether the finite element or finite volume is the superior choice remains open (Jahandari, Ansari, and Farquharson 2017).

In this paper, we present a hybrid 1D/2D inversion code for frequency-domain HEM data designed for inverting field scale surveys on desktop computers. Since an efficient 2D modelling algorithm is vital to achieve this goal, and since our 2D algorithm has not previously been published, this paper begins with the construction of our 2D algorithm and the foundation it is built on. The 2D algorithm is based on the 2.5D formulation by Stoyer and Greenfield (1976), along with field separation into primary and secondary fields, where the high frequency singularity is handled by the introduction of a finite resistivity of the air (Mitsuhata 2000). The algorithm has a triangular finite element mesh for the 2D forward and derivative calculations, and a regular grid for the inversion. When having multiple meshes, interpolation schemes are needed to map variables between the meshes. In general, interpolation between meshes is a non-trivial task (Caudillo-Mata et al. 2016), but in our case the task is made trivial, by using the regular grid as a skeletal structure for building the finite element mesh. Due to limited memory, as well as performance concerns, we introduce sectioning, which splits large surveys into smaller sections. Sectioning is only done when carrying out the 2D forward and derivative calculations, during which we enforce sufficient overlap, such that vital 2D information is preserved. Based on the overlap size, we show how section sizes should be

chosen in order to reach optimal performance. The algorithm is built in Fortran/OpenMP, and utilizes Intel MKL libraries, as well as a custom-built block-parallel sparse iterative linear solver. The algorithm is part of AarhusInv, which is provided as freeware for non-commercial academic purposes (Auken et al. 2014).

Following the presentation of our 2D algorithm, we present a hybrid scheme, inspired by the work presented in Christiansen et al. (2015), Christiansen and Auken (2004). The method starts by performing 1D forward and inverse calculations, later it switches to 2D forward calculations and 1D derivatives, and finally it ends with full 2D calculations. The result of this is a code, which produces 2D results, but with a substantially shorter computational time than traditional 2D algorithms. We demonstrate these computational benefits using two synthetic models and a field example. Finally, we discuss the trade-off between computational speed and accuracy, how the algorithm is best parallelized, and we illustrate the code's parallel scaling and performance on a multiprocessor system.

METHODOLOGY

The 2.5D forward algorithm is based upon the framework of Stoyer and Greenfield (1976). In a 2.5D formulation the earth is described in 2D (homogeneous in the cross-section-direction), but the source is 3D. The source needs to be 3D, in order to describe accurately the sources used in AEM, since AEM sources do not produce source fields, which are reasonably homogenous in any direction. Our 2.5D algorithm was originally developed for marine EM measurements (Vöge 2010), but sources in the air have been added so it can now be used to invert airborne frequency domain EM data (Vöge et al. 2015). For hybrid inversion we include the 1D algorithm of Auken et al. (2014), which is based on the layered 1D model solution presented in Ward and Hohmann (1988).

Governing equations

Starting from Maxwell's equations in the frequency domain:

$$\boldsymbol{\nabla} \times \boldsymbol{E} + i\omega\boldsymbol{\mu} \cdot \boldsymbol{H} = 0 \tag{1}$$

$$\nabla \times \boldsymbol{H} - i\omega\boldsymbol{\varepsilon} \cdot \boldsymbol{E} = \boldsymbol{J}, \tag{2}$$

where $\boldsymbol{E}$ and $\boldsymbol{H}$ are the electric- and magnetic-fields, $\boldsymbol{J}$ is the electric source current, i is the imaginary unit, ω is the frequency, $\boldsymbol{\varepsilon}$ is the complex dielectric permittivity, with $\boldsymbol{\varepsilon} = \boldsymbol{\varepsilon_0} - i\frac{\sigma}{\omega}$, and $\boldsymbol{\mu}$ is the magnetic permeability. In order to minimize the forward inaccuracy, the fields are split into primary and secondary fields:

$$\boldsymbol{E} = \boldsymbol{E_p} + \boldsymbol{E_s}, \boldsymbol{H} = \boldsymbol{H}_p + \boldsymbol{H_s}, \tag{3}$$

Where the primary field is computed analytically, and the inaccuracy of the finite element method affects only the secondary field, which is several orders of magnitude smaller than the total field.

Following from equation (1) and (2), the primary field is given as:

$$\boldsymbol{\nabla} \times \boldsymbol{E_p} + i\omega\boldsymbol{\mu} \cdot \boldsymbol{H}_p = 0 \tag{4}$$

$$\boldsymbol{\nabla} \times \boldsymbol{H_p} - i\omega\boldsymbol{\varepsilon} \cdot \boldsymbol{E}_p = \boldsymbol{J}, \tag{5}$$

with the remainder being the secondary fields:

$$\boldsymbol{\nabla} \times \boldsymbol{E_s} + i\omega\boldsymbol{\mu} \cdot \boldsymbol{H}_s = 0 \tag{6}$$

$$\boldsymbol{\nabla} \times \boldsymbol{H}_s - i\omega\boldsymbol{\varepsilon} \cdot \boldsymbol{E_s} = \boldsymbol{\sigma}_s \cdot \boldsymbol{E}_p, \tag{7}$$

where $\boldsymbol{\sigma}$ is the conductivity, and $\boldsymbol{\sigma}_s = \boldsymbol{\sigma} - \boldsymbol{\sigma}_p$. $\boldsymbol{\sigma}_p$ is the conductivity of the primary field model. In our case, we chose the primary field model to be a uniform full-space air model with magnetic point sources and receivers, which can be easily calculated analytically. Since $\boldsymbol{\sigma}_p$ is the conductivity of air, we have $\boldsymbol{\sigma} = \boldsymbol{\sigma}_p$ and $\boldsymbol{\sigma}_s = 0$ in the air layer.

The Fourier transform is defined with respect to y (i.e. the strike direction of the survey) as:

$$\tilde{F}(x, k_y, z) = \int_{-\infty}^{+\infty} F(x, y, z) e^{ik_y y} dy, \tag{8}$$

where k_y is the wavenumber. A Fourier transformation of the primary field is carried out numerically, following the approach of Streich, Becken, and Ritter (2011). The governing equations of the 2D forward response emerge by applying the Fourier transform to equation (6) and (7):

$$\widetilde{E}_{sx} = \frac{1}{k_y^2 - \omega^2 \mu_z \varepsilon_x}\left(ik_y \frac{\partial \widetilde{E}_{sy}}{\partial x} - i\omega\mu_z \frac{\partial \widetilde{H}_{sy}}{\partial z} - i\omega\mu_z \sigma_{sx} \widetilde{E}_{px}\right) \tag{9}$$

$$\widetilde{E}_{sz} = \frac{1}{k_y^2 - \omega^2 \mu_x \varepsilon_z}\left(ik_y \frac{\partial \widetilde{E}_{sy}}{\partial z} + i\omega\mu_x \frac{\partial \widetilde{H}_{sy}}{\partial x} - i\omega\mu_x \sigma_{sz} \widetilde{E}_{pz}\right) \tag{10}$$

$$\widetilde{H}_{sx} = \frac{1}{k_y^2 - \omega^2 \mu_x \varepsilon_z}\left(i\omega\varepsilon_z \frac{\partial \widetilde{E}_{sy}}{\partial z} + ik_y \frac{\partial \widetilde{H}_{sy}}{\partial x} - ik_y \sigma_{sz} \widetilde{E}_{pz}\right) \tag{11}$$

$$\widetilde{H}_{sz} = \frac{1}{k_y^2 - \omega^2 \mu_z \varepsilon_x}\left(-i\omega\varepsilon_x \frac{\partial \widetilde{E}_{sy}}{\partial x} + ik_y \frac{\partial \widetilde{H}_{sy}}{\partial z} + ik_y \sigma_{sx} \widetilde{E}_{px}\right) \tag{12}$$

$$\begin{aligned} -i\omega\varepsilon_y \tilde{E}_{sy} &+ \frac{\partial}{\partial x}\left(\frac{i\omega\varepsilon_x}{c_{zx}} \frac{\partial \tilde{E}_{sy}}{\partial x}\right) + \frac{\partial}{\partial z}\left(\frac{i\omega\varepsilon_z}{c_{xz}} \frac{\partial \tilde{E}_{sy}}{\partial z}\right) - \frac{\partial}{\partial x}\left(\frac{ik_y}{c_{zx}} \frac{\partial \widetilde{H}_{sy}}{\partial z}\right) \\ &+ \frac{\partial}{\partial z}\left(\frac{ik_y}{c_{xz}} \frac{\partial \widetilde{H}_{sy}}{\partial x}\right) \\ &= -\left(i\omega\varepsilon_{py} - i\omega\varepsilon_y\right)\tilde{E}_{py} + \frac{\partial}{\partial x}\left(\left(\frac{i\omega\varepsilon_{px}}{c_{pzx}} - \frac{i\omega\varepsilon_x}{c_{zx}}\right)\frac{\partial \tilde{E}_{py}}{\partial x}\right) \\ &+ \frac{\partial}{\partial z}\left(\left(\frac{i\omega\varepsilon_{pz}}{c_{pxz}} - \frac{i\omega\varepsilon_z}{c_{xz}}\right)\frac{\partial \tilde{E}_{py}}{\partial z}\right) - \frac{\partial}{\partial x}\left(\left(\frac{ik_y}{c_{pzx}} - \frac{ik_y}{c_{zx}}\right)\frac{\partial \widetilde{H}_{py}}{\partial z}\right) \\ &+ \frac{\partial}{\partial z}\left(\left(\frac{ik_y}{c_{pxz}} - \frac{ik_y}{c_{xz}}\right)\frac{\partial \widetilde{H}_{py}}{\partial x}\right), \end{aligned} \tag{13}$$

and

$$-i\omega\mu_y\widetilde{H}_{sy} + \frac{\partial}{\partial x}\left(\frac{i\omega\mu_x}{c_{xz}}\frac{\partial\widetilde{H}_{sy}}{\partial x}\right) + \frac{\partial}{\partial z}\left(\frac{i\omega\mu_z}{c_{zx}}\frac{\partial\widetilde{H}_{sy}}{\partial z}\right) + \frac{\partial}{\partial x}\left(\frac{ik_y}{c_{xz}}\frac{\partial\widetilde{E}_{sy}}{\partial z}\right) \tag{14}$$

$$-\frac{\partial}{\partial z}\left(\frac{ik_y}{c_{zx}}\frac{\partial\widetilde{E}_{sy}}{\partial x}\right)$$

$$= -(i\omega\mu_{py} - i\omega\mu_y)\widetilde{H}_{py} + \frac{\partial}{\partial x}\left(\left(\frac{i\omega\mu_{px}}{c_{pxz}} - \frac{i\omega\mu_x}{c_{xz}}\right)\frac{\partial\widetilde{H}_{py}}{\partial x}\right)$$

$$+\frac{\partial}{\partial z}\left(\left(\frac{i\omega\mu_{pz}}{c_{pzx}} - \frac{i\omega\mu_z}{c_{zx}}\right)\frac{\partial\widetilde{H}_{py}}{\partial z}\right) + \frac{\partial}{\partial x}\left(\left(\frac{ik_y}{c_{pxz}} - \frac{ik_y}{c_{xz}}\right)\frac{\partial\widetilde{E}_{py}}{\partial z}\right)$$

$$-\frac{\partial}{\partial z}\left(\left(\frac{ik_y}{c_{pzx}} - \frac{ik_y}{c_{zx}}\right)\frac{\partial\widetilde{E}_{py}}{\partial x}\right),$$

where $c_{ij} = k_y^{\ 2} - \omega^2\mu_i\varepsilon_j$. While the left-hand-sides of equation (13)-(14) are identical to the governing equations presented in Mitsuhata (2000) , the right-hand-sides are expressed by $\widetilde{E}_{py}$ and $\widetilde{H}_{py}$ instead of $\widetilde{E}_{px}$, $\widetilde{E}_{py}$ and $\widetilde{E}_{pz}$. However, a simple arithmetic reformulation of the right-hand-side of equation (13) using equations (9)-(12) can show that both forms are equivalent (not shown). Having the same field components and derivatives on on both sides of the equations, allows us to speed-up the assembling of the linear equation system.

With the governing equations defined in equation (9)-(14), we use the standard finite element approach to define a set of local equations for each element. By combining all these using the Galerkin method (Zienkiewicz, Taylor, and Taylor 1977) with 2nd order nodal elements and Dirichlet boundary conditions, a global set of linear equations is found for the secondary electromagnetic fields (See appendix A for more details). From equation (13)-(14) a linear system of equations is found:

$$\boldsymbol{A}\widetilde{\boldsymbol{x}} = \boldsymbol{b}, \tag{15}$$

where $\boldsymbol{A}$ is the global symmetric stiffness matrix, $\tilde{\boldsymbol{x}}$ contains the Fourier transformed secondary EM-fields, and $\boldsymbol{b}$ contains the source terms, where each column represents one source component.

The procedure to solve the system is as follows: assemble the matrix equation resulting from equation (15), solve the linear system using a direct LU-decomposition solver and interpolate the field values at the receiver positions using the same 2nd order shape function (which has already been used to assemble the finite element system) to find the Fourier transformed y-components of the secondary fields. Then insert the solution into equation (9)-(12) to find the remaining components of the Fourier transformed fields. Finally, the inverse Fourier transform is applied in order to obtain the fields in the frequency-domain. This inverse Fourier transform is done numerically by logarithmic spaced k_y-samples, which are splined together over the relevant k_y-domain. Tests show that five wavenumbers per decade between $10^{-5} - 10\ \mathrm{m}^{-1}$ provide sufficiently accurate results. One important point related to the inverse Fourier transform is that the air conductivity needs to be larger than zero, otherwise a singularity at $k_y^2 \approx \omega^2 \mu \varepsilon$ is encountered (Mitsuhata 2000). We found that setting the air conductivity to $\sigma = 10^{-6}\ \mathrm{S/m}$ keeps the air sufficiently resistive, while avoiding the singularity within a frequency range of 0.4-130 kHz.

Derivative calculation

The 2D derivatives are found through the adjoint-state method, while the 1D derivatives for the hybrid inversion scheme are found by successive forward calculations using small perturbations of the model parameters (Auken et al. 2014). For the 2D calculations, equation (15) is differentiated with regards to the model parameters $\boldsymbol{m}$:

$$\frac{d(\boldsymbol{A}\tilde{\boldsymbol{x}})}{d\boldsymbol{m}} = \frac{d\boldsymbol{b}}{d\boldsymbol{m}} \tag{16}$$

which through the product rule gives the Jacobi elements:

$$\frac{d\tilde{\boldsymbol{x}}}{d\boldsymbol{m}} = \boldsymbol{A}^{-1}\left(\frac{d\boldsymbol{b}}{d\boldsymbol{m}} - \frac{d\boldsymbol{A}}{d\boldsymbol{m}}\tilde{\boldsymbol{x}}\right) \tag{17}$$

Here, m can be chosen to represent the resistivity or the logarithm of the resistivity. Since only the coefficients of the governing equations are depending on the conductivity, $\frac{d\boldsymbol{A}}{d\boldsymbol{m}}$ and $\frac{d\boldsymbol{b}}{d\boldsymbol{m}}$ can be analytically calculated and assembled. As each inversion cell usually contains only a small number of finite elements, both of these terms are extremely sparse and $\frac{d\boldsymbol{b}}{d\boldsymbol{m}} - \frac{d\boldsymbol{A}}{d\boldsymbol{m}}\tilde{\boldsymbol{x}}$ can be calculated efficiently, and the result can still be considered sparse. To calculate $\boldsymbol{A}^{-1}$, however, would be far too expensive. Instead, we use the fact that only the field derivatives at the receiver position are of interest, and thus only columns of $\boldsymbol{A}^{-1}$ corresponding to the receiver positions need to be calculated. This is done using the same direct LU-decomposition solver as for the regular forward solutions. The matrix multiplication in equation (17) then results in $\frac{d\tilde{\boldsymbol{x}}}{d\boldsymbol{m}}$, which is a dense matrix, however, with rather small dimensions, where the number of rows is equal to the number of sources, and the number of columns is equal to 12 times the number of receivers (6 nodes per finite element with 2 field components each). The derivatives at the receiver positions are then calculated from $\frac{d\tilde{\boldsymbol{x}}}{d\boldsymbol{m}}$ using the second order shape function as interpolator. For derivatives with respect to resistivity, the result of $\frac{d\tilde{\boldsymbol{x}}}{d\boldsymbol{m}}$ builds the coefficients in the Jacobian Matrix $\boldsymbol{G}$ for the respective inversion parameter. As altitude derivatives cannot be calculated by this approach, those derivatives are calculated by small perturbations, as done in the 1D case.

Meshing

The 2D modelling is performed on a triangular finite element mesh as shown in Figure 1 (b), while the inversion operates on a regular grid, as seen in Figure 1 (a). The column spacing of the inversion grid is determined by the sounding distance, the row spacing by the model layers, and the layer thickness is chosen to be logarithmically increasing, which reflects the decreasing sensitivity of HEM systems with

depth. Separating the meshes of forward calculations and inversion has some clear computational benefits, as the inversion grid is much coarser than the 2D forward mesh. This decreases the size of the inversion problem, while maintaining the accuracy of the forward modelling.

Interpolation between the inversion grid and the forward mesh is avoided by using the inversion grid as a skeletal structure for the forward mesh (Figure 1). By incorporating the inversion grid into the forward mesh, it is guaranteed that each finite element is fully residing in just one inversion cell, which makes the forward modelling mesh an exact representation of the inversion grid.

The mesh density for the forward mesh is adjusted according to the key parameters like frequency and source/receiver height. The highest mesh density is needed near the surface below the sources, where the primary field is strongest. Here, the mesh density is selected as a function of the source height and, thus, of the strength of the primary field. Tests showed, that at deeper locations and at larger horizontal offsets from the source, the mesh density can be reduced without losing accuracy. The higher the frequency, the quicker the mesh may coarsen. Tests showed that reducing the mesh density for increasing offset and depth as a function of the logarithm of the frequency gives good tradeoff of accuracy and mesh size. Additionally, the mesh density is increased near the receivers, in order to calculate the spatial derivatives in equations (11) and (12) accurately.

The mesh of the 2D forward model is appended with large absorbing boundary domains that extend 10km in each direction. As the mesh density is coarsening quickly in these boundary domains, the computational overhead is not very high, but the size of the domains allows the field to attenuate, so that the validity of the Dirichlet boundary conditions is assured.

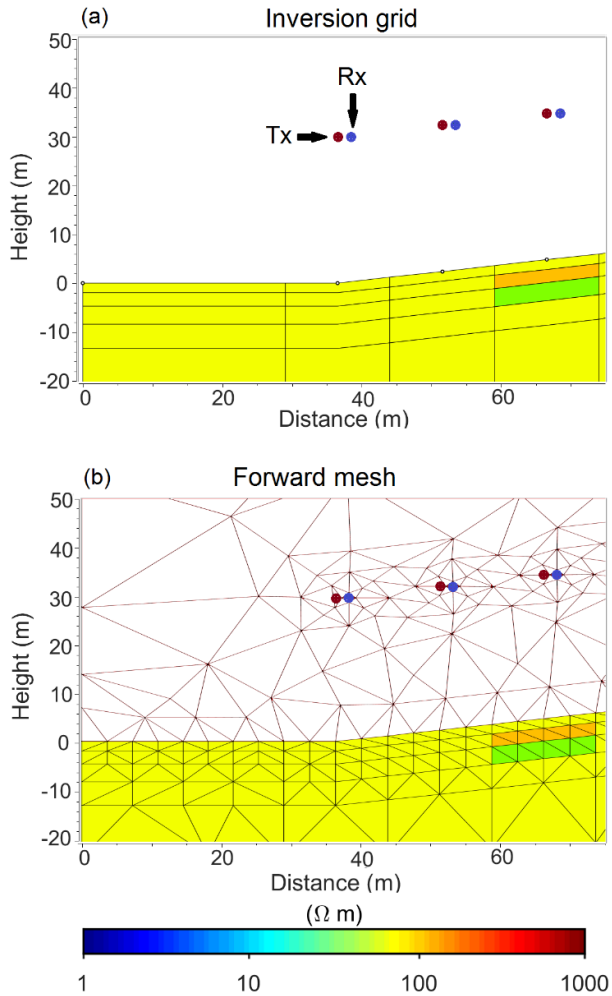

Figure 1 Inversion grid and forward mesh for a small section of a HEM survey.

Transmitters are indicated by a brown circle, receivers by a blue circle. (a) Shows the inversion grid. In the inversion grid, the column width is determined by the sounding distance, while the column depth is reflecting the thickness of the model layers. (b) Shows the resulting forward modelling finite element mesh. Note how the inversion grid is still present in the forward modelling mesh, since this is used as the skeletal structure for building the finite element mesh.

Sectioning

Even for relatively small surveys, it is computationally inefficient to create and store a sufficiently fine finite element mesh and do 2D calculations on all soundings at once. Because of this, it is imperative to split large surveys into smaller sections. Sectioning, or local meshing as it is also often called in the literature, can be accomplished in several different ways. Our sectioning method is somewhat similar to the method used in Yang and Oldenburg (2012a). Their method involves a global mesh, and a local mesh for each sounding. While the forward problem is handled on the local meshes, the inversion is made by subsampling the global mesh. In our case the local meshes contain multiple soundings, since that is more efficient, and is used for both the 2D forward and derivative calculations. In order for these sections to retain the 2D information of the survey, they need to overlap as shown in Figure 2. Thus, each section, L, consists of a core section, l, and one or two overlapping regions, Δl. Continuity between different sections are ensured by using sufficient overlap between different sections, and by placing lateral constraints on all soundings irregardless of section boundaries. The size of the overlap and sections will be addressed later.

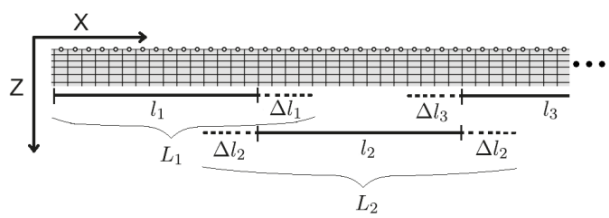

Figure 2 Sectioning of survey lines. Each section, L, consists of a core section, l, and overlap regions, Δl . Sections at the end of a survey line only have one overlap region, while all other sections have two overlap regions. The dots on top of the ground surface indicate the individual soundings.

Forward modelling validation

The 2D finite element forward response was validated against the 1D code of Auken et al. (2014) for a range of frequencies relevant for HEM (0.4-130 kHz) across different half spaces with

resistivities of: 10 Ωm, 100 Ωm, and 1000 Ωm. A halfspace comparison between 1D and 2D is shown in Figure 3. The mesh density is selected such that the resulting responses deviate less than 5 % from the 1D responses within the frequency range. The inaccuracy of the 1D response is estimated to be between 0.1–0.3 % and is insignificant in this context. Note that the deviation between 1D and 2D responses is not just a single number, but instead a range, because of variations in the mesh density between soundings near the edge of the mesh and those near the center. This is reflected in Figure 3 (b), where the deviation from 1D is shown for a 300 m long section with 30 soundings equally spaced over the section. The flight height of the system is 30 m and the halfspace resistivity is set to 100 Ωm. Similar accuracies are obtained from halfspace resistivities at 10 Ωm and 1000 Ωm, but for brevity we only show one representative example. In this case, the inaccuracy is generally less than 2%, while reaching as high as 5% for frequencies beyond the range shown here.

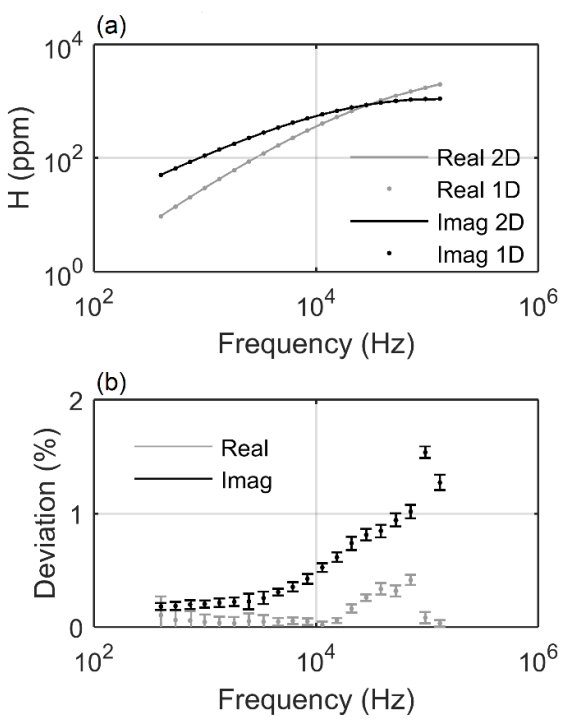

Figure 3 1D and 2D forward responses and deviations, on a 100 Ωm halfspace at an instrument altitude of 30 m, as a function of frequency (a) Shows an example of a 1D and 2D

forward response for just a single sounding. (b) Shows the relative deviations between 2D and 1D forward response. The deviation is expressed as a range, because the accuracy of the 2D responses varies between soundings near the edge and near the center due to mesh variations. The 2D responses are from a 300 m section with 30 equally spaced soundings. Deviations at all frequencies and all positions are below 2%.

Inversion algorithm

Our inversion technique utilizes linearized minimization, following the Levenberg-Marquardt adaptive scheme (Menke 1989). The following is a brief review of our inversion algorithm, see Auken and Christiansen (2004), (Auken et al. 2014) for the full details.

The minimized objective function is given as:

$$q = q_{obs} + q_{prior} + q_{reg} \tag{18}$$

with q_{obs} being the observed data misfit, q_{prior} being the prior constraint misfit, and q_{reg} being the regularization misfit. Smooth regularizations are used both laterally and vertically. To determine the misfit, we use a standard least-square solution (L2-norm). With this, the n'th iterative update of the model vector $\boldsymbol{m}$ is given as:

$$\boldsymbol{m}_{n+1} = \boldsymbol{m}_n + \left(\widehat{\boldsymbol{G}}_n^T \boldsymbol{C}_n^{-1} \widehat{\boldsymbol{G}}_n + \lambda_n \boldsymbol{I}\right)^{-1} \cdot \left(\widehat{\boldsymbol{G}}_n^T \boldsymbol{C}_n^{-1} \delta\widehat{\boldsymbol{d}}_n\right) \tag{19}$$

where λ is the damping parameter (Marquardt 1963), $\delta\widehat{\boldsymbol{d}}$ is the extended perturbed data vector, $\widehat{\boldsymbol{G}}$ is the extended Jacobian, and $\widehat{\boldsymbol{C}}$ is the extended covariance matrix, where the extensions comes from the inclusion of prior information and regularization:

$$\delta\widehat{\boldsymbol{d}} = \begin{bmatrix} \boldsymbol{d} - \boldsymbol{d}_{obs} \\ \boldsymbol{m} - \boldsymbol{m}_{prior} \\ -\boldsymbol{R}\boldsymbol{m} \end{bmatrix} \tag{20}$$

$$\widehat{\boldsymbol{G}} = \begin{bmatrix} \boldsymbol{G} \\ \boldsymbol{P} \\ \boldsymbol{R} \end{bmatrix} \tag{21}$$

$$\widehat{\boldsymbol{C}} = \begin{bmatrix} \boldsymbol{C}_{obs} & 0 & 0 \\ 0 & \boldsymbol{C}_{prior} & 0 \\ 0 & 0 & \boldsymbol{C}_{reg} \end{bmatrix} \tag{22}$$

where, $\boldsymbol{d}$ is the forward response, $\boldsymbol{d}_{obs}$ is the observed data, $\boldsymbol{m}$ is the model parameters, $\boldsymbol{m}_{prior}$ is the a priori model parameters, $\boldsymbol{R}$ is the roughness matrix, which binds neighboring models/model-parameters together, $\boldsymbol{G}$ is the Jacobian , $\boldsymbol{P}$ is a matrix containing the a priori information, $\boldsymbol{C}_{obs}$ is the covariance of the observed data, $\boldsymbol{C}_{prior}$ is the covariance of the a priori information, and $\boldsymbol{C}_{reg}$ is the covariance stemming from the roughness matrix.

Calculating the iterative model update as shown in equation (19), requires solving a large linear system. In 1D, this system is sparse, but in 2D the linear system is in principle dense. However, in practice it can be assumed sparse if only the part with most sensitivity is considered (this will be covered in more detail later). Nevertheless, the 2D linear system will always be considerably less sparse than the 1D case. Solving large sparse linear systems is non-trivial and the optimal approach is dependent on the system being solved. Our current approach to solving the linear system in the 1D case is thoroughly described in Kirkegaard and Auken (2015), and starts with a reverse Cuthill-Mckee reordering algorithm (Cuthill and McKee 1969), which is used on the ordering of the initial soundings. This results in the matrix being created in such a way that all vital non-zero elements lie relatively close to the diagonal, while retaining the sounding structure in the matrix. The actual matrix is solved in parallel using an iterative sparse solver, which uses CG propagation (Hestenes and Stiefel 1952, Saad 2003), along with a preconditioner, which depends on the dimensionality of the inversion problem. For the 1D inversion problem our method of choice is a block-parallelized version of an incomplete LU factorization with a dual dropping strategy (Saad 1994). However, due to the increased bandwidth of the sparse matrix in the 2D case, consistent convergence is not obtained when applying the LU decomposition as a preconditioner. Direct solvers work

well for small surveys (up to around 5,000 soundings), but for larger surveys direct solvers become inefficient due to memory consumption as well as factorization time. Neither scale linearly with the size of the survey. Instead, we have found that applying the symmetric-Gauss-Seidel (SGS) preconditioner leads to stable convergence when doing 2D inversions. Furthermore, if applied in cases where the linear system is sufficiently diagonally dominant, the SGS preconditioner is even more efficient than the incomplete LU factorization, and can lead to a significant speedup in 1D inversions.

Optimizing section sizes

Previously, we discussed the need for dividing large surveys into smaller sections due to memory concerns. However, even if memory had not been an issue it still proves computationally advantageous to split a survey into smaller sections. The reason for this is that for unstructured meshes, the computational time scales quadratically with the number of elements as the number of elements becomes large. On the other hand, there is also a size-independent initialization cost associated with each section that needs to be considered. This cost comes from setting up the mesh padding, establishing the equations, spawning the parallel thread pool, and other similar tasks. Even more importantly, it also needs to be assured that each section overlaps its neighboring section by a fixed amount, in order to retain the 2D information from the survey.

Analysis of our parallel algorithm has led to the identification of an optimal section size. One that is defined by the initial computational cost, the quadratic computational scaling with section size, as well as the overlap size. In order to find this optimal section size, performance tests for the RESOLVE system (shown in Table 1) were conducted. The experiments were performed over a sweep of section sizes, and the results for both forward and derivative computations can be seen in Figure 4 (a).

Coil #	Orientation	Frequency (kHz)	Separation (m)
1	Z	0.395	7.9
2	Z	1.822	7.9
3	X	5.4	9.06

4	Z	8.199	7.9
5	Z	38.76	7.9
6	Z	128.76	7.9

Table 1 The table lists the parameters for the modelled system, which resembles a RESOLVE system. The flight altitude is 30 m and the uncertainty on the data is 5%.

As seen in Figure 4 (a), the computational times present a global minimum, different for forward and derivative calculations. The reason why the derivative calculation favors smaller section sizes than the forward calculation is due to the heavier computational burden associated with derivative calculations. This increased computational burden makes the initialization cost less significant and thus naturally shifts the optimal section size for derivative calculation towards smaller sizes. With the results presented in Figure 4 (a), the optimal section size as a function of the overlap is determined as shown in Figure 4 (b). The optimal section size is determined by using the data in Figure 4 (a). By subtracting two times the desired overlap size from the section sizes given in Figure 4 (a), and interpolating the remaining positive section sizes, an estimate of the computational time for a given section size with a given overlap size can be determined. In order to find the optimal section size, the section sizes that fall within 5 % of the fastest time for a given overlap are used and shown in Figure 4 (b). Note that, once again, the optimal section sizes are different for forward and derivative calculations. One caveat to this is that the results in Figure 4 (b) change depending on the 2D finite element mesh density, which changes slightly between different surveys and systems. Therefore, Figure 4 (b) should not be considered the absolute truth, but rather serve as a guide for picking a sensible section size based on overlap size.

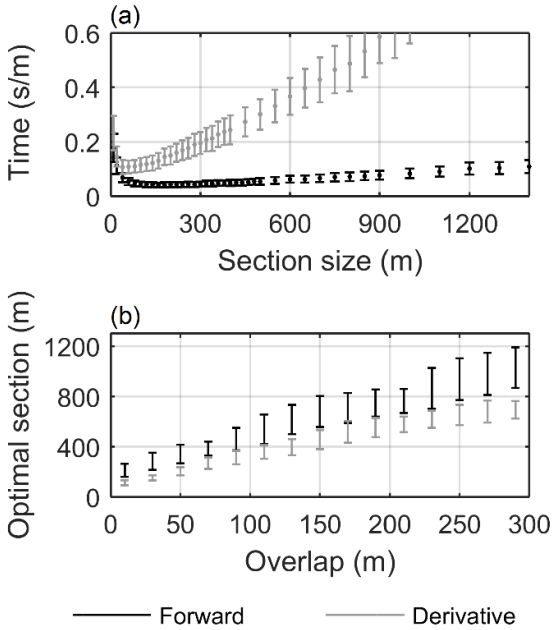

Figure 4 (a) Time required for an iteration of forward and derivative calculations for the RESOLVE system presented in Table 1 using a 10 m sounding separation, as a function of section size. For small section sizes the initialization cost becomes dominant and visible as a sharp increase in iteration time per m, while for large section sizes the quadratic scaling of the finite elements becomes dominant, and is visible as a linear rise in iteration time per meter (it appears linear in the figure, because iteration time per meter is shown). The range bars indicate variance in computational time between various repetitions, and indicate 1 standard deviation. (b) Shows optimal section sizes as a function of the overlap, where the range bars represent section sizes that are within 5% of the optimal compute time.

2D Jacobian and sensitivity analysis

As mentioned earlier, the structure of the 2D Jacobian is a dense matrix. However, due to the decay in sensitivity as a function of distance, a threshold can be defined, where anything that falls below this threshold is assumed negligible. Thus, in practice the Jacobian matrix can still be considered

sparse even in 2D, even though it has considerably wider bands around the diagonal than in the 1D case. The 2D Jacobian matrix resulting from the inversion grid is illustrated in Figure 5. (a) Shows the 2D Jacobian in block form. Note that the 1D Jacobian structure is identical to the one for the 2D Jacobian, but in the 1D case all the off-diagonal elements shown in Figure 5 (a) would be zero. Figure 5 (b) shows the structure of a single Jacobian block element, which contains a number of elements equal to the number of perturbable model parameters for this particular model (altitude, and resistivities) times the number of data points for the corresponding sounding.

(a) 2D Jacobian

$$\boldsymbol{G} = \begin{pmatrix} \ddots & \vdots & \vdots & \vdots & \vdots & \vdots & \iddots \\ \cdots & \frac{\partial \boldsymbol{D}_{i-2}}{\partial \boldsymbol{M}_{i-2}} & \frac{\partial \boldsymbol{D}_{i-2}}{\partial \boldsymbol{M}_{i-1}} & 0 & 0 & 0 & \cdots \\ \cdots & \frac{\partial \boldsymbol{D}_{i-1}}{\partial \boldsymbol{M}_{i-2}} & \frac{\partial \boldsymbol{D}_{i-1}}{\partial \boldsymbol{M}_{i-1}} & \frac{\partial \boldsymbol{D}_{i-1}}{\partial \boldsymbol{M}_{i}} & 0 & 0 & \cdots \\ \cdots & 0 & \frac{\partial \boldsymbol{D}_{i}}{\partial \boldsymbol{M}_{i-1}} & \frac{\partial \boldsymbol{D}_{i}}{\partial \boldsymbol{M}_{i}} & \frac{\partial \boldsymbol{D}_{i}}{\partial \boldsymbol{M}_{i+1}} & 0 & \cdots \\ \cdots & 0 & 0 & \frac{\partial \boldsymbol{D}_{i+1}}{\partial \boldsymbol{M}_{i}} & \frac{\partial \boldsymbol{D}_{i+1}}{\partial \boldsymbol{M}_{i+1}} & \frac{\partial \boldsymbol{D}_{i+1}}{\partial \boldsymbol{M}_{i+2}} & \cdots \\ \cdots & 0 & 0 & 0 & \frac{\partial \boldsymbol{D}_{i+2}}{\partial \boldsymbol{M}_{i+1}} & \frac{\partial \boldsymbol{D}_{i+2}}{\partial \boldsymbol{M}_{i+2}} & \cdots \\ \iddots & \vdots & \vdots & \vdots & \vdots & \vdots & \ddots \end{pmatrix}$$

(b) Jacobian block element

$$\frac{\partial \boldsymbol{D}_j}{\partial \boldsymbol{M}_k} = \begin{pmatrix} \frac{\partial d_{j,1}}{\partial m_{k,1}} & \frac{\partial d_{j,1}}{\partial m_{k,2}} & \frac{\partial d_{j,1}}{\partial m_{k,3}} & \cdot & \frac{\partial d_{j,1}}{\partial m_{k,N_{m_k}}} \\ \frac{\partial d_{j,2}}{\partial m_{k,1}} & \frac{\partial d_{j,2}}{\partial m_{k,2}} & \frac{\partial d_{j,2}}{\partial m_{k,3}} & \cdot & \frac{\partial d_{j,2}}{\partial m_{k,N_{m_k}}} \\ \frac{\partial d_{j,3}}{\partial m_{k,1}} & \frac{\partial d_{j,3}}{\partial m_{k,2}} & \frac{\partial d_{j,3}}{\partial m_{k,3}} & \cdot & \frac{\partial d_{j,3}}{\partial m_{k,N_{m_k}}} \\ \vdots & \vdots & \vdots & \vdots & \vdots \\ \frac{\partial d_{j,N_{d_j}}}{\partial m_{k,1}} & \frac{\partial d_{j,N_{d_j}}}{\partial m_{k,2}} & \frac{\partial d_{j,N_{d_j}}}{\partial m_{k,3}} & \cdot & \frac{\partial d_{j,N_{d_j}}}{\partial m_{k,N_{m_k}}} \end{pmatrix}$$

Figure 5 Structure of our 2D Jacobian. (a) Shows the 2D Jacobian in block-matrix form, where the number of off-diagonal bands is equal to the number of surrounding soundings above the sensitivity threshold (in this illustration, only the nearest neighbor is above the threshold). Each entry in the Jacobian block matrix is a dense matrix block. (b) Shows the structure of a single Jacobian block element. j and k represent the individual sounding indices, and $\boldsymbol{D}_j$ contains $N_{d\,j}$ forward responses associated with the j'th sounding. While

$\boldsymbol{M}_k$ contains N_{m_k} model parameters associated with sounding k.

Accurately determining the resulting sensitivity range is important, not just when building the Jacobian, but also when optimizing section size. This is due to the obvious connection between the sensitivity threshold distance, and the required overlap distance between adjacent sections. To determine the sensitivity threshold, we follow the convention of Liu and Becker (1990) and define a significant sensitivity range as the distance at which 90% of the full sensitivity is contained. Following this approach, a sensitivity analysis was performed for the coils shown in Table 1, for altitudes ranging between 20-50m. Figure 6 (a) demonstrates the cumulated sensitivity as a function of distance for a 0.4 kHz signal originating at an altitude of 30 m, while Figure 6 (b,c) shows the correlation between depth and footprint size for a 0.4 kHz signal and a 1.8 kHz signal. Based on the sensitivity analysis as well as performance concerns, we decide to use an overlap of 150 m. While this is less than the footprint size for the real part of the 0.4 kHz signal, more than 75 % of the sensitivity for a 100 Ωm halfspace is retained, and if considering total sensitivity over all frequencies then the total loss of sensitivity is around 7 %, which we deem an acceptable loss.

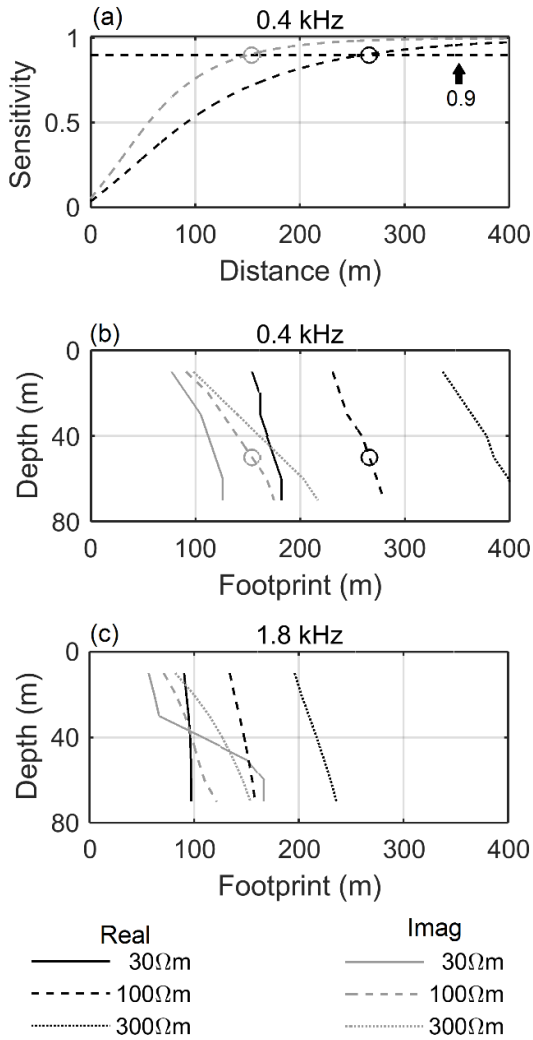

Figure 6 Sensitivity analysis for a frequency domain system at an altitude of 30 m. (a) Cumulated sensitivity as a function of distance for a 0.4 kHz signal, on a 100 Ωm halfspace at a depth of 50-60 m, with the horizontal dashed line indicating the footprint size at 90% threshold. The two circles indicate the distances where the 0.4 kHz signal reaches the threshold for the real and imaginary response. (b,c) Correlation between footprint size and depth for a 0.4 kHz signal and a 1.8 kHz signal, on a 30 Ωm, 100 Ωm, and 300 Ωm halfspace. On (b) the two circles from (a) are also plotted.

1D/2D Hybrid inversion scheme

The conceptual idea behind the hybrid inversion scheme is to use computationally inexpensive approximative forward and derivative computations in the first inversion steps where accuracy is of little importance. As the iterations start to converge, one can then gradually switch to higher accuracy computations that are more expensive. Within such a scheme, the overall computational time can be greatly reduced without sacrificing the quality of the final model. Such a scheme can be constructed in several ways; Christiansen et al. (2015) have created a hybrid scheme using increasingly accurate 1D modelling responses, and a similar approach could be envisioned in 2D by using a coarse mesh in the early iterations and a more refined mesh in the later stages. However, we believe that our hybrid scheme would be computationally superior to such a scheme, since 1D modelling is so computationally inexpensive compared to 2D modelling, and the number of full 2D iterations utilized in our scheme is quite low as will be demonstrated later. Our hybrid scheme is a 3-stage scheme with:

1. 1D forward and derivative calculations
2. 2D forward, 1D derivative calculations
3. 2D forward and 2D derivative calculations

Each stage is executed with a fixed number of iterations. By running the hybrid scheme over a large number of synthetic models, we have empirically found that the optimal number of iterations are four in the first stage, and eight in the second stage. The third stage runs until the algorithm converges.

The inversion is said to have converged if the relative misfit change is less than 1% between two iteration steps. If convergence is reached in stage 1 or 2, then the inversion is advanced to the next stage and the process continues.

RESULTS AND DISCUSSION

Synthetic model

The 2D hybrid inversion algorithm is demonstrated on two synthetic models. A system resembling the RESOLVE system with the parameters shown in Table 1 is modelled. In both examples, the inversion is started from a 100 Ωm halfspace with a model discretization of 20 layers where the thickness of each layer increases logarithmically from 3 m – 10 m. Horizontal smoothing constraints are employed with a covariance factor of 1.6 and vertical smoothing with a factor of 3.0. There are 51 equidistant soundings distributed over a 500 m long line.

Figure 7 shows the results of an inversion of a conductive lens. (a) Illustrates the true model, which consists of a 50 Ωm lens in a 500 Ωm halfspace, (b) shows a 1D inversion, (c) shows a hybrid inversion, and (d) shows a full 2D inversion. The 1D inversion mostly manages to recover the conductive lens at the correct depth, but strong pant legs are produced. The 1D inversion is shown with both a 1D and 2D residual curve. Both residual curves use the model arrived at through the 1D inversion, but the 1D residual evaluates the 1D forward responses, while the 2D residual is relative to 2D forward responses. Variation between the two residuals can therefore be regarded as an indicator of areas where 1D modeling is insufficient. Both the hybrid and the full 2D inversion reproduce the lens as good as can be expected from an AEM measurement, without any pant legs effect and with a good determination of the lens boundaries, and a misfit well below 1, which in our synthetic model without noise is a good thing. The speedup gained by utilizing the hybrid inversion was 2.7x compared to the 2D inversion, and will be discussed in detail in the Performance subsection.

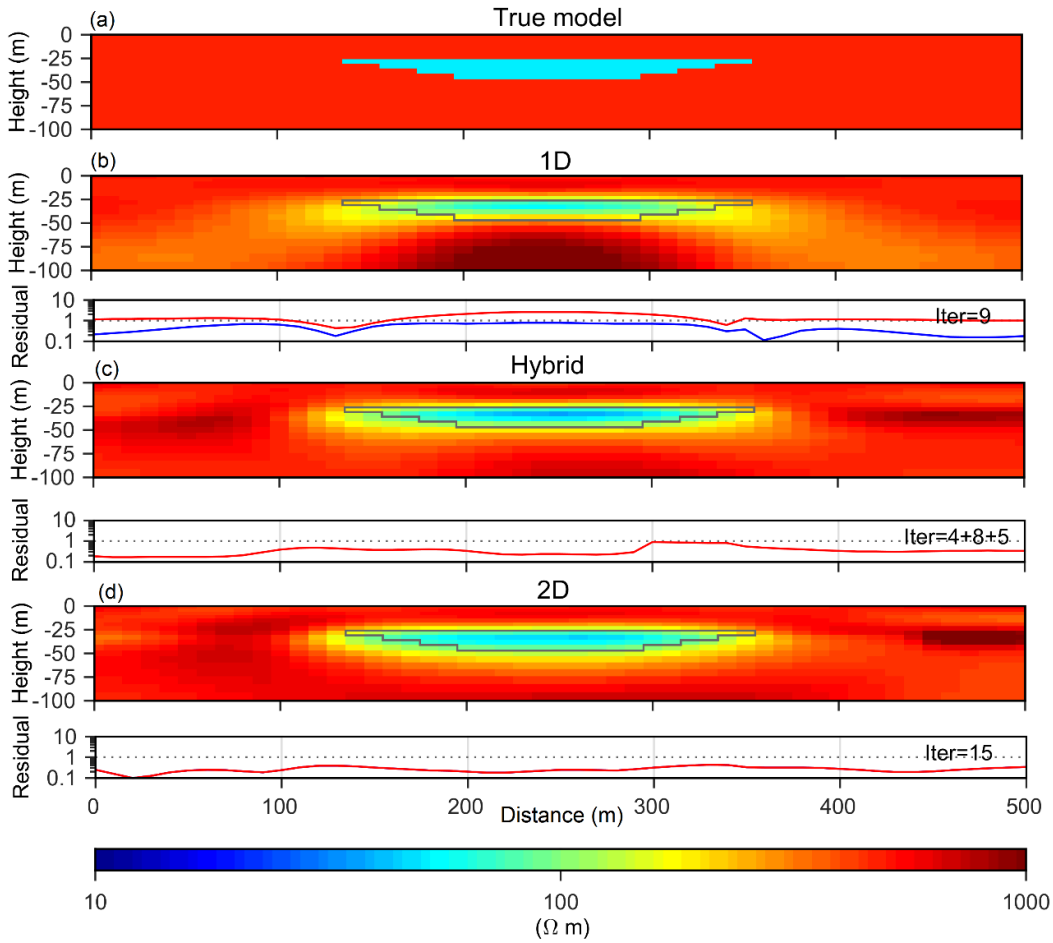

Figure 7 Inversion results for a synthetic conductive lens. (a) True model, which consists of a 50 Ωm lens in a 500 Ωm halfspace. (b) 1D inversion, where the blue line is the 1D data residual, and the red line is the 2D data residual. (c) Hybrid inversion, where the number of iterations are given in each hybrid stage separately. (d) 2D inversion. For all inversions, the number of iterations until convergence is written inside the residual box.

Figure 8 shows the results of an inversion of a sharp horizontal conductivity contrast. (a) Illustrates the true model, where the left side is 10 Ωm and the right side is 200 Ωm, (b) shows a 1D inversion, (c) shows a hybrid inversion, and (d) shows a full 2D inversion. In this case, the 1D inversion creates a rather wide region around the conductivity contrast where the conductivities are smeared and

there are clearly visible pant legs. Once again, both 1D and 2D residuals are shown. The full 2D inversion demonstrates a better determination of the vertical boundary and while smearing is still observed, the affected region is significantly smaller. The hybrid model again converges to a model, which is significantly better than the 1D model, as noticed both by the size of the smearing region as well as the residual, which is only slightly higher than for the 2D inversions. The differences between the 2D and the hybrid model are likely a result of the 1D model doing a poor job of accurately modelling the sharp conductivity contrast, combined with model equivalences, as evidenced the similarity of the hybrid/2D residual. The speedup gained by utilizing the hybrid inversion was 6.6x compared to the 2D inversion, and will be discussed in detail in the Performance subsection.

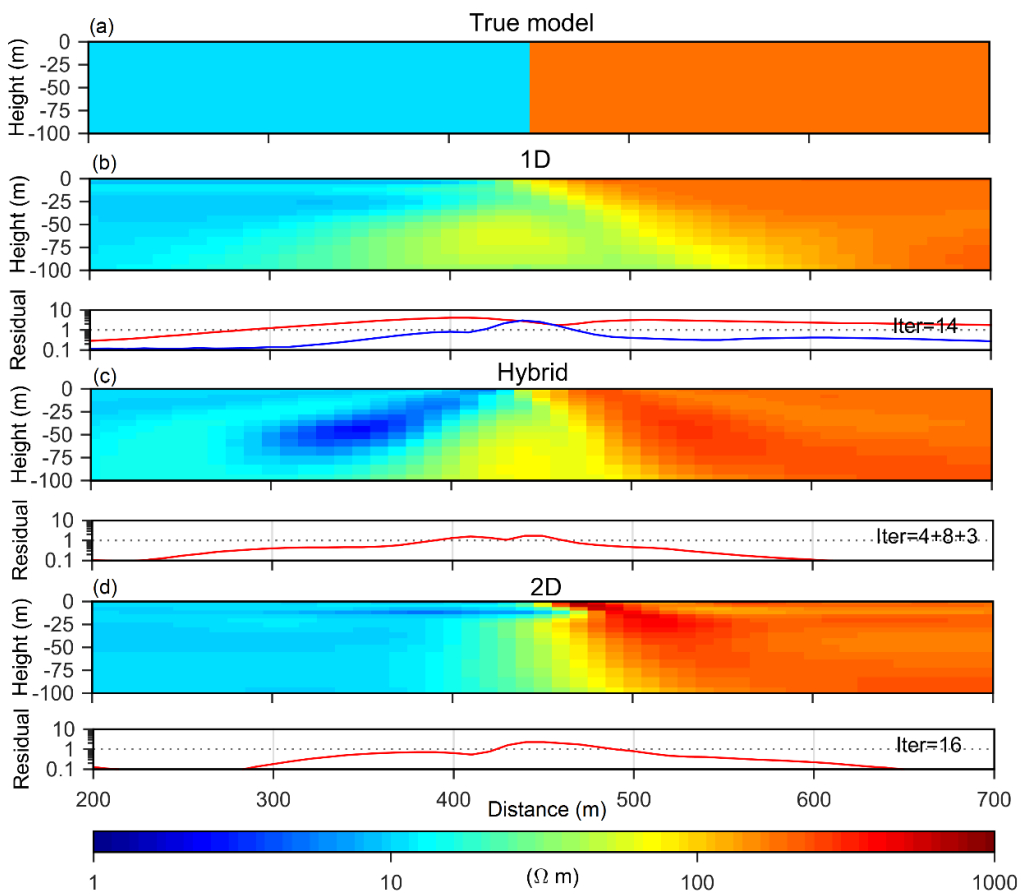

Figure 8 Inversion results for a horizontal conductivity contrast. (a) Illustrates the true

model; the left side has a resistivity of 10 Ωm, while the right side has a resistivity of 200 Ωm. (b) Shows the result from a 1D inversion, where the blue line is the 1D data residual, and the red line is the 2D data residual. (c) Shows the result from a hybrid inversion. (d) Shows the result from a 2D inversion. The number of iterations until convergence is written inside the residual box.

Field example

As a final test, the 2D algorithm is used on a field example collected by a RESOLVE system owned by the German Bundesanstalt für Geowissenschaften und Rohstoffe (BGR). The field data was collected on a small island named Langeoog, where the target is a mapping of the freshwater/saltwater boundary (Siemon et al. 2015). Langeoog comprises three geological features: the base is formed from glaciofluvial sediments, from the Pleistocene age. This contains Lauenburg clay, which lies at a depth of 15-35 m below sea level, with a typical thickness of a few meters. Overlaying the Pleistocene layer is a Holocene marine deposit, which lies at 10-20 m depth below sea level. The top-layer consist of dunes and beach sand. For more information about the geology of Langeoog, see Costabel et al. (2017).

The field data profile is 1400 m long and consists of 144 soundings. Inversion results are shown in Figure 9. (a) Shows a 1D inversion, (b) shows a hybrid inversion, while (c) shows a 2D inversion. Overall, the three different inversions show very consistent results, though there are notable differences in the top layers at around the 1 km mark. While the models deviate at this point, the data residual for the 2D and hybrid code are only negligibly lower than for the 1D inversion. Upon a closer look at the fit of each individual transmitter frequency, it is revealed that there is excellent correspondence between measured data and modelled response for all coils except coil 3. This coil is off by several standard deviations in the high residual area around the 1 km mark. Figure 10 shows an example of this for sounding 112, which is

marked in Figure 9 by a vertical red line. The speedup gained by utilizing the hybrid inversion was 6x compared to the 2D inversion, and will be discussed in detail in the Performance subsection.

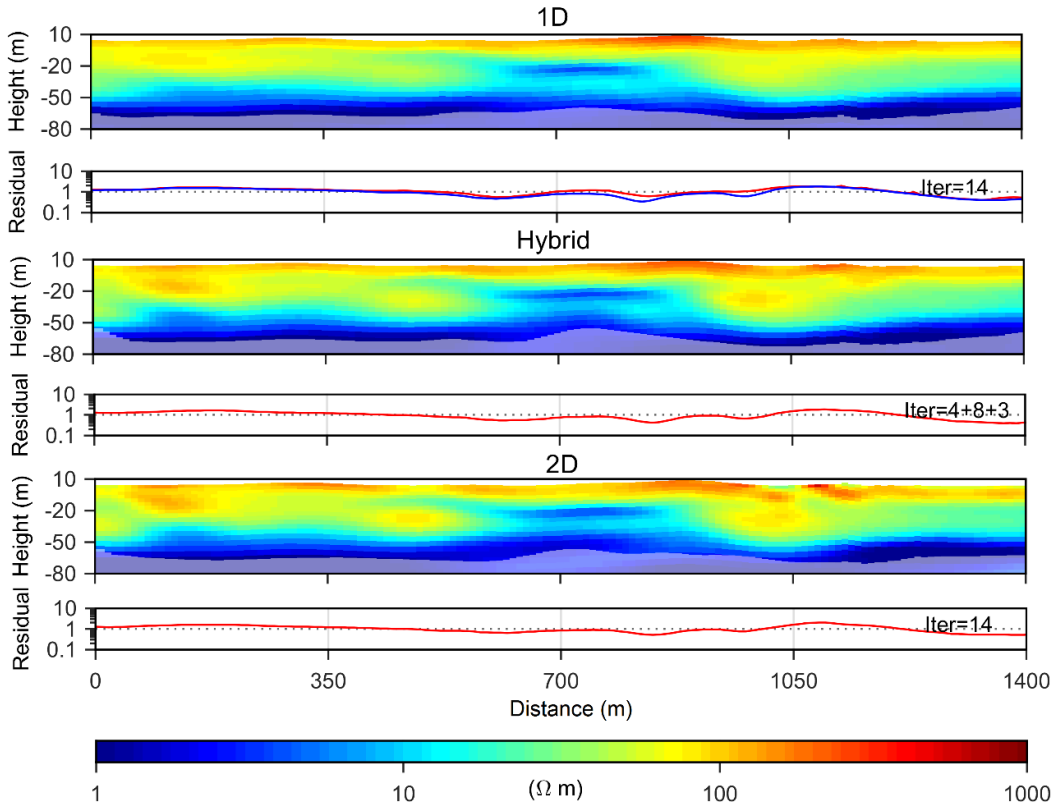

Figure 9 Inversion results from a survey in northern Germany (Siemon et al. 2015). (a) Shows a 1D inversion, where the blue line is the 1D data residual, and the red line is the 2D data residual. (b) Shows a hybrid inversion, where the number of iterations are provided for each separate stage. (c) Shows a 2D inversion. The number of iterations until convergence is written inside the residual box. The vertical red line at the top of the figures around 1100 is sounding 112, which is shown in Figure 10.

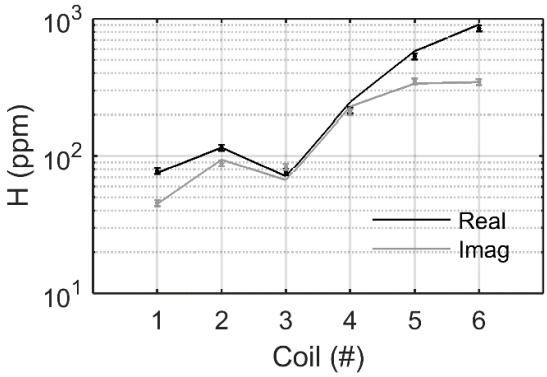

Figure 10 Example of a 2D sounding curve for the inversion results shown in Figure 9 (c). The sounding curve is marked in Figure 9 by a vertical red line at the top of the figures, around 1.1 km distance. The coil # configuration can be found in Table 1.

Parallelization and scalability

Since the introduction of commodity multicore CPUs in 2005, parallelization has become increasingly important. While computational speed continues to grow exponentially, it has become a non-trivial issue to fully harness this power. Algorithms often have to be specifically tailored to enable optimal parallelization, and with the shift away from uniform memory access (UMA) systems, and towards non-uniform memory access (NUMA) systems architecture, this becomes an even harder problem. The architectures are illustrated in Figure 11. The consequences of having a NUMA system is that data placement becomes paramount. If data is not placed in the local memory associated with the processor working on it, it will need to be accessed over the interconnect by the processor. Not only does this add significant latency, but the interconnect also has limited bandwidth and becomes saturated much before the direct channels to local memory. For this reason, good scaling on the NUMA system is harder to achieve in general than on uniform memory access (UMA) systems, and if not done carefully can actually lead to decreased performance, unlike for UMA systems (Panourgias 2011).

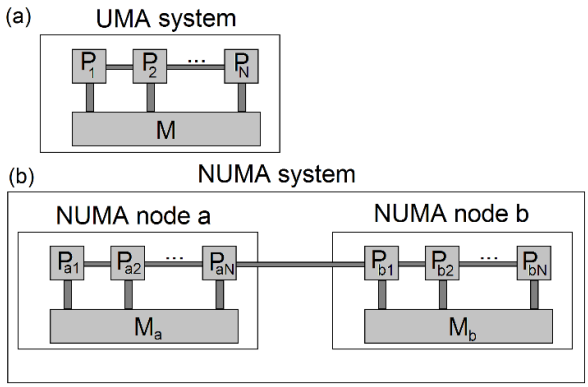

Figure 11 UMA and NUMA system architectures. P represents processors, while M represents memory. (a) an UMA system; here there is only one memory bank, and all the processors have the same bandwidth connection to the memory. (b) a two-node NUMA system, which essentially consists of two connected UMA systems. Thus, each NUMA node has a number of processors attached to a memory bank, and the different memory banks are then connected together by a relatively small bandwidth.

The 2D FEM problem can be parallelized in several ways, but to get the best possible scalability for large surveys, we chose to put our parallelization across the sections. In other words, multiple sections are computed in parallel. This requires more memory than putting the parallelization over the wavenumbers, however with the sectioning used, the memory requirement during the 2D modelling is less than 1 GB per thread utilized (not shown), and thus the total memory requirement is inconsequential on modern hardware. While parallelization over the sections require more memory than other approaches it also gives the best scalability for large surveys, because there is practically no inter-communication between the different threads. Section parallelization provides good largescale scaling, but it does not provide much benefit for small-scale problems. In order to remedy this, an additional parallelization over the frequencies of each section was implemented using OpenMP's collapse directive. By parallelizing over both sectioning and frequency, good scaling can be achieved for surveys of all sizes. Figure 12 shows the

parallel scalability of the code. It can be seen that the scaling is almost linear for low numbers of threads, whereas linear scalability is lost for higher numbers of threads due to memory bandwidth limitations.

Another key concept, when doing parallelization is affinity. That is how the parallel threads are bound to the various cores in the system. If thread affinity is not employed it can severely affect performance, especially on NUMA systems. Without affinity, the calculations of a thread are never confined to a single core, but rather executed in small portions executed on random cores of the system. This can have dramatic consequences since memory locality cannot be assured and data kept in cache is constantly lost. Figure 12 demonstrates two different affinity schemes, which are commonly employed: compact affinity and scattered affinity. When using compact affinity, thread spawning tends to cluster together on a NUMA node until all processors on the NUMA are engaged, whereas scattered affinity tends to spread out the thread spawning across all NUMA nodes. The two different affinity modes can have a significantly different performance depending on the problem to which they are employed. Because of the low level of intercommunication between the parallel threads, a practically identical scaling for the two affinities can be seen in Figure 12.

As a final comment to scaling, it should be mentioned that due to the way we do sectioning and inversion, our code has a linear scaling in compute time as a function of survey size (not shown here).

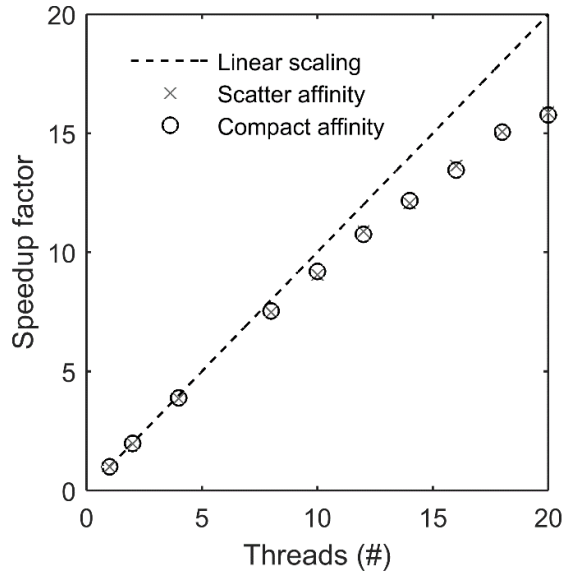

Figure 12 Parallel scaling of the code. The data are generated on a NUMA system with two Intel Xeon E5-2650 v3 CPUs, each with 10 cores. The threads are bound to specific logical processors, following either a compact affinity approach or a scattering affinity approach.

Performance

Our 2D code is capable of inverting surveys of virtually any size, due to the scalability introduced by sectioning. Thus far, the code has been successfully tested on a 100-line km survey with 10000 soundings. For such a survey, the code performs a full 2D forward and derivative calculation in ~5 hours on a NUMA system with two Intel Xeon E5-2650 v3 CPUs, each with 10 cores.

The total inversion time for the 100-line km survey can be seen in Table 2. Both the hybrid and 2D inversion reaches comparable misfits, but the hybrid scheme does so 2.3 times faster than the 2D. Though the performance numbers presented are representative, it should be mentioned that the number of iterations needed to reach convergence can vary quite heavily between different surveys. Obviously, this also makes inversion times vary quite heavily. Roughly speaking a pure 2D inversion can usually be done in

around 10-20 iterations, while a hybrid inversion requires 14-20 iterations. Note that the number of iterations and hence inversion time, depends heavily on the stopping criteria, which we have chosen to be a relative misfit change of less than 1%.

In the examples shown previously, the speedup gained from utilizing the hybrid scheme was 2.7x for the synthetic conductive lens, 6.6x for the horizontal conductivity contrast, 6x for the small field example, and 2.3x for a 100-line km. These are all very significant speedups, and they are generally generated without notably worsening the resulting model. The reason why the speedups vary largely depends on the number of iterations spent in stage 3 of the hybrid scheme, if only a few iterations are spent then the speedup is high in general, whereas if more than a few iterations are spent in stage 3, the speedup will generally be in the low end.

	100 line km	
	Iterations	Runtime (hours)
1D	15	0.1 h
Hybrid	4+8+5	36 s+4.9 h+26.0 h = 31 h
2D	15	71 h

Table 2 Runtime and iteration number for an inversion of a 100-line km survey conducted with the RESOLVE system. For the hybrid system, the iteration numbers and runtimes are given for each of the 3 stages.

CONCLUSION

We have presented an algorithm for hybrid 2D frequency domain forward modelling and inversions. The 2D forward and derivative calculations are done on a triangular finite element mesh using sectioning, while inversions are done on a regular grid. The finite element mesh is created with the inversion grid as the foundation, which makes interpolation between the meshes significantly easier. By

using sectioning and a regular grid for inversion, the code is able to handle large-scale inversions, which are otherwise often problematic for higher dimensional inversion codes. We have demonstrated how section sizes should be chosen to optimize computational times, and shown how forward and derivative calculations are optimally performed using different section sizes. Our parallelization goal was to achieve maximum speed; hence, the code is parallelized over both frequencies and sections. This gives the code high efficiency for both large and small surveys, as well as excellent scaling properties even on non-uniform memory architectures. Though focus was on computational speed, the memory consumption is less than 1GB per thread, and thus memory consumption for this algorithm was deemed inconsequential. Furthermore, we presented a hybrid 1D/2D scheme, which boosts the computational speed of 2D inversions by $\sim 2-6x$, without significantly reducing the accuracy. The concept of combining lower- and higher-dimensional algorithms in a hybrid scheme to significantly increase computational speed, is a largely unused optimization within the scientific community. We have demonstrated our algorithm with two successful synthetic examples and a field example.

ACKNOWLEDGMENTS

This study was supported by Innovation fund Denmark, through the AirTech4Water project. We furthermore thank Dr. Bernhard Siemon and BGR for the field data.

APPENDIX A

In order to recast the governing equations (13)-(14) into a system of linear equations, the finite element method is employed. In this regard, we substitute $\widetilde{E}_{sy}$ and $\widetilde{H}_{sy}$ by interpolated fields combined with second order shape functions:

$$\widetilde{E}_{sy}(x,z) = \sum_{i=1}^{n} N_i(x,z)\widetilde{E}_{sy,i}, \qquad \widetilde{H}_{sy}(x,z) = \sum_{i=1}^{n} N_i(x,z)\widetilde{H}_{sy,i}\ ,$$

where n is the number of nodes attached to one element. Replacing $\widetilde{E}_{sy}$ and $\widetilde{H}_{sy}$ in this way leads to an approximation of the Maxwell equations, which bear a residual. We use the weighted residual procedure to minimize the residual averaged over the area of each grid cell. As our procedure applies to

both equation (13) and (14) in the same way, we will only focus on equation (13). The weighting function for the residual is the same as the interpolation function, i.e. $N_i(x,z)$, and integration of both sides of the equation and applying the rule for integration by parts combined with Gauss' Theorem leads us to:

$$-i\omega\varepsilon_y \int_\Omega N^T N d\Omega\, \tilde{E}_{sy} + \frac{i\omega\varepsilon_x}{c_{zx}}\left[\oint_\Gamma N^T \frac{\partial N}{\partial x} d\Gamma + \int_\Omega \frac{\partial N}{\partial x}^T \frac{\partial N}{\partial x} d\Omega\right] \tilde{E}_{sy} + i\omega \frac{\varepsilon_z}{c_{xz}}\left[\oint_\Gamma N^T \frac{\partial N}{\partial z} d\Gamma + \int_\Omega \frac{\partial N}{\partial z}^T \frac{\partial N}{\partial z} d\Omega\right] \tilde{E}_{sy} - \frac{ik_y}{c_{zx}}\left[\oint_\Gamma N^T \frac{\partial N}{\partial x} d\Gamma + \int_\Omega \frac{\partial N}{\partial x}^T \frac{\partial N}{\partial z} d\Omega\right] \tilde{H}_{sy} + \frac{ik_y}{c_{xz}}\left[\oint_\Gamma N^T \frac{\partial N}{\partial x} d\Gamma + \int_\Omega \frac{\partial N}{\partial z}^T \frac{\partial N}{\partial x} d\Omega\right] \tilde{H}_{sy} = -(i\omega\varepsilon_{py} - i\omega\varepsilon_y) \int_\Omega N^T N d\Omega\, \tilde{E}_{py} + \left(\frac{i\omega\varepsilon_{px}}{c_{pzx}} - \frac{i\omega\varepsilon_x}{c_{zx}}\right)\left[\oint_\Gamma N^T \frac{\partial N}{\partial x} d\Gamma + \int_\Omega \frac{\partial N}{\partial x}^T \frac{\partial N}{\partial x} d\Omega\right] \tilde{E}_{py} + \left(\frac{i\omega\varepsilon_{pz}}{c_{pxz}} - \frac{i\omega\varepsilon_z}{c_{xz}}\right)\left[\oint_\Gamma N^T \frac{\partial N}{\partial z} d\Gamma + \int_\Omega \frac{\partial N}{\partial z}^T \frac{\partial N}{\partial z} d\Omega\right] \tilde{E}_{py} - \left(\frac{ik_y}{c_{pzx}} - \frac{ik_y}{c_{zx}}\right)\left[\oint_\Gamma N^T \frac{\partial N}{\partial x} d\Gamma + \int_\Omega \frac{\partial N}{\partial x}^T \frac{\partial N}{\partial z} d\Omega\right] \tilde{H}_{py} + \left(\frac{ik_y}{c_{pxz}} - \frac{ik_y}{c_{xz}}\right)\left[\oint_\Gamma N^T \frac{\partial N}{\partial x} d\Gamma + \int_\Omega \frac{\partial N}{\partial z}^T \frac{\partial N}{\partial x} d\Omega\right] \tilde{H}_{py}\,,$$

where Ω is the area of the respective element and Γ the element's boundary. Within the model domain the integrals of connected elements cancel each other out and at the model domain boundary, we assume Dirichlet boundary conditions, i.e. $\tilde{E}_{sy} = \tilde{H}_{sy} = 0$, hence the boundary integrals can be ignored. This finally results in the following system of linear equations:

$$-i\omega\varepsilon_y \int_\Omega N^T N d\Omega\, \tilde{E}_{sy} + \frac{i\omega\varepsilon_x}{c_{zx}} \int_\Omega \frac{\partial N}{\partial x}^T \frac{\partial N}{\partial x} d\Omega\, \tilde{E}_{sy} + i\omega\varepsilon_z \int_\Omega \frac{\partial N}{\partial z}^T \frac{\partial N}{\partial z} d\Omega\, \tilde{E}_{sy} - \frac{ik_y}{c_{zx}} \int_\Omega \frac{\partial N}{\partial x}^T \frac{\partial N}{\partial z} d\Omega\, \tilde{H}_{sy} + \frac{ik_y}{c_{xz}} \int_\Omega \frac{\partial N}{\partial z}^T \frac{\partial N}{\partial x} d\Omega\, \tilde{H}_{sy} = -(i\omega\varepsilon_{py} - i\omega\varepsilon_y) \int_\Omega N^T N d\Omega\, \tilde{E}_{py} + \left(\frac{i\omega\varepsilon_{px}}{c_{pzx}} - \frac{i\omega\varepsilon_x}{c_{zx}}\right) \int_\Omega \frac{\partial N}{\partial x}^T \frac{\partial N}{\partial x} d\Omega\, \tilde{E}_{py} + \left(\frac{i\omega\varepsilon_{pz}}{c_{pxz}} - \frac{i\omega\varepsilon_z}{c_{xz}}\right) \int_\Omega \frac{\partial N}{\partial z}^T \frac{\partial N}{\partial z} d\Omega\, \tilde{E}_{py} - \left(\frac{ik_y}{c_{pzx}} - \frac{ik_y}{c_{zx}}\right) \int_\Omega \frac{\partial N}{\partial x}^T \frac{\partial N}{\partial z} d\Omega\, \tilde{H}_{py} + \left(\frac{ik_y}{c_{pxz}} - \frac{ik_y}{c_{xz}}\right) \int_\Omega \frac{\partial N}{\partial z}^T \frac{\partial N}{\partial x} d\Omega\, \tilde{H}_{py}.$$

By creating and combining this system of equations and its counterpart resulting from equation (14), the desired linear system of equations is found:

$$\boldsymbol{A}\tilde{\boldsymbol{x}} = \boldsymbol{b},$$

where $\boldsymbol{A}$ is the global symmetric stiffness matrix, $\tilde{\boldsymbol{x}}$ contains the Fourier transformed EM-fields, and $\boldsymbol{b}$ contains the source terms.

REFERENCES

Abubakar, A., T. Habashy, V. Druskin, L. Knizhnerman, and D. Alumbaugh. 2008, 2.5 D forward and inverse modeling for interpreting low-frequency electromagnetic measurements. Geophysics, **73**, no. 4,F165-F177.

Auken, E., and A. V. Christiansen. 2004, Layered and laterally constrained 2D inversion of resistivity data. Geophysics, **69**, no. 3,752-761.

Auken, E., A. V. Christiansen, C. Kirkegaard, G. Fiandaca, C. Schamper, A. A. Behroozmand, A. Binley, E. Nielsen, F. Effersø, N. B. Christensen, and others. 2014, An overview of a highly versatile forward and stable inverse algorithm for airborne, ground-based and borehole electromagnetic and electric data. Exploration Geophysics, **46**, no. 3,223-235.

Beamish, D. 2003, Airborne EM footprints. Geophysical Prospecting, **51**, no. 1,49-60.

Caudillo-Mata, L. A., E. Haber, L. J. Heagy, and C. Schwarzbach. 2016, A Framework for the Upscaling of the Electrical Conductivity in the Quasi-static Maxwell's Equations. Journal of Computational and Applied Mathematics.

Christiansen, A. V., and E. Auken. 2004, Optimizing a layered and laterally constrained 2D inversion of resistivity data using Broyden's update and 1D derivatives. Journal of Applied Geophysics, **56**, no. 4,247-261.

Christiansen, A. V., E. Auken, C. Kirkegaard, C. Schamper, and G. Vignoli. 2015, An efficient hybrid scheme for fast and accurate inversion of airborne transient electromagnetic data. Exploration Geophysics,1-8.

Costabel, S., B. Siemon, G. Houben, and T. Günther. 2017, Geophysical investigation of a freshwater lens on the island of Langeoog, Germany–Insights from combined HEM, TEM and MRS data. Journal of Applied Geophysics, **136**,231-245.

Cox, L. H., G. A. Wilson, and M. S. Zhdanov. 2010, 3D inversion of airborne electromagnetic data using a moving footprint. Exploration Geophysics, **41**,250-259.

Cox, L. H., G. A. Wilson, and M. S. Zhdanov. 2012, 3D inversion of airborne electromagnetic data. Geophysics, **77**, no. 4,WB59-WB69.

Cuthill, E., and J. McKee. 1969, Reducing the bandwidth of sparse symmetric matrices. Paper read at Proceedings of the 1969 24th national conference.

Doyle, B., K. Kivi, and S. S. BH. 1999, The TU Kwi Cho (D027 and D018) Diamondiferous Kimberlite Complex, Northwest Territories, Canada.

Haber, E., D. W. Oldenburg, and R. Shekhtman. 2007, Inversion of time domain three-dimensional electromagnetic data. Geophysical Journal International, **171**, no. 2,550-564.

Hestenes, M. R., and E. Stiefel. 1952, Methods of conjugate gradients for solving linear systems. Vol. 49: NBS.
Jahandari, H., S. Ansari, and C. G. Farquharson. 2017, Comparison between staggered grid finite–volume and edge–based finite–element modelling of geophysical electromagnetic data on unstructured grids. Journal of Applied Geophysics, **138**,185-197.
Key, K., and J. Ovall. 2011, A parallel goal-oriented adaptive finite element method for 2.5-D electromagnetic modelling. Geophysical Journal International, **186**, no. 1,137-154.
Kirkegaard, C., and E. Auken. 2015, A parallel, scalable and memory efficient inversion code for very large-scale airborne electromagnetics surveys. Geophysical Prospecting, **63**, no. 2,495-507.
Li, W.-B., Z.-F. Zeng, J. Li, X. Chen, K. Wang, and Z. Xia. 2016, 2.5 D forward modeling and inversion of frequency-domain airborne electromagnetic data. Applied Geophysics, **13**, no. 1,37-47.
Liu, G., and A. Becker. 1990, Two-dimensional mapping of sea-ice keels with airborne electromagnetics. Geophysics, **55**, no. 2,239-248.
Marquardt, D. 1963, An Algorithm for Least Squares Estimation of Nonlinear Parameters. SIAM, Journal of Applied Mathematics, **11**,431-441.
Menke, W. 1989, Geophysical data analysis: discrete inverse theory. xii, 289 p vols, International geophysics series: Academic Press. Reprint, Not in File.
Mitsuhata, Y. 2000, 2-D electromagnetic modeling by finite-element method with a dipole source and topography. Geophysics, **65**, no. 2,465-475.
Mitsuhata, Y., and T. Uchida. 2002, 2-D inversion of frequency-domain EM data caused by a 3-D source. Methods in Geochemistry and Geophysics, **35**,153-171.
Panourgias, I. 2011, NUMA effects on multicore, multi socket systems. The University of Edinburgh.
Reid, J. E., A. Pfaffling, and J. Vrbancich. 2006, Airborne electromagnetic footprints in 1D earths. Geophysics, **71**, no. 2,G63-G72.
Siemon, B., S. Costabel, W. Voß, U. Meyer, N. Deus, J. Elbracht, T. Günther, and H. Wiederhold. 2015, Airborne and ground geophysical mapping of coastal clays in Eastern Friesland, Germany. Geophysics, **80**, no. 3,WB21-WB34.
Stoyer, C., and R. J. Greenfield. 1976, Numerical solutions of the response of a two-dimensional earth to an oscillating magnetic dipole source. Geophysics, **41**, no. 3,519-530.
Streich, R., M. Becken, and O. Ritter. 2011, 2.5D controlled-source EM modeling with general 3D source geometries. GEOPHYSICS, **76**, no. 6,F387-F393. doi: 10.1190/geo2011-0111.1.
Saad, Y. 1994, ILUT: A dual threshold incomplete LU factorization. Numerical linear algebra with applications, **1**, no. 4,387-402.
Saad, Y. 2003, Iterative methods for sparse linear systems: Siam.
Vöge, M. 2010, ngi25em Version 4.0 User Documentation.
Vöge, M., A. Pfaffhuber, E. Auken, C. Kirkegaard, T. Boesen, S. Hendricks, and P. Hunkeler. 2015, 2.5 D Inversion of Sea Ice Thickness from Helicopter EM Data. Paper read at First European Airborne Electromagnetics Conference.
Ward, S. H., and G. W. Hohmann. 1988, Electromagnetic theory for geophysical applications. Paper read at Electromagnetic methods in applied geophysics.
Wilson, G., A. Raiche, and F. Sugeng. 2006, 2.5 D inversion of airborne electromagnetic data. Exploration Geophysics, **37**, no. 4,363-371.
Wilson, G. A., L. H. Cox, M. Čuma, and M. S. Zhdanov. 2012, Inverting airborne geophysical data for mega-cell and giga-cell 3D Earth models. The Leading Edge, **31**, no. 3,316-321.
Yang, D., and D. W. Oldenburg. 2012a, Practical 3D inversion of large airborne time domain electromagnetic data sets. ASEG Extended Abstracts, **2012**, no. 1,1-4.
Yang, D., and D. W. Oldenburg. 2012b, Three-dimensional inversion of airborne time-domain electromagnetic data with applications to a porphyry deposit. Geophysics, **77**, no. 2,B23-B34.

Yang, D., D. W. Oldenburg, and E. Haber. 2014, 3-D inversion of airborne electromagnetic data parallelized and accelerated by local mesh and adaptive soundings. Geophysical Journal International, **196**, no. 3,1492-1507.

Yu, W. W., and E. Haber. 2012, A 2.5 D Inversion of Airborne Electromagnetic data. Paper read at 2012 SEG Annual Meeting.

Zienkiewicz, O. C., R. L. Taylor, and R. L. Taylor. 1977, The finite element method. Vol. 3: McGraw-hill London.

Appendix C

Paper 3

Submitted to Geophysical prospecting.

A parallel computing thin sheets inversion algorithm for airborne time domain data utilizing a variable overburden

Authors:

Tue Boesen, tue@geo.au.dk , Aarhus University, Denmark

Esben Auken. esben.auken@geo.au.dk, Aarhus University, Denmark

Anders Vest Christiansen, anders.vest@geo.au.dk, Aarhus University, Denmark

Gianluca Fiandaca, gianluca.fiandaca@geo.au.dk , Aarhus University, Denmark

Cyril Schamper, cyril.schamper@upmc.fr, Sorbonne Universités, UPMC Univ Paris 06, UMR 7619 METIS, F-75005, Paris, France

Running head: Thin sheet inversion

Corresponding author: Tue Boesen, Aarhus University, Denmark

Email: tue@geo.au.dk

Submission date:

Key words:

Electromagnetics, Inversion, Modelling.

ABSTRACT

Accurate modelling of mineralizations can often be difficult. In order to remedy this, a parametric approach is often used. We have developed a parametric thin sheet code, with variable overburden. The code is capable of performing inversions of time-domain airborne electromagnetic data, and it has been tested successfully on both synthetic data and field data. The code implements an integral solution containing one or more conductive sheets, buried in a half-space with a laterally varying conductive overburden. This implementation increases the area of applicability compared to e.g. codes operating in free-space, but it comes with a significant increase in computational cost. To remedy the cost, the code is parallelized using OpenMP and heavily optimized, which means that inversions of field data can be performed in hours on multiprocessor desktop computers. The code models the full system transfer function of the electromagnetic system, including variable flight height. The code is demonstrated with a synthetic example imitating a mineralization buried underneath a conductive meadow. As a field example, the Valen mineral deposit, which is a graphite mineral deposit located in a variable overburden, is successfully inverted. Our results match well with previous models of the deposit. These examples collectively demonstrate the effectiveness of our thin sheet code.

INTRODUCTION

Electromagnetic (EM) data are commonly used in subsurface detection and modelling. One of the earliest uses was the detection of mineralization, which often produces signals orders of magnitudes larger than the non-mineralized background. While detection of such deposits is easy, accurate modelling remains a challenge. In cases where sharp boundaries and large conductivity contrasts are indicated, it can often be beneficial to employ a parametric formulation, where the anomalies are modelled using locally defined discrete objects, described with only a few key parameters. This is often beneficial from a computational point of view, since a parametric approach drastically reduces the amount of parameters used in a model.

Historically, there have been several parametric approaches made in EM geophysics. Price (1948) introduced the thin sheet formulation, since then various authors (Annan 1974, Lajoie and West 1976, Vasseur and Weidelt 1977, Weidelt 1981, Walker and West 1991, Fainberg et al. 1993) have presented numerically stable integral equation formulations of the thin sheet problem. The formulation by Weidelt (1981) has been the foundation for several other papers that in some way extend the formulation, including: (Zhou 1989, Song et al. 2002), and this paper as well.

Roughly speaking, there are two common areas in controlled source EM where thin sheet modelling can be utilized: 1) mineral exploration, and 2) seabed oil exploration. In mineral exploration, free-space sheet modelling is commonly used today. Thin sheet modelling for oil exploration is possible using resistive sheets in conductive backgrounds (Constable and Weiss 2006, Swidinsky and Edwards 2010).

While thin sheet modelling is a well-known parametric model used in EM geophysics, other alternative parametrizations exist as well: Dorn et al. (2000), Dorn and Lesselier (2006) used a parametric model to simulate plumes from landfills; Aghasi et al. (2011) developed a general

parametric inversion framework using radial basis functions; McMillan et al. (2015) developed a 3D parametric hybrid inversion scheme for airborne EM data using skewed Gaussian ellipsoids to represent the target anomalies.

Focusing on thin sheet modelling, the simplest and most common approach is to consider a thin sheet in free space (Duncan 1987, Macnae et al. 1998). In mineral exploration, this is often a reasonable approximation, since the host rock is usually several orders of magnitudes more resistive than the mineral deposit. However, even though the free-space approximation is valid in many cases, there are many examples where the approximation breaks down (Reid et al. 2010, Wolfgram et al. 1998).

In order to extend the domain where sheet codes are applicable and improve their accuracy, we have gone beyond the free space approximation, and have extended a layered sheet code, originally developed for far field data in the frequency domain by Zhou (1989), to consider a two-layered earth where the top layer incorporates a variable overburden. The code, which will be described in detail in the following sections, is implemented in Fortran within an already established and robust inversion engine (Auken et al. 2014), and is optimized using task parallelization OpenMP directives, which provide superior CPU balancing compared to traditional loop parallelization. Furthermore, a sophisticated adaptive frequency sampler has been developed, in order to minimize the number of frequencies needed to transform the response to time domain. The code is capable of handling multiple sheets, and has the option of locking sheets together, in what is commonly referred to as a thick sheet. The code models the full system transfer function of any transient electromagnetic system. It has been extensively validated, both against 1D algorithms, as well as against the thin sheet code presented in Raiche (1998). Finally, we demonstrate the effectiveness of our sheet code by successfully inverting both a synthetic example as well as the Valen mineral deposit.

METHODOLOGY

Governing equations

Starting with Maxwell's equations, under the assumption that displacement currents are negligible, and the medium is non-magnetizable, the thin sheet theory is formulated following the approach of (Weidelt 1981, Zhou 1989). In space-frequency domain, Faradays and Amperes law are given as:

$$\nabla \times \boldsymbol{E}(\boldsymbol{r}) = -i\omega\mu_0 \boldsymbol{H}(\boldsymbol{r}), \tag{1}$$

$$\nabla \times \boldsymbol{H}(\boldsymbol{r}) = \boldsymbol{\sigma}(\boldsymbol{r})\boldsymbol{E}(\boldsymbol{r}) + \boldsymbol{J}_e(\boldsymbol{r}), \tag{2}$$

where $\boldsymbol{E}, \boldsymbol{H}$ are the electric- and magnetic fields, ω is the angular frequency, μ_0 is the vacuum permeability, $\boldsymbol{\sigma}$ is the conductivity, and $\boldsymbol{J}_e$ is the source current density. Equations (1)-(2) can be combined to give:

$$\nabla \times \nabla \times E(\boldsymbol{r}) + i\omega\mu_0 \boldsymbol{\sigma}(\boldsymbol{r})\boldsymbol{E}(\boldsymbol{r}) = -i\omega\mu_0 \boldsymbol{J}_e(\boldsymbol{r}). \tag{3}$$

This is combined with the thin sheet approximation:

$$\boldsymbol{n} \times (\boldsymbol{H}_+ - \boldsymbol{H}_-) = \tau(\boldsymbol{r})\boldsymbol{E}, \tag{4}$$

where $\boldsymbol{n}$ is a normal vector to the sheet, $\boldsymbol{H}_+, \boldsymbol{H}_-$ are the magnetic field above and below the thin sheet, and $\tau(\boldsymbol{r})$ is the conductance of the sheet.

From equation (3)-(4) an expression for the electric field anywhere in space can be found (Zhou 1989):

$$\boldsymbol{E}(\boldsymbol{r}) = \boldsymbol{E}_{\boldsymbol{n}}(\boldsymbol{r}) - i\omega\mu_0 \sum_{j=1}^{N_s} \int_{S_j} \tau_j(\boldsymbol{r}')\boldsymbol{G}(\boldsymbol{r},\boldsymbol{r}') \cdot \boldsymbol{E}_{S_j}(\boldsymbol{r}')dS', \tag{5}$$

where $\boldsymbol{E}_{\boldsymbol{n}}(\boldsymbol{r})$**,** is the primary electric field:

$$\boldsymbol{E}_{\boldsymbol{n}}(\boldsymbol{r}) = -i\omega\mu_0 \int_V \boldsymbol{J}_e(\boldsymbol{r}') \cdot \boldsymbol{G}(\boldsymbol{r},\boldsymbol{r}')dV', \tag{6}$$

where N_s is the number of sheets, S_j is the surface of the j'th sheet, τ_j is the conductance of the j'th sheet, $\boldsymbol{G}(\boldsymbol{r},\boldsymbol{r}')$ is the dyadic Greens function, and $\boldsymbol{E}_{S_j}$ is the tangential electric field on the j'th

sheet, V is the whole space volume excluding the volume occupied by the sheets, and $\boldsymbol{r}'$ being the corresponding position vector.

Since equation (5) is valid anywhere, it can also be used to find the electric field on the sheets, thus the electric field on the i'th sheet is given by the following closed form:

$$\boldsymbol{E}_{S_i}(\boldsymbol{r}) = \boldsymbol{E}_{\boldsymbol{n}}(\boldsymbol{r}) - i\omega\mu_0 \sum_{j=1}^{N_s} \int_{S_j} \tau_j(\boldsymbol{r}')\boldsymbol{G}(\boldsymbol{r},\boldsymbol{r}') \cdot \boldsymbol{E}_{S_j}(\boldsymbol{r}')dS'. \tag{7}$$

The electric field on the thin sheet is found by discretizing the sheet into rectangular cells and treating each cell as a dipole. By introducing an inductive- and a channelling-current, as suggested by Weidelt (1981), a coupling between the dipoles can be found. With the coupling matrix known, the response from the sheet to an external field can be found. Finally, in order to get the response in the time domain, a fast Hankel transform is utilized (Johansen and Sørensen 1979).

Sheet-modelling with a varying overburden

The computation of the sheet response with a smooth varying conductive overburden, is done by computing one common layered background from all the 1D layered models in the modelling domain. Each of the 1D models represent a sounding measured by the AEM system. The secondary electric fields derived from the sheets are then computed using equation (7), and the fields are added to the layered response from each of the soundings. Computing one common layered background, is an approximate mapping that relies on the assumption that the elevation and background resistivity do not vary abruptly, such that the average background model, in which the sheet is calculated, is representative of the actual background. An illustration of this mapping can be seen in Figure 1, and will be explained more thoroughly in the following.

The mapping is made by giving each sounding an individual weight for each sheet, where the weight, w_{ij}, of the i'th sounding in comparison to the j'th sheet is given as:

$$w_{ij} = \frac{\tau_j}{d_{ij}^2}, \tag{8}$$

with τ being the conductance of the sheet, and d the distance between the sounding and the sheet. The conductance contributes to the weight to quantify the importance of the sheet in comparison to other sheets, while the distance quantifies the importance of the sounding in comparison to other soundings. Thus, the weight ensures that soundings close to the sheet have a larger impact on the common background model, while soundings far away play a negligible role.

The normalized weights, $\widehat{w}$, are then given as:

$$\widehat{w}_{ij} = \frac{w_{ij}}{\sum_{m=1}^{N_{sound}} \sum_{k=1}^{N_{sheet}} w_{mk}} \tag{9}$$

and the weighted average parameters, $\overline{m}$, are calculated as:

$$\overline{m} = \sum_{i=1}^{N_{sound}} \sum_{j=1}^{N_{sheet}} \widehat{w}_{ij} m_i \tag{10}$$

Equation (10) is used to determine the average parameter values of: elevation, E, thickness, T, and conductivity of layer 1 and 2, σ_1, σ_2 – all of which are needed in order to create the common background model used for the sheet calculation, as seen in Figure 1.

Once the common background model has been determined, the sheet response is calculated based on equation (5)-(7), and its constituent magnetic field equations. The variable overburden is included in the total magnetic field, H_T, by adding the secondary magnetic field from the sheet, H_S, to the layered magnetic field responses, H_L, based on 1D models at each sounding position.

$$H_T = H_S + H_L \tag{11}$$

One way to look at this is that variable overburden is included by dropping the common background response from the sheet calculation, and instead recalculating this using the individual 1D models. Thus the additional cost of using variable overburden, in comparison to a two layer homogenous

background, is a computation of all the 1D-background responses for each iteration, which is almost negligible in comparison to the cost of the thin sheet calculation.

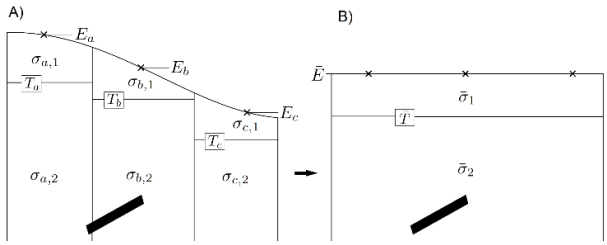

Figure 1 Illustrates the mapping from individual 1D soundings, to an average background model used for sheet calculation. A) shows three individual 1D models, with unique elevation, E, conductivities, σ, and thicknesses, T, for all soundings. B) shows the resulting average background model used for the sheet calculation, where all the shown parameters are now weighted mean values calculated in accordance with equation (10).

Modelling the system response

The full system response is calculated following Auken et al. (2014). This implies that the actual bandwidth of the receiver coil and the receiver instrument is modelled using Butterworth filters (Effersø et al. 1999) and the current waveform is modelled with piecewise linear elements (Fitterman and Stewart 1986). The shape of the transmitter loop is modelled by integrating the response from horizontal electric dipoles following the path of the transmitting wire.

Inversion

The objective function to be minimized in the inversion problem is given as:

$$q = q_{obs} + q_{prior} + q_{reg} \tag{12}$$

with q_{obs} being the observed data misfit, q_{prior} is the misfit to the prior model information about both the layered models as well as sheets, and q_{reg} is the misfit to the regularization of the layered models. A least-squares solution (L2-norm) is used to minimize the objective function incorporating a Tikhonov regularization scheme. The scheme is an extension of the inversion algorithm described in (Auken et al. 2014, Auken and Christiansen 2004).

The n'th iterative update of the model vector $\mathbf{m}$, (which is described in greater detail in Table 1), is given as:

$$\mathbf{m}_{n+1} = \mathbf{m}_n + \left(\widehat{\mathbf{G}}_n^T \mathbf{C}_n^{-1} \widehat{\mathbf{G}}_n + \lambda_n \mathbf{\Gamma}_n\right)^{-1} \cdot \left(\widehat{\mathbf{G}}_n^T \mathbf{C}_n^{-1} \delta \hat{\mathbf{d}}_n\right), \qquad (13)$$

where λ is a damping parameter, $\mathbf{\Gamma}$ is a diagonal scaling matrix, $\delta\hat{\mathbf{d}}$ is an extended perturbed data vector, $\widehat{\mathbf{G}}$ is the extended Jacobian, and $\hat{\mathbf{C}}$ is an extended covariance matrix, where the extensions are the a priori information and regularization:

$$\delta\hat{\mathbf{d}} = \begin{bmatrix} \mathbf{d} - \mathbf{d}_{obs} \\ \mathbf{m} - \mathbf{m}_{prior} \\ -\mathbf{R}\mathbf{m} \end{bmatrix} \qquad (14)$$

$$\widehat{\mathbf{G}} = \begin{bmatrix} \mathbf{G} \\ \mathbf{P} \\ \mathbf{R} \end{bmatrix} \qquad (15)$$

$$\hat{\mathbf{C}} = \begin{bmatrix} \mathbf{C}_{obs} & 0 & 0 \\ 0 & \mathbf{C}_{prior} & 0 \\ 0 & 0 & \mathbf{C}_{reg} \end{bmatrix} \qquad (16)$$

With, $\mathbf{d}$ being the forward response data, $\mathbf{d}_{obs}$ is the observed data, $\mathbf{m}_{prior}$ contains any a priori information about the model parameters, $\mathbf{R}$ is the roughness matrix defining which model parameters that are constrained to each other, $\mathbf{G}$ is the Jacobian, $\mathbf{P}$ defines the constraints of the a priori information. $\mathbf{C}_{obs}$, $\mathbf{C}_{prior}$, and $\mathbf{C}_{reg}$ are covariance matrices for the observed data, the prior information, and the roughness matrix. The diagonal scaling matrix, $\mathbf{\Gamma}$, is scaled individually for the different types of model parameters in the linear system (which are listed in Table 1). The reason

for this is that the different types of model parameters have vastly different sensitivities, and in order to prevent any type of model parameters from being overdamped, each model parameter type is damped individually.

The model parameters of the inversion are given in Table 1. Several different characterizations of the sheet were considered, but by characterizing the sheets with a central point and the strike/dip angles, a covariance analysis revealed that these parameters are the least coupled, and thus overall best suited for inversion. Furthermore, the strike/dip angles of the sheet can often be predicted to some degree based on the data streams, and can thus be given a reasonable initial value for the inversion.

MODEL PARAMETERS	
For each sounding	**For each sheet**
ρ_1	τ
ρ_2	x
T	y
A	z
	L_x
	L_y
	θ
	φ

Table 1 Parameters considered by the sheet inversion algorithm. Each sheet is characterized by eight parameters, while each sounding is characterized by four parameters. The four sounding parameters are: ρ_1 − resistivity of first layer, ρ_2 − resistivity of second layer, T − thickness of first layer, and A − flight altitude. The eight sheet parameters

are: $\tau -$ conductance, $(x, y, z) -$ coordinate of the sheet-centre, $L_{x/y} -$ length of sheet in x/y-direction when all angles are 0, $\theta -$ strike angle in comparison to x-axis, and $\varphi -$ dip angle.

Optimization steps

Dynamic cell discretization

When doing sheet inversion, the sheet is free to move in the subsurface and change size and shape. While the sheet is changing shape, it is imperative that the cell-discretization remains sufficiently fine. Because of this, a dynamic discretization of the sheet was implemented, which ensures sufficient cell discretization of the sheet, while also keeping the cells as square as possible. The dynamic discretization is given an upper and lower bound for the number of cells each sheet can contain, as well as a desired cell size. Each sheet is then initially discretized with cells as close to square as possible, with the desired cell size. If the number of cells falls outside the allowed number of cells, the cells are then lengthened or shortened to meet this criterion as well.

The reason to keep the cells as square as possible is that it gives a higher accuracy to the integration over the sheet than if using elongated cells (not shown).

During a typical inversion, roughly 200-1000 cells will be used, depending on the number of sheets, the size of the sheets, and the desired accuracy.

Adaptive frequency sampler

Transient EM modelling codes are often formulated in frequency domain, which means that a transformation to time domain is required. This is most efficiently done using a Fast Hankel Transform. For such a transformation to be accurate ~ 100 frequency responses need to be calculated. In our case, a high precision adaptive fast Hankel transformation with 14 points per

decade is used, for as many decades as needed. This usually results in ~200 frequency responses that need to be determined.

A Hankel transformation can be done using either the real or the quadrature part of the magnetic field. We chose to use the quadrature part, since the adaptive sampler described below performs better on this part, due to the quadrature part being smoother, and thus easier to interpolate than the real part.

In 1D codes, computing a single frequency response is a computational inexpensive process, but for higher dimensional codes, including thin sheet modelling, calculating a frequency response becomes computationally expensive. This means that it can be computationally beneficial to calculate only selected frequencies, and then interpolate to get the remaining. In order to do this, an adaptive frequency sampler was developed. The adaptive sampler consists of an initial stage, an adaptive stage, and a final interpolating stage. In the initial stage, the frequency sampler starts by calculating a small number of frequencies, spread equidistantly in log-space between $10^{-4} - 10^{8}$ Hz, as well as a single point at 10^{-7}Hz. The total number of initial frequencies is dynamically determined to be divisible with the number of CPUs utilized. At high frequencies, the sheet response falls rapidly towards zero, and thus becomes negligible compared to the background response as seen in Figure 2 A). From the initial calculated frequencies, a dynamically determined frequency limit, ω_{max}, is made. Where all calculated frequencies higher than ω_{max} fulfil the criteria that the sheet-to-background response ratio is less than 10^{-4}. For frequencies higher than ω_{max}, it is assumed that the sheet response is negligible, and thus sheet responses are not calculated above ω_{max} during the adaptive sampling.

The adaptive sampling can be envisioned to operate in iterations, where an iteration starts with an interpolation error sampling of the frequency spectrum within $10^{-4} - \omega_{max}$ Hz. This is done by

going through each calculated frequency except the first and last. For each frequency, its surrounding calculated frequencies are used in an interpolation to estimate the frequency response, which is compared with the actual value. The result of such an interpolation error estimation can be seen in Figure 2 B). The frequencies with the highest interpolation error are refined by calculating two additional frequency responses around the central frequency. This is done for as many frequencies as needed for all CPUs to be working, or until all calculated frequencies have been calculated to a satisfactory level of accuracy. Once a thread has finished its calculation, and there are no more available tasks to compute, the next iteration starts. This procedure is repeated until sufficient accuracy is reached, or all frequencies needed for the Hankel transform, within the interval, have been calculated. For frequencies below 10^{-4} Hz, the sheet response shows an asymptotic behaviour that makes accurate interpolation possible.

The final stage consists of doing an interpolation of all the frequency responses, including the 10^{-7} Hz point, which was calculated for additional accuracy of the low frequency interpolation.

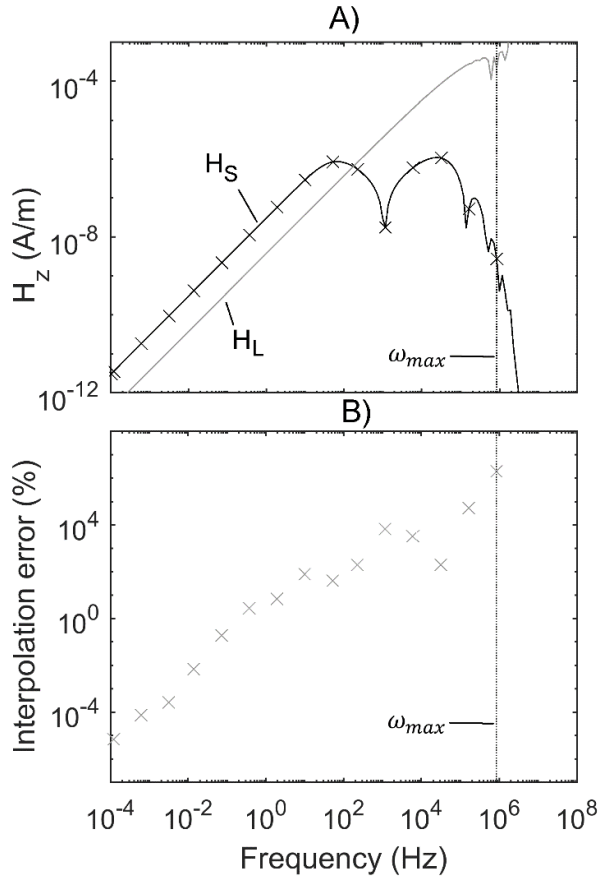

Figure 2 Illustrates the adaptive frequency sampler. A) The quadrature part of the magnetic z-component is shown as a function of frequency for both the sheet, H_S, and the layered background, H_L. The lines show the responses for all 14 points per decade, which are needed during the Hankel transform, while the crosses on the sheet response curve, are the initial equidistant responses. ω_{max} is shown as a dashed line, and indicates the frequency where sheet responses become negligible and are not calculated during the adaptive sampling. B) shows the interpolation error based on the initial sampling. Additional frequencies are calculated around the frequencies with the highest error.

The interpolation routine itself is adaptive, and uses either a four- or a six-point natural spline interpolation. A four-point natural spline is used for the two endpoints at either end, and a six-point natural spline is used for all other points.

If the sheets are calculated with very few cells – which is sometimes done in preliminary tests, natural spline interpolation becomes too computationally demanding compared to the amount of time the sheet calculation takes. In this case a simpler linear interpolation is used to estimate the accuracy. The reason it becomes too expensive, is that the spline interpolation must be done for each receiver, and because it has to be done in an OpenMP critical section, which means that no other parallel thread can access this data while it is happening. Once the adaptive sampling is completed, any frequency needed for the Hankel transform that has not explicitly been calculated during the adaptive scheme, is interpolated using natural spline interpolation with all calculated frequencies included.

The benefits gained by using this adaptive frequency sampler is roughly a halving of the number of frequency calculations performed. Thus, among the $\sim 170 - 200$ frequencies needed for the Hankel transform, around $\sim 60 - 90$ frequencies with sheet response are usually calculated.

Parallelization and scalability

Since the paradigm shift in CPUs happened around 2005, where advancements in clock frequency stagnated and multicore CPUs were introduced, parallelization has become an increasingly important consideration for numerical modelling. Moore's law of exponential computational growth is still more or less observed over the last decade, but only if vectorization and parallelization are utilized. On top of this, non-uniform memory access (NUMA) systems have been introduced

(Panourgias 2011). NUMA systems make data placement essential, and if done incorrectly a NUMA system can actually run slower by utilizing parallelization.

Our thin sheet formulation operates in the frequency domain, which makes parallelization significantly simpler than a time domain formulation. Parallelization across frequencies is largely independent and usually not memory bandwidth restricted, since the frequency calculations are sufficiently compute heavy in comparison to the amount of communication required between the threads. Thus, when frequency responses are calculated in an optimized loop parallelization, the scalability is almost linear. Since the number of frequencies that needs to be calculated during the adaptive sampling is unknown, loop parallelization would be suboptimal. Instead, OpenMP task parallelization is employed. This allows tasks to be dynamically spawned, and any available thread to perform the task. Thus near optimal work balancing across all threads is ensured.

Figure 3 A) shows the scaling of the code both when running with adaptive sampling on and without. The main reason why a linear scaling is not observed, is that the total number of frequencies being calculated are, in general, not divisible with the number of threads. Thus, at the end of a sampling, some of the threads will remain idle while the last few frequencies are being calculated. When running with the adaptive sampler, this is even more pronounced since it calculates significantly fewer frequencies than when running without it. Nevertheless, the effectiveness of the sampler can be seen in Figure 3 B), where the computational time is shown.

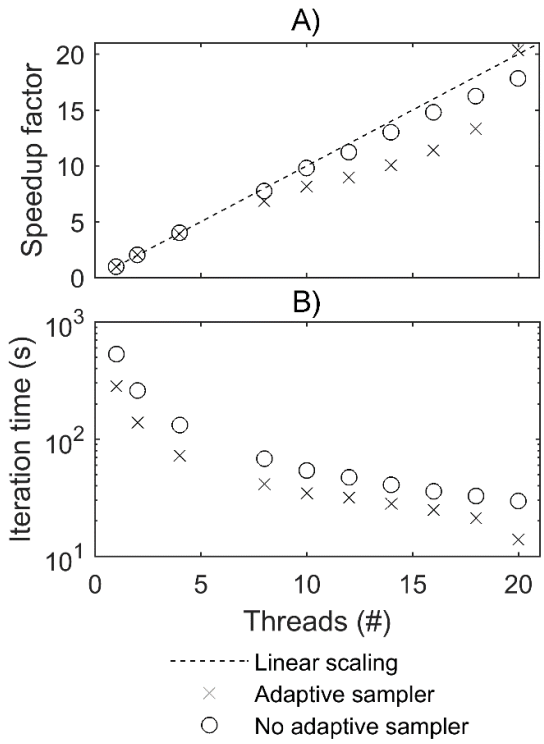

Figure 3 Parallel scaling of the thin sheet code. Tests were performed on a modern NUMA system with two Intel Xeon E5-2650 v3 CPUs, each with 10 cores. A) shows the scaling with number of threads, while B) shows the iteration time. The tests shown here were performed on a system with 90 soundings and 500 sheet cells.

RESULTS AND DISCUSSION

Validation

Forward modelling of the thin sheet code has been thoroughly validated against the thin sheet code known as Leroi Air (Raiche 1998). Differences in forward responses of around 0.1% or less were observed for all three components of the magnetic field, when the sheet response is dominant. A comparison of the quadrature part of the responses is seen in Figure 4. Note that the high frequency

difference between the total magnetic field, H_t, calculated by Leroi and our code, happens when the sheet response, H_s, is significantly smaller than the total magnetic field. As such, it is not a difference in the sheet response that is observed, but rather a difference in the layered background response. Our background response however, is validated against the well-established 1D modelling code (Auken et al. 2014). Thus, we believe that the high frequency difference seen when comparing with Leroi Air, likely stems from uncertainties because of single float precision in Leroi Air.

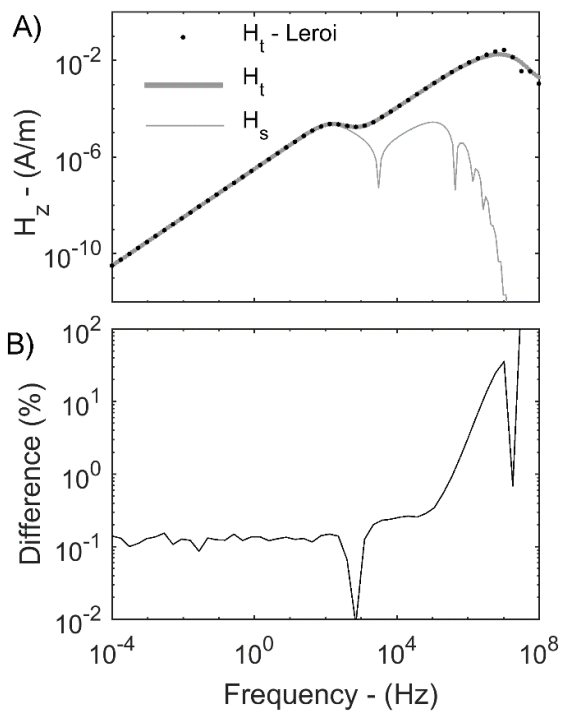

Figure 4 A comparison between Leroi Air and the sheet code. The model consists of a 100 S square sheet, placed at 50 m depth, with a length of 100 m, in a homogenous background of 1000 Ωm. The transmitter is a 22x22 m^2 square loop, placed on the ground, 25 m off-centre in comparison to the underlying sheet, while the receiver is placed in the centre of the transmitter. Panel A) shows the imaginary part of the magnetic field as a function of frequency and panel B) shows the relative difference between the total magnetic fields: H_t and H_t - Leroi

Synthetic model

A synthetic model was created to test the sheet code with variable overburden. A 3D overview of the modelling system can be seen in Figure 5A), it consists of: a 25 m thick overburden, with a conductive part centrally, and a highly resistive background with an almost vertical sheet placed at a depth of 120 m. The technical specifications of the SkyTEM516 system are used (see SkyTEM webpage for specifications), including both a low and a high moment, with the earliest gate being at 0.22 ms, and the latest gate being at 11 ms. The current of the low moment is 5.3 A, while the high moment operates at 113.9 A. The survey contains three lines of 30 soundings each, spaced 100 m apart, with 17 m between each sounding in a line, flown at a height of 30 m.

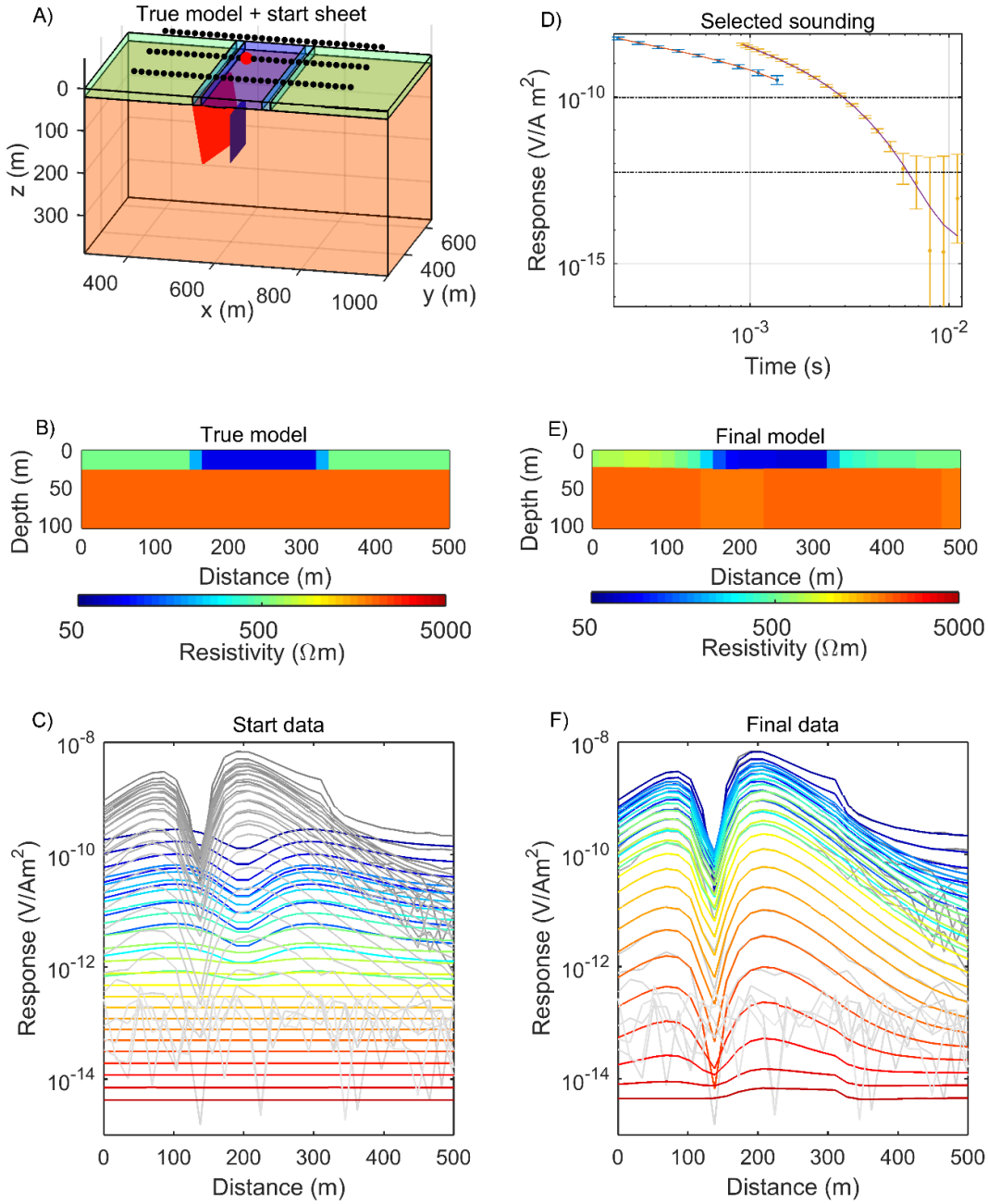

Figure 5 Shows the synthetic model. A) shows a 3D overview of the synthetic modelling system. The black dots indicate soundings, while the red dot is the selected sounding shown in D). The red sheet is the true sheet, while the blue sheet shows the sheet at the beginning of the inversion, (the final sheet is not shown as it coincides almost perfectly with the

true sheet, see Table 2). B, E) shows the true/final resistivity model along the central flight line. C, F) shows data from all gates for all soundings in the central flight-line. Each line in the figure represents data from a particular gate shown across all soundings in the central flight-line. The grey lines are the true data, while the coloured lines are the forward response from the starting/final model. D) shows the true data from a single sounding station with error bars, as well as the final forward response from the inversion. The location of the selected sounding is indicated by a red dot in A). Both high-moment (yellow) and low-moment (blue) data are shown. The horizontal black dashed lines indicate the noisefloors for the low moment and high moment. Note that only the z-component of the magnetic field has been used during this inversion.

The uncertainties on the data contain 10 % uniform noise as well as a 1 $\mathrm{nV/m^2}$ noisefloor, while the data have been perturbed by 10% of the uncertainty. The resulting noisefloor for the low and high moment, can be seen in Figure 5 D).

The starting model was set to 1000 Ωm for the overburden (15 m thick) and 2000 Ωm for the background. Constraints and standard deviations are given as factors and follow Auken et al. (2014), this means that 1.0 is perfect resolution, while 1.1 corresponds to a standard deviation of 10%.

The lateral constraint factors on the resistivity were set to 2 and 1.1 for the overburden and background and the lateral constraint on the thickness was set to 1.1. A prior of 0.6 m was put on the altitude with a lateral constraint of 1.01. The sheet was started with half the true conductivity, and as a completely square and vertical sheet 40 m off from the true position in both x, y, and z. Looking at Figure 5C) we believe this is a fair starting point, since manual inspection clearly shows

the approximate position of the sheet to well within these starting parameters. The sheet was restricted to 300-600 cells during the inversion, with a desired cell length of 5 m.

The inversion ran until a relative norm change of less than 0.7 % was obtained, which took 28 iterations, and was completed in ~10k seconds on a NUMA system with two Intel Xeon E5-2650 v3 CPUs, each with 10 cores. The results of the inversion can be found in Figure 5 D,E,F) and Table 2.

			Variable overburden		Free-space
Sheet Parameter	Starting	True	Final	STD factor	Final
τ (S)	15	30	30	1.01	24
x (m)	590	550	550	1.00	557
y (m)	510	470	469	1.00	468
z (m)	160	120	120	1.04	133
L_x (m)	100	200	200	1.01	220
L_y (m)	100	150	149	1.01	180
θ (°)	90	80	80	1.00	80
φ (°)	90	100	100	1.00	103
Data residual	5.56	-	0.11	-	1.6

Table 2 Details on the progression of the sheet parameters and the data residual during the inversion. The final sheet parameters are given for an inversion with both variable overburden and free-space. The standard deviation factors are determined by a linearized sensitivity analysis (Auken et al. 2014) of the parameters at the end of the inversion. Note that the data residual is normalized with the noise.

From Table 2 it is seen that the inversion with variable overburden finds the true sheet. Furthermore, based on the STD factors, the inversion parameters are very well determined. As can be seen in Figure 5 E) the inversion finds the conductivity structure of both the overburden and background with only small variations from the true model. This is true for all three lines, which are practically identical.

For comparison, Table 2 also contains the sheet parameters from a similar inversion, but with the sheet in free-space. In this case the sheet is still reasonably well determined, but the added accuracy of the inclusion of variable overburden is clearly demonstrated.

Field example – Valen mineral deposit

The Valen mineral deposit is located in the central region of the Musgrave province in the western part of South Australia. Geologically, the overall area consists of mafic units belonging to the Giles Complex, with occasional conductive overburdens consisting mainly of sand or a thick regolith cover of paleovalley sediments (Eadie and Prikhodko 2013, Effersø and Sørensen 2013).

In 2011 Geotech flew a survey over what is now known as the Valen deposit (Eadie and Prikhodko 2013). The Valen deposit was modelled using Maxwell plate modelling, and several plate models were proposed based on various time gates, see Figure 6. Based on these models, two drillings were committed to the Valen deposit, where one of the drillings found a massive 40 cm graphite layer at 89 m depth, and a smaller graphite layer at ~100 m depth, both of which are attributed to the conductive response of the Valen deposit. Provided that these mineralizations are the only ones present, and that they run parallel, they should be close enough to be accurately modelled as a single thin sheet.

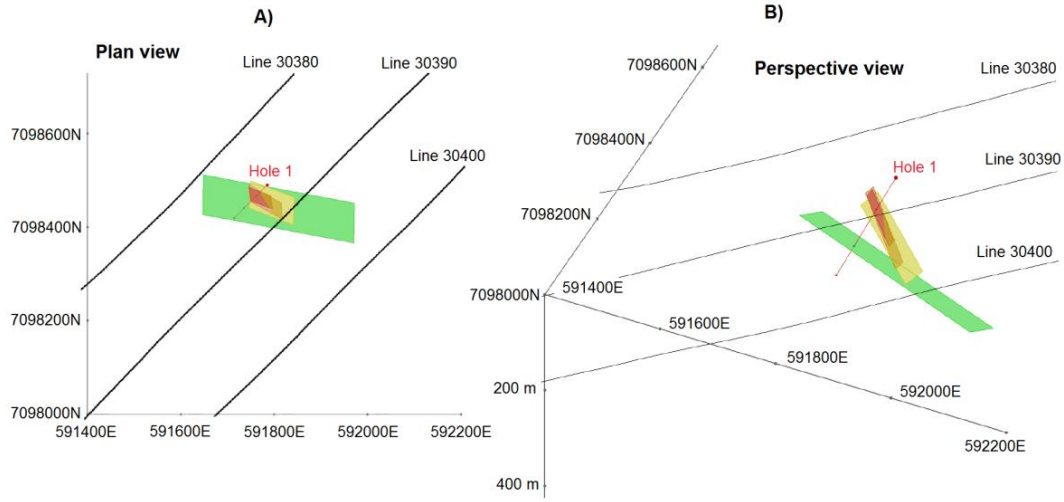

Figure 6 Shows VTEM flight-lines around the Valen mineral deposit, as well as Geotech's four proposed sheet models made in Maxwells plate simulation program, to fit various different time gate ranges. Based on these plate models, a drilling dubbed Hole 1 was proposed. A) shows a plan view, while B) a perspective view. The figures are modified from Blundell (2012).

Based on the VTEM data we have performed a sheet inversion of the Valen deposit. The data uncertainty was set to 5%. A pragmatic low-pass filter of 12 kHz with a primary field damping of 90% was chosen, along with larger uncertainty in the early gates, in order to remove any system response from the data. For the same reason gates before 0.25 ms were discarded and the earliest two gates used were given additional uncertainty. For the inversion a section of flight lines: 30380, 30390, and 30400, was processed and used. The flight lines have a spacing of 200 m between them. Though the sheet is essentially only visible in line 30390, the other lines were kept to help constrain the sheet. The VTEM data was originally sampled at 10 Hz, but was stacked to create 2 Hz soundings, for a total of 96 soundings, with an average inline sounding distance of ~17 m.

Based on 1D modelling of the data, it was clear that the regional geology changes from something moderately resistive in the northeast, to highly resistive hardrock in the southwest. Consequently,

the starting model was chosen to reflect this. The starting resistivities were chosen to be 275 Ωm for the soundings in the north east, and 1500 Ωm overburden with 2000 Ωm background for the soundings in the south west. Between these two areas, a group of 5 soundings is set with intermediate value of 800 Ωm.. The thickness of the overburden was uniformly set to 50 m. A priori uncertainties of 2 and 1.1 were placed on the resistivities of the overburden and background respectively. Lateral constraints were placed on the resistivities and thickness in order to enforce approximate homogeneity for the background model, with values of: 2, 1.1, and 1.1 being chosen for resistivities of the overburden, background, and the thickness.

The starting values for the sheet can be seen in Table 3, and were chosen based on the suggested Maxwell models for the Valen deposit, but were otherwise given complete freedom to change. The sheet was restricted to 300-600 cells during the inversion, with a desired cell length of 5 m.

The inversion took six iterations, and was done in ~13 minutes, on a NUMA system with two Intel Xeon E5-2650 v3 CPUs, each with 10 cores. The results from the inversion can be seen in Figure 7 and Table 3.

Figure 7 only shows details from the central line, since this is the only line where the sheet response is detectable. The two surrounding lines merely provide constraints for the sheet, but do not notably help to pinpoint the exact location of the sheet.

The high conductance closest to the sheet location in the resistive background in Figure 7 E), suggest that a single sheet is not sufficient to account for the entire signal found. This is further seen in Figure 7 D) where a deviation is observed at late times, suggesting that part of the sheet has a higher conductance.

Since the drillings do not go through our predicted sheet model, a comparison of the ground truth and our predicted sheet model remains inconclusive. It is possible that there is an even larger

dominating mineralization at the location predicted by our model. However, it is also possible that the graphite found during the drilling is the only vein and that our model is off by ~50 m. If that is the case, then several factors could be contributing to this. First, it could be that the mineralization is simply not shaped in a way that can be well modelled by a thin sheet. Secondly, the sheet is only measured on one flight line, and since we only had access to the z-component from that line, it is reasonable to expect a relatively high uncertainty on the position of the predicted sheet.

Comparing our model with the Maxwell models; the models are overall in agreement about the position, shape and angle of the sheet, though the conductance of our sheet is significantly lower than all theirs, which is likely because Maxwell uses a freespace background, and hence their sheet tries to compensate for the background signal as well. While our model corresponds well with Maxwell's model, we believe that our method is superior due to several reasons. First, we are able to present a single sheet, which reasonably models the Valen mineralization for all the used gates, and since our results are derived through inversions, they are in that sense more objective. Furthermore, our approach provides a data misfit, which we believe is a valuable objective parameter, when determining the trustworthiness of a model.

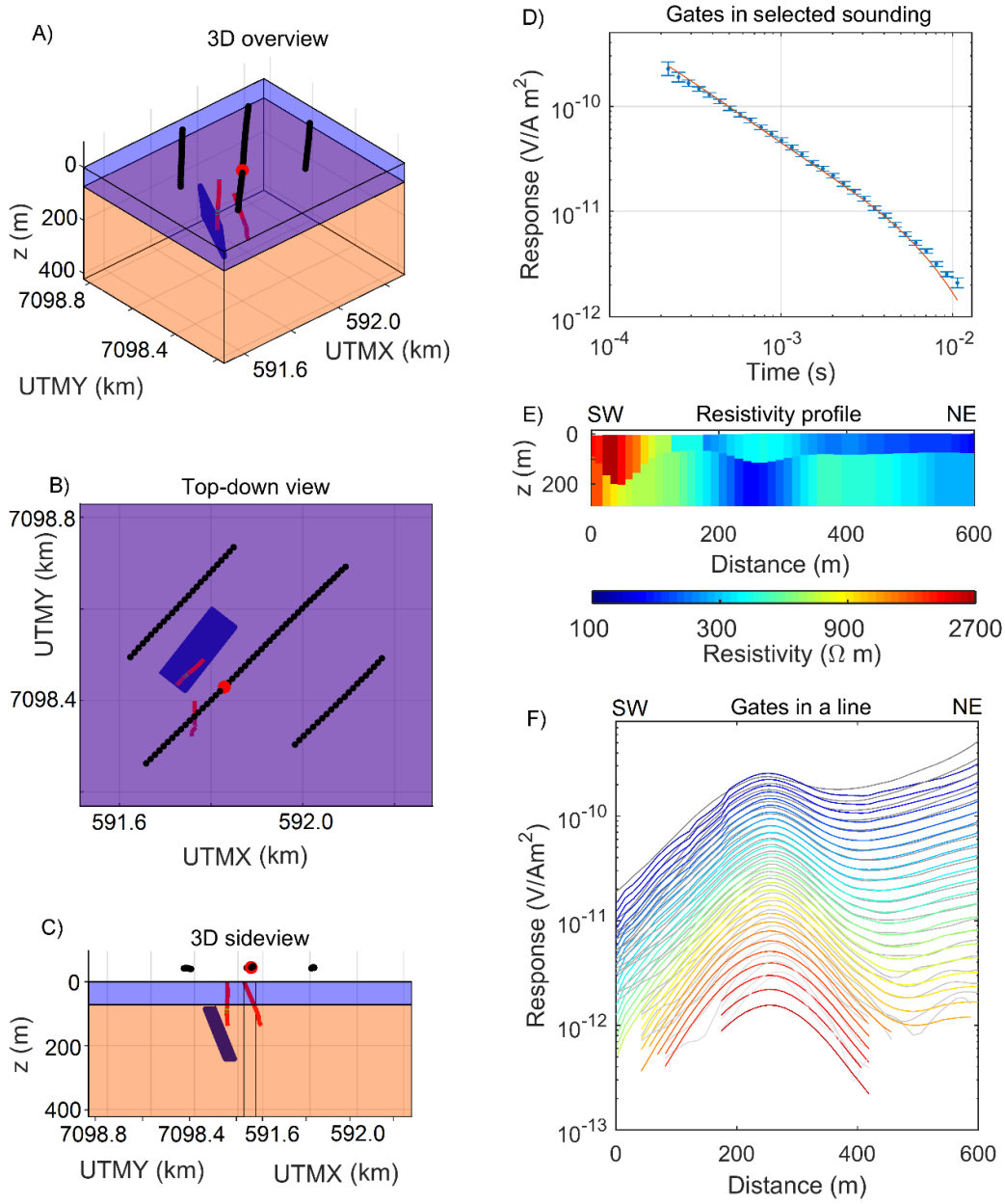

Figure 7 Inversion results from the Valen deposit. A-C) shows a 3D overview of the flight lines, the final sheet, as well as the two drillings conducted in the area. The black dots indicate soundings, while the red dot is the selected sounding shown in D), the red lines indicate the two drillings, with the green stripes being the location of the graphite mineralization encountered in the drilling – Note that only one of the two drillings encountered the

graphite mineralization. D) shows a comparison of forward and observed data, with error bars, for all gates in the selected sounding. E) shows the final 1D resistivity models below the central line. F) shows a comparison of forward and observed data, for all gates in the central flight-line. Each line represents a specific time-gate. All coloured lines are forward model data, while the grey lines are observed data. Note that only the z-component of the magnetic field has been used during this inversion.

	Starting	Final	STD factor
Conductance (S)	300	205	1.02
UTMX (km)	591.844	591.776	1.00*
UTMY (km)	7098.463	7098.508	1.00*
depth (m)	150	167	1.03
Width (m)	150	172	1.02
Length (m)	150	178	1.06
Strike angle (°)	231	232	1.00
Dip angle (°)	40	68	1.00
Data residual	7.5	1.9	-

Table 3 Details the progression of the sheet parameters and the data residual during the inversion of the data from the Valen deposit. The standard deviation factors are determined by a sensitivity analysis of the parameters at the end of the inversion in order to calculate how well determined the parameters are. *For completeness sake, it

should be noted that the Standard deviation factors of UTMX and UTMY are calculated in a local coordinate system, where the final sheet position is given as $(x, y) = (458, 545)$.

CONCLUSION

We have developed an advanced thin sheet code capable of performing a full non-linear inversion of AEM data. The thin sheet is calculated in a two-layered background, and a variable overburden is furthermore included. The background and overburden are based on 1D models, which are mapped from 1D local models to a regional average sheet background as a weighted mean. Significant time and resources have been spent in parallelizing and optimizing the performance of the sheet code, which includes dynamic cell discretization, and an OpenMP task parallelized adaptive frequency sampler. This means that the code is capable of doing inversion of field data in a matter of hours on a desktop computer. The effectiveness of the code was shown both on a synthetic example emulating a variable overburden, where the code showed significant improvement over free-space sheet modelling, as well as the Valen mineral deposit, which is located in an area with changing background geology.

ACKNOWLEDGMENTS

This study was supported by Innovation fund Denmark, through the AirTech4Water project. Furthermore, we would like to thank our colleague Kristoffer Andersen for many helpful discussions and insights about the underlying theory. Finally, we thank Tim Munday and CSIRO for the field data.

REFERENCES

Aghasi, A., Kilmer, M. & Miller, E.L. 2011. Parametric level set methods for inverse problems. *SIAM Journal on Imaging Sciences* **4**, 618-650.

Annan, A.P. 1974. The equivalent source method for electromagnetic scattering analysis and its geophysical application. Memorial University of Newfoundland.

Auken, E. & Christiansen, A.V. 2004. Layered and laterally constrained 2D inversion of resistivity data. *Geophysics* **69**, 752-761.

Auken, E., Christiansen, A.V., Kirkegaard, C., Fiandaca, G., Schamper, C., Behroozmand, A.A., Binley, A., Nielsen, E., Effersø, F., Christensen, N.B., Sørensen, K.I., Foged, N. & Vignoli, G. 2014. An overview of a highly versatile forward and stable inverse algorithm for airborne, ground-based and borehole electromagnetic and electric data. *Explor. Geophys*, 1-13.

Blundell, K. 2012. Deering Hills Project November 2011 TEM Survey Valen Model Summary. pp. 1. Musgrave Minerals.

Constable, S.C. & Weiss, C.J. 2006. Mapping thin resistors and hydrocarbons with marine EM methods: Insights from 1D modeling. *Geophysics* **71**, G43-G51.

Dorn, O. & Lesselier, D. 2006. Level set methods for inverse scattering. *Inverse Problems* **22**, R67.

Dorn, O., Miller, E.L. & Rappaport, C.M. 2000. A shape reconstruction method for electromagnetic tomography using adjoint fields and level sets. *Inverse Problems* **16**, 1119.

Duncan, A. 1987. Interpretation of down-hole transient EM data using current filaments. *Exploration Geophysics* **18**, 36-39.

Eadie, T. & Prikhodko, A. 2013. VTEM - SKYTEM SURVEY COMPARISON OVER VALEN CU-NI DEPOSIT. Geotech Ltd.

Effersø, F., Auken, E. & Sørensen, K.I. 1999. Inversion of band-limited TEM responses. *Geophysical Prospecting* **47**, 551-564.

Effersø, F. & Sørensen, K.I. 2013. SkyTEM Case Study: The Valen Survey Comparison with VTEM. SkyTEM Surveys.

Fainberg, E., Pankratov, O. & Singer, B.S. 1993. Thin sheet modelling of subsurface and deep inhomogeneities. *Geophysical Journal International* **113**, 144-154.

Fitterman, D.V. & Stewart, M.T. 1986. Transient electromagnetic sounding for groundwater. *Geophysics* **51**, 995-1005.

Johansen, H.K. & Sørensen, K.I. 1979. Fast Hankel transforms. *Geophysical Prospecting* **27**, 876-901.

Lajoie, J.J. & West, G. 1976. The electromagnetic response of a conductive inhomogeneity in a layered earth. *Geophysics* **41**, 1133-1156.

Macnae, J., King, A., Stolz, N., Osmakoff, A. & Blaha, A. 1998. Fast AEM data processing and inversion. *Exploration Geophysics* **29**, 163-169.

McMillan, M.S., Schwarzbach, C., Haber, E. & Oldenburg, D.W. 2015. 3D parametric hybrid inversion of time-domain airborne electromagnetic data. *Geophysics* **80**, K25-K36.

Panourgias, I. 2011. NUMA effects on multicore, multi socket systems. *The University of Edinburgh*.

Price, A.T. 1948. The induction of electric currents in non/uniform thin sheets and shells.

Raiche, A. 1998. Modelling the time-domain response of AEM systems. *Exploration Geophysics* **29**, 103-106.

Reid, J., Fitzpatrick, A. & Godber, K. 2010. An overview of the SkyTEM airborne EM system with Australian examples. *Preview* **2010**, 26-37.

Song, Y., Kim, H.J. & Lee, K.H. 2002. An integral equation representation of wide-band electromagnetic scattering by thin sheets. *Geophysics* **67**, 746-754.

Swidinsky, A. & Edwards, R.N. 2010. The transient electromagnetic response of a resistive sheet: an extension to three dimensions. *Geophysical Journal International* **182**, 663-674.

Vasseur, G. & Weidelt, P. 1977. Bimodal electromagnetic induction in non-uniform thin sheets with an application to the northern Pyrenean induction anomaly. *Geophysical Journal International* **51**, 669-690.

Walker, P.W. & West, G.F. 1991. A robust integral equation solution for electromagnetic scattering by a thin plate in a conductive media. *Geophysics* **56**, 1140-1152.

Weidelt, P. 1981. Report on dipole induction by a thin plate in a conductive halfspace with an overburden.

Wolfgram, P., Hyde, M. & Thomsen, S. 1998. How to find localised conductors in GEOTEM data. *Exploration Geophysics*, 665-670.

Zhou, Q. 1989. Audio-frequency Electromagnetic Tomography for Reservoir Evaluation. PhD dissertation, Lawrence Berkeley Laboratory, University of California.

Appendix D

Paper 4

Submitted to Radio Science.

A novel approach to solving the quasi-static electromagnetic problem

Tue Boesen [1],Eldad Haber[2]

[1]Aarhus University, Denmark
[2]University of British Columbia, Canada

Key Points:

- Novel approach to the quasi-static Maxwell equation, using the spectral method.
- Founded on circulant matrices, which are natural representations of temporal periodicity.
- Gives the benefits of time domain propagation as well as frequency domain calculations.

Corresponding author: Tue Boesen, `tue@geo.au.dk`

Abstract

The quasi-static electromagnetic problem is commonly encountered in geophysics, and is of particular interest in near-surface exploration. We present a novel spectral approach to solving the quasi-static electromagnetic problem, commonly encountered in geophysics. Our solution naturally enables temporal periodicity, and decouples the equations for each timestep, making parallelization trivial, much like the well-known frequency domain approach. Unlike frequency domain propagation, our solution requires only one spectral response calculation for each timestep, and is in that sense similar to time domain propagation. We have successfully demonstrated our approach through synthetic studies with linear timestepping in 3D. Unfortunately, we have been unable to find a stable propagation approach in the general non-linear case. Presently it remains unclear to us whether a stable propagation method could exist, but we believe the method has potential, if a stable solution can be found, and as such we present our findings and experiences, and hope to inspire others to further investigate and advance the method.

1 Introduction

Electromagnetic (EM) methods are among the most vital methods when doing near-surface geophysics. Within near-surface geophysics, the quasi-static approximation is commonly applicable and widely used (*Haber*, 2014). There are commonly two ways of solving the quasi-static maxwell equation, either directly in time domain, or in frequency domain with a transformation back to time domain at the end. In EM measurements signal-to-noise ratio is a large concern, which is usually handled by stacking data through repeated measurements. This stacking is generally repeated with a sufficiently high frequency that electromagnetic remnants from the previous measurements are present in the current measurement. These stackings give rise to temporal periodic boundaries, which can be approximated directly in the time domain, by propagating through several initiating cycles. However a smarter and more common way to compensate for these remnants, is to include one or more previous cycles in the waveform deconvolution (*Raiche*, 1987).

The typical goal of geophysical EM modelling is to find the time evolution of the EM field. This is done straight-forward in time domain, where the timesteps are chosen such that they directly propagate the EM field through times of interest. The number of timesteps needed depends on the earliest and latest time-gate of interest. The main drawback with doing propagation in time domain is that the calculation of the timesteps has to happen sequentially, which means that parallelization of the EM problem in time domain becomes non-trivial, and with a sub-optimal scaling (*Lions*, 2001). On modern hardware this can become a serious issue, since the exponential growth in computer power have largely been in the area of parallelization within the last decade, and is likely to remain so in the foreseeable future (*Rauber and Rünger*, 2013; *Satish et al.*, 2015).

The usual alternative to time domain propagation, is frequency domain methods, where Maxwell's equations are recast into frequency domain. When recasting Maxwells equation into frequency domain, a time periodic EM field is assumed. This transforms the time differential operations into purely algebraic relations, which have several desirable properties in comparison (*Zhdanov*, 2009). The cost of this approach comes when transforming back to time-domain, since such a transformation typically needs ~100 frequencies to be calculated in order for the transformation back to time domain to be sufficiently accurate (*Börner et al.*, 2015). Roughly speaking the frequency domain approach, spectrally transforms the sequential time-step calculations into decoupled frequency response calculations, with the price that significantly more frequency responses are usually required to be calculated, than the number of time-steps.

In this paper we propose a novel approach to handling Maxwells equation, which will be referred to as spectral-time approach. Our method is, like frequency domain approaches, based on the spectral method. But unlike frequency domain methods, which requires up-

wards to 100 spectral responses in order to achieve an accurate transformation back to the time domain, the spectral-time method requires exactly one spectral response to be calculated for each timestep. Thus the spectral-time method typically involves significantly fewer spectral responses, than frequency domain methods, while retaining several of the key benefits commonly associated with frequency domain methods: The spectral-time approach still decouples the equations for each timestep, which makes parallelization trivial, and furthermore it gives the option of using temporal periodic boundaries. The spectral-time method is inspired by the mathematical framework surrounding circulant matrices (*Gray et al.*, 2006), which are matrices with properties that makes them natural representations of propagation schemes with periodic boundaries. Though the concept of circulant matrices is very general, and could no doubt be used in a wide variety of fields, the only area, we have been able to find, which utilize circulant matrices is digital image processing (*Hansen et al.*, 2006), where they are used in image restoration, and are useful because of their analytic properties.

Even though the spectral-time method is inspired by circulant matrices, the theory itself is not restricted to circulant matrices, but remains valid for a much broader class of propagation matrices. In the following, we demonstrate succesfully how spectral-time method can be used on temporal periodic systems with linear timestepping. Furthermore, we show how the theory is extended beyond circulant matrices on non-linear timestepping. Unfortuntely, in this general extended case, numerical instabilities are encountered, which we have been unable to circumvent. All our simulations are done in 3D, using a 3D Octree code (*Haber and Heldmann*, 2007).

2 Theory

In time domain the quasi-static electric field can be written as (*Ward and Hohmann*, 1988, p. 126):

$$\sigma \frac{\partial E}{\partial t} + \nabla \times \mu^{-1} \nabla \times E = -\frac{\partial S}{\partial t}, \tag{1}$$

where E is the electric field in time domain, σ is the conductivity, μ is the magnetic permeability, and S is the source-term. For brevity, let K be the curl-curl operator, given as:

$$K = \nabla \times \mu^{-1} \nabla \times, \tag{2}$$

and thus equation 1 can be rewritten as:

$$\sigma \frac{\partial E}{\partial t} + KE = -\frac{\partial S}{\partial t}. \tag{3}$$

We bring this from the continuous space to a discretized space in both space and time. Let $\boldsymbol{E}$ be the discretized version of the continuous field E, with n spatial points and m temporal points. Thus:

$$\boldsymbol{E} = [\boldsymbol{e}_1, \boldsymbol{e}_2, ..., \boldsymbol{e}_m], \tag{4}$$

where $\boldsymbol{e}_i$ is the discrete spacial electric field at the i'th timestep.

By using a finite difference approximation to the time differential, equation 3 can be rewritten in the discretized space as:

$$\boldsymbol{M_\sigma E D} + \boldsymbol{K E} = -\boldsymbol{S D}, \tag{5}$$

where $\boldsymbol{M_\sigma}$,$\boldsymbol{E}$,$\boldsymbol{K}$,$\boldsymbol{S}$ are discretized version of their continium variables, and $\boldsymbol{D}$ is a diagonalizable matrix that applies a finite difference differential to the left.

Since $\boldsymbol{D}$ is assumed diagonalizable, we can do an eigendecomposition of $\boldsymbol{D}$:

$$\boldsymbol{D} = \boldsymbol{V \Lambda V}^{-1}. \tag{6}$$

Using the eigendecomposition of $\boldsymbol{D}$, equation 5 can be rewritten as:

$$\boldsymbol{M_\sigma E V \Lambda} + \boldsymbol{K E V} = -\boldsymbol{S V \Lambda}. \tag{7}$$

By transforming the Electric field and source term equation 7 can be rewritten as:

$$\boldsymbol{M_\sigma}\bar{\boldsymbol{E}}\boldsymbol{\Lambda} + \boldsymbol{K}\bar{\boldsymbol{E}} = -\bar{\boldsymbol{S}}\boldsymbol{\Lambda}, \tag{8}$$

where

$$\bar{\boldsymbol{E}} = \boldsymbol{E}\boldsymbol{V}, \tag{9}$$

and

$$\bar{\boldsymbol{S}} = \boldsymbol{S}\boldsymbol{V}. \tag{10}$$

Since $\boldsymbol{\Lambda}$ is diagonal, equation 8 is essentially decoupled for each timestep. In order to highlight this decoupling, the i'th timestep can be written as:

$$(\lambda_i \boldsymbol{M_\sigma} + \boldsymbol{K})\bar{\boldsymbol{e}}_i = -\lambda_i \bar{\boldsymbol{s}}_i, \tag{11}$$

where λ_i is the i'th diagonal element in $\boldsymbol{\Lambda}$.

Equation 11 highlights how the transformed electric field given in equation 9 is decoupled from all other timesteps and can easily be solved in parallel. For each timestep equation 11 forms a linear system of equations, which can be solved by either a direct sparse linear solver or an iterative linear solver. One caveat compared to direct propagation in time domain, is that matrix factorization is non-reusable, since the matrix will in general change for each timestep, due to its dependence on the eigenvalues λ_i, this makes sparse iterative solvers more attractive with this method. Once the transformed electric field is solved for all timesteps, the field is transformed back to timedomain, by multiplication with V^{-1} from the right.

D - the differential decomposition

$\boldsymbol{D}$ can be any diagonalizable matrix representation of a finite difference differential, though as noted in *Haber* (2014, p. 22) not all representations are desirable due to their non-trivial null-spaces. In this article several different differential propagation schemes are explored. We start by using the first order Backward differential formula (BDF1) to illustrate how the equations will look (*Ascher and Petzold*, 1998), as well as to highlight certain key aspects when creating an appropriate $\boldsymbol{D}$.

Linear timesteps - analytic solution

Assuming linear timesteps, and temporal periodic boundaries, then for a BDF1 propagation scheme $\boldsymbol{D}$ will be of the following form:

$$\boldsymbol{D} = \frac{1}{\Delta t}\begin{pmatrix} 1 & -1 & & & \\ & 1 & -1 & & \\ & & \ddots & \ddots & \\ & & & 1 & -1 \\ -1 & & & & 1 \end{pmatrix}, \tag{12}$$

where Δt is the constant timestep length. Multiplying this from the right on $\boldsymbol{E}$ gives:

$$\boldsymbol{E}\boldsymbol{D} = \frac{1}{\Delta t}\left[(\boldsymbol{e}_1 - \boldsymbol{e}_m), (\boldsymbol{e}_2 - \boldsymbol{e}_1), \ldots, (\boldsymbol{e}_m - \boldsymbol{e}_{m-1})\right], \tag{13}$$

which is exactly a finite difference approximation, with temporal periodic boundaries. $\boldsymbol{D}$ is a circulant matrix, and thus analytical solutions to the eigendecomposition $\boldsymbol{D} = \boldsymbol{V}\boldsymbol{\Lambda}\boldsymbol{V}^{-1}$ exists (*Gray et al.*, 2006). The eigenvector matrix is given as:

$$\boldsymbol{V} = \begin{pmatrix} e^{i2\pi/m} & e^{i4\pi/m} & \cdots & e^{i2\pi} \\ e^{i4\pi/m} & e^{i8\pi/m} & & \vdots \\ \vdots & & \ddots & \\ e^{i2\pi} & & & e^{im2\pi} \end{pmatrix}, \tag{14}$$

and the eigenvalue matrix is given as:

$$\boldsymbol{\Lambda} = \begin{pmatrix} 1 - e^{i2\pi/m} & & & \\ & 1 - e^{i4\pi/m} & & \\ & & \ddots & \\ & & & 1 - e^{i2\pi} \end{pmatrix}. \tag{15}$$

Note that the last eigenvalue in this case is 0. And in fact it can be shown that for any periodic differential matrix $\boldsymbol{D}$, one eigenvalue will always be zero.

Varying timesteps - general solution

In the general case where the timesteps are non-linear, a general expression for $\boldsymbol{D}$ using the BDF1 propagation scheme can be written as:

$$\boldsymbol{D} = \begin{pmatrix} \eta_1 & -\eta_1 & & & \\ & \eta_2 & -\eta_2 & & \\ & & \ddots & \ddots & \\ & & & \eta_{nt-1} & -\eta_{nt-1} \\ -\eta_{nt} & & & & \eta_{nt} \end{pmatrix}, \tag{16}$$

where η_i is the reciprocal timestep, $\eta_i = \frac{1}{\Delta t_i}$. In this general case, $\boldsymbol{D}$ is no longer a circulant matrix, and an analytical expression for the eigendecomposition is not known, and thus numerical methods have to be used.

A subtle yet important caveat when choosing how to create $\boldsymbol{D}$ is that in all the cases we have explored, the corresponding eigenvector matrix $\boldsymbol{V}$ will be nearly singular, and hence $\boldsymbol{V}^{-1}$ is not well defined, which is needed to retrieve the electric field in time domain, see equation 9. Exactly how close to singular the eigenvector matrix ends up being, is largely dependent on the timesteps chosen. Unfortunately, as will be shown in the following, we have been unable to find a propagation scheme that produces stable solutions in the case of non-linear timestepping.

3 Data and Results

Numerical tests of the spectral method were conducted using a 3D octree code based on the work done in *Haber and Heldmann* (2007), and currently incorporated in the open source framework called jInv (*Ruthotto et al.*, 2016). Our modelling setup consists of: a 100 Ω m halfspace, with a 10 m x 10 m square transmitter loop, placed on a flat surface, which emits an impulse response at t =60 µs and every 300 µs thereafter. Two y-directed electric dipole receivers are placed along the x-axis; a close receiver at 50 m from the center of the transmitter, and a remote receiver placed 400 m from the center. Additional tests were performed on more complicated systems, which showed similar results (not shown).

Validation against time domain propagation

A comparison between the spectral method and propagation in time domain was conducted. The comparison was done both to confirm convergence between the two methods, but also to investigate the number of cycles needed for a time domain propagation to converge to the periodic solution provided by the spectral method. In this case the direction of the current is changed between each consecutive pulse, in order to minimize the build-up residual currents in the ground, as is commonly done in actual field measurements.

Figure 1 shows a comparison for the; first-, second-, and fifth-cycle. (A,B) Shows the field and deviation in the remote receiver, while (C) shows the deviation for the close receiver. For a close receiver only 1-2 initiating cycles are needed for a deviation of less than

1 %, but for the remote receiver around ∼ 5 cycles are needed in order to reach the same level of accuracy.

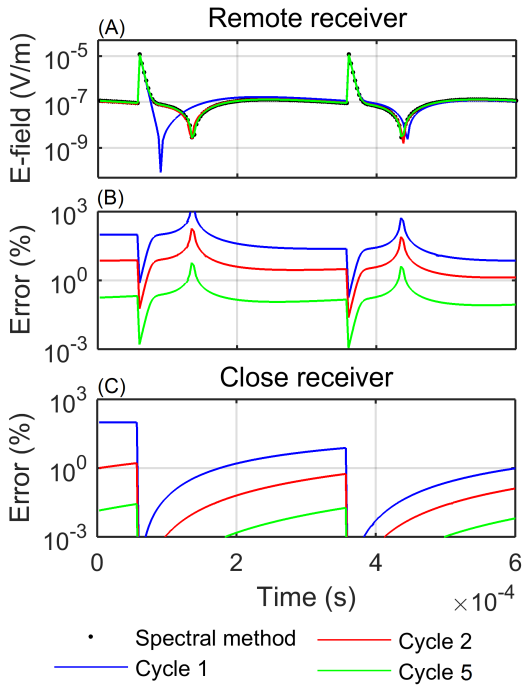

Figure 1. Compares the electric field generated by the spectral method using temporal periodic boundaries, with the field from a similar periodic pulse propagated in time domain. In the figure, the: first, second, and fifth cycle of the time domain propagation are shown. (A) Shows the magnitude of the electric field in the remote receiver. (B) Shows the deviation between the spectral response and different cycles of the time domain propagated pulse for the remote receiver. (C) Shows the deviation between the spectral response and different cycles of the time domain propagated pulse for the close receiver.

The number of cycles needed for convergence between the methods should be considered in two ways. From a numerical modelling perspective, the number of cycles indicates how expensive it is to use time domain propagation to simulate temporal periodic systems. From a physical perspective, the number of cycles represents the number of repeated measurements needed in an area in order to reach a temporal periodic steady state. As expected time propagation converges to the same response as the spectral-time method, given enough cycles.

Number of timesteps

In the previous, a simulation with 150 timesteps showed that time domain propagation converges to the spectral-time method given enough cycles. Figure 2 shows a comparison between the responses from the 5'th cycle using time domain propagation and the spectral-time method, for various numbers of timesteps. From this it is concluded that the two methods converge irregardless of the number of timesteps used.

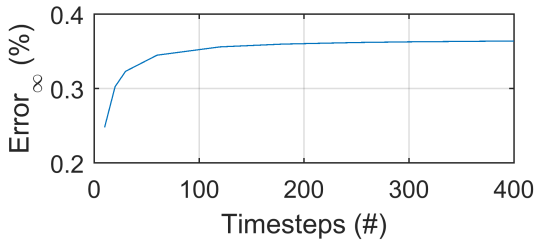

Figure 2. Shows the infinity norm deviation between the 5'th cycle of a time domain propagation and the spectral method, as a function of the number of timesteps. The deviation is shown for the close receiver.

Non-linear BDF1 timestepping

The fact that spectral-time propagation is stable and accurate with linear timestepping, can be usefull in various cases. However, in order for the method to have general applicability, and be a contender to the already well-established methods, non-linear timestepping is needed. Unfortunately, BDF1 appears unstable when moving beyond linear timestepping, due to the numerical singularity of its corresponding eigenvector-matrix. This instability with BDF1 happens both for logspaced timesteps and for combinations of different constant length timesteps as seen in Figure 3.

Alternative propagation methods

Since BDF1 proved numerically unstable for non-linear timestepping, alternative propagation methods are explored. Figure 4 shows a linear timestepping comparison of: BDF1, BDF2, BDF3, and first order central differences (CD1). CD1 methods can in some cases produce artificial oscillations (*Ewing and Wang*, 2001), which stems from the methods non-trivial nullspace. While the artificial oscillations are problematic, they could be suppressed by introducing a smoothening filter, as done in computational fluid dynamic (*Shyy et al.*, 1992). More problematic is the fact that the CD1 solution, produces a solution which appears time-symmetric, this is decidedly different from how such a solution should appear. BDF2 and BDF3 produces solutions more akin to BDF1, but still with a less than satisfactory deviation from BDF1. So unfortunately neither: BDF2, BDF3, or CD1 produced satisfactory solutions when doing linear timestepping, and hence there is no reason to explore their stability further in the general non-linear case.

4 Discussion & Conclusion

We have presented a novel approach for solving the quasi-static electromagnetic problem commonly used in geophysical EM methods with temporal periodicity. The spectral-time method naturally enables temporal periodicity, it decouples the equation for each timestep, and only requires one spectral response calculation for each timestep. For linear timestepping, we have shown that propagation in time domain converges to the spectral-time method, when using BDF1 propagation. For non-linear timestepping, numerical instabilities are encountered in the eigendecomposition of the BDF1 differential matrix operator. We sought to circumvent this instability by using alternative propagation schemes, but BDF2, BDF3, and CD1 have all failed to produce satisfactory results in the case of linear timestepping. At this point it seems prevalent to ask whether this is an inherent instability for any periodic differential matrix. Unfortunately, we have thus far been unable to answer this question, and now turn to the scientific community in the hope that others can use or further advance the spectral-time method, which we believe have great potential, if a stable general propagation method could be found.

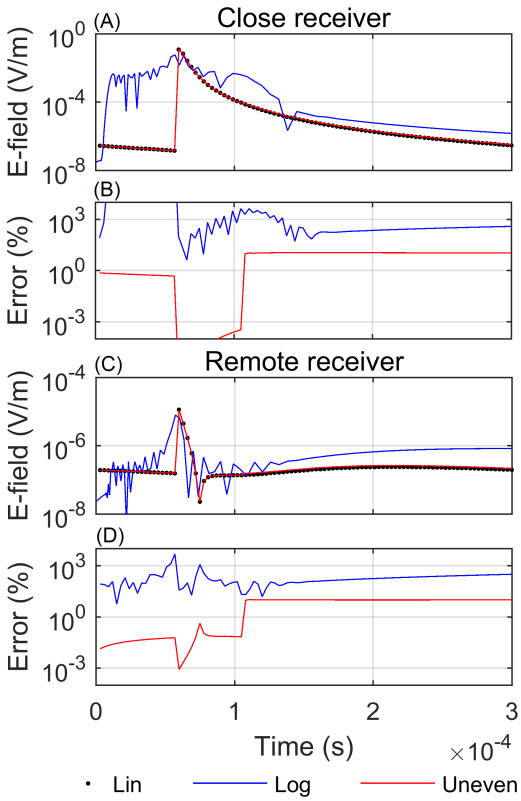

Figure 3. Shows a comparison between: linear-, logspaced-, and uneven-timestepping. The uneven timestepping, performs linear timestepping until $t = 105\,\mu s$ at which point the timestepping size, Δt, is increased by 10 %. (A) Shows the electric fields in the close receiver, (B) shows the corresponding deviation from linear timestepping. (C) Shows the electric fields in the remote receiver, (D) shows the corresponding deviation from linear timestepping.

Acknowledgments

This study was supported by Innovation fund Denmark, through the AirTech4Water project.

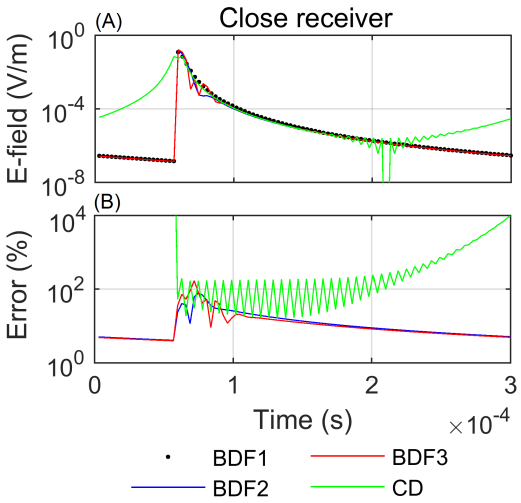

Figure 4. Four different propagation schemes are compared for linear timestepping. (A) Shows the electric field, while (B) shows the deviation between BDF1 and the other propagation methods.

References

Ascher, U. M., and L. R. Petzold (1998), *Computer methods for ordinary differential equations and differential-algebraic equations*, vol. 61, Siam.

Börner, R.-U., O. G. Ernst, and S. Güttel (2015), Three-dimensional transient electromagnetic modelling using rational krylov methods, *Geophysical Journal International*, *202*(3), 2025–2043.

Ewing, R. E., and H. Wang (2001), A summary of numerical methods for time-dependent advection-dominated partial differential equations, *Journal of Computational and Applied Mathematics*, *128*(1), 423–445.

Gray, R. M., et al. (2006), Toeplitz and circulant matrices: A review, *Foundations and Trends® in Communications and Information Theory*, *2*(3), 155–239.

Haber, E. (2014), *Computational methods in geophysical electromagnetics*, vol. 1, SIAM.

Haber, E., and S. Heldmann (2007), An octree multigrid method for quasi-static maxwellâĂŹs equations with highly discontinuous coefficients, *Journal of Computational Physics*, *223*(2), 783–796.

Hansen, P. C., J. G. Nagy, and D. P. O'leary (2006), *Deblurring images: matrices, spectra, and filtering*, vol. 3, Siam.

Lions, J. (2001), Résolution d'edp par un schéma en temps «pararéel» a"parareal"in time discretization of pde's, *Academie des Sciences Paris Comptes Rendus Serie Sciences Mathematiques*, *332*, 661–668.

Raiche, A. (1987), Transient electromagnetic field computations for polygonal loops on layered earths, *Geophysics*, *52*(6), 785–793.

Rauber, T., and G. Rünger (2013), *Parallel programming: For multicore and cluster systems*, Springer Science & Business Media.

Ruthotto, L., E. Treister, and E. Haber (2016), jinv–a flexible julia package for pde parameter estimation, *arXiv preprint arXiv:1606.07399*.

Satish, N., C. Kim, J. Chhugani, H. Saito, R. Krishnaiyer, M. Smelyanskiy, M. Girkar, and P. Dubey (2015), Can traditional programming bridge the ninja performance gap for parallel computing applications?, *Communications of the ACM*, *58*(5), 77–86.

Shyy, W., M.-H. Chen, R. Mittal, and H. Udaykumar (1992), On the suppression of numerical oscillations using a non-linear filter, *Journal of Computational Physics*, *102*(1), 49–62.

Ward, S. H., and G. W. Hohmann (1988), Electromagnetic theory for geophysical applications, in *Electromagnetic methods in applied geophysics*, vol. 1, pp. 131–311.

Zhdanov, M. S. (2009), *Geophysical electromagnetic theory and methods*, vol. 43, Elsevier.

Appendix E

Technical Report

Available at http://hgg.au.dk/publications/reports/.

Numerical tools and optimizations for EM geophysical methods

Tue Boesen[1,*]

[1] *Aarhus University, Denmark*

(Dated: October 30, 2017)

* tue@geo.au.dk

PRETEXT

This technical report was prepared, in order to document work I had done during my PhD studies, which did not make it into any publications, but was nevertheless deemed important and of relevance to others in the scientific community. For PhD purposes it should be stated that: the parallelization framework is essentially created solely by me, with the exception of the hardware detection algorithm, which was made before I started my PhD. The iterative solver already existed in a serial form before I arrived. Under guidance from my first co-supervisor Casper Kirkegaard, I created the new iterative solver, based on some of the old elements and many new elements.

CONTENTS

Pretext i

Introduction 1

Parallelism 1
- Goals for our parallelization framework 2
- A general parallelization framework 3
- Limitations and caveats 3

Sparse linear solvers 3
- Direct solvers 4
- Iterative solvers 4
- Propagation methods 4
- Preconditioners 4
- Block parallelism 6
- Our iterative sparse linear solver 7
- Solver performance 7
- Limitations and caveats 8

Results and conclusion 9

Acknowledgements 9

References 10

INTRODUCTION

Numerical modelling is becoming an increasingly important tool for any scientist, and the continued exponential growth in computational power enables the possibility of ever more realistic and powerful simulations.

Before multicore CPU's became common, around 2005, optimizing numerical code largely meant to make sure that the algorithm was mathematical optimal, while tricks that required in-depth hardware knowledge like: the number of clock cycles various mathematical operations take, or how to minimize cache misses, rarely meant more than a speedup factor of ∼10x. Moreover, before 2005, CPU advancements largely happened through faster clock frequencies. Thus, old code could more or less run optimally on a new CPU without any modifications. Today this is no longer so. Since the introduction of the multicore CPU, processor advancements have largely happened through parallelization and vectorization. To the point where old serial code that does not use either of these advancements can easily loose out a computational speedup of ∼50x or even upwards of ∼500x on a modern CPU designed for heavy computational use (Sodani et al. 2016). In this context, it is important to note that this speedup is on top of the ∼10x speedup previously mentioned.

While vectorization is often partially utilized implicitly by compilers, a conscious effort requiring intrinsic knowledge is generally required in order to design algorithms that can run optimally on modern hardware. Most scientist are experts in their own field, but lack the in-depth hardware knowledge required to design optimal algorithms. Because of this, it is imperative that general heavily optimized numerical algorithms are designed, and made available for the advancement of scientific modelling. BLAS and LAPACK, (Anderson et al. 1999), are perhaps the most well-known examples of such tools. In the following, I will present the various parallelization methods commonly used, explain why we chose OpenMP parallelization in AarhusInv (Auken et al. 2014). Following this, I will discuss the various issues this lead to in our code, and how we solved these by developing a general parallelization framework, designed for portability and a wide range of users. Building on top of this framework, I present our highly optimized iterative sparse linear solver, which is able to achieve super-linear scaling on the linear systems we arrive at in geophysical EM inversions. Both of these tools are freely available for academic purposes and can be obtained by contacting the HydroGeophysics Group at Aarhus University.

PARALLELISM

Parallelizing generally exist at three different levels. The highest level of parallelization is between different systems in a distributed memory environment, where the environment can be either a cluster or a grid. In both cases the system consist of separate systems, which communicate through a network, typically with message passing interface (MPI) (Gropp et al. 1999). If a problem needs a lot of computational power, then clusters with MPI are generally the only way to achieve it, since any number of systems can be combined to make an almost arbitrarily powerful cluster/grid. However, most programs do not require a supercomputer to run on, and since a single modern computer can reach more than 3 TFLOPS of performance, this is sufficient for solving many problems, provided the compute power can be used efficiently. The next level of parallelization is task parallelization on the processing unit. CPU task parallelization commonly occurs with OpenMP directives (Dagum and Menon 1998), while GPU task parallelization can be done with CUDA directives (Nickolls et al. 2008). The final level of parallelization happens inside individual cores, and is commonly referred to as vectorization. Vectorization is largely done automatically by the compiler, though there can still be a significant performance boost if done manually, since automatic compiler vectorization has to be very safe and conservative. It is important to note that the different kinds of parallelization are not mutually exclusive, though combining all levels of parallelization can be a difficult task.

Our code does currently not use MPI programming, for which there are several reasons: One reason being that MPI programming requires a significant restructuring of the already existing code. Furthermore, MPI programming has a very large communication overhead and low communication bandwidth, which means that acceptable scaling, can often be hard to achieve. However, the main reason why MPI parallelization has not been implemented is that using a single computer system have thus far proven to be sufficient for the modelling we do. Instead, our code relies on CPU parallelization through OpenMP, and vectorization.

OpenMP parallelization was chosen because OpenMP directives are designed for gradual parallelization of existing sequential code, while GPU parallelization was disregarded since it is only suited for very narrow and extremely parallel jobs, and not for the multi-purpose modelling program we have. During the last 5 years, all the vital and

processor-heavy algorithms have been parallelized in AarhusInv. However, this parallelization did not come without issues. In the following, several issues will be highlighted that led to the creation of our general parallelization framework.

Portability

AarhusInv is intended to be used by many people, with various computer systems. Ideally, it should run optimally on all those systems, whether they are: NUMA or UMA systems (Panourgias 2011), contains 4 or 64 cores, has hyperthreading enabled, and whether it is a dedicated or shared machine.

Broad userbase

Our users range from novices to experts, with various desires for controlling how the code runs on their systems. As such, we ideally want a program which can run decent autonomously, but where the expert user still has full thread and affinity control, if desired.

Complex code

The code contains various different modelling schemes developed by many different people. Parts of the code use simple loop parallelization, others use more advanced nested parallelization. Furthermore, some parts can be memory bandwidth limited, and in such parts, it is advantageous to use fewer parallelization threads, in order to prevent bottleneck regions in the code. The result of this was that we had a wide variety of parallelization schemes, which all made sense in their individual cases, but collectively were hard to maintain. Furthermore, autonomous code becomes increasingly complex with the number of exceptions and special cases that needs to be accounted for.

Global directives

OpenMP calls are global directives, and setting them in one subroutine can affect code outside that subroutines scope. This led to unintended cross-modular behavior, especially when combined with the fact that developers often reuse - as they should, general subroutines from other parts of the code. Finally, it often resulted in people copying existing subroutines and changing the parallelization to fit their particular parallelization schemes, which makes maintenance of the code a nightmare.

Goals for our parallelization framework

Based on these issues, a set of goals were created that the framework should fulfil:

- Portability - make the code run optimally on various different systems and architectures (NUMA/UMA/Hyperthreading).
- Make the code run well on both shared and dedicated servers.
- Enable autonomous parallelization, as well full control for the expert user.
- Create a simple, yet general parallelization structure, which can contain all the previously used parallelization schemes.
- Create a single parallelization module, that contains all parallelization information, and does all the global OpenMP directives needed, such that the general developer should never set these global directives manually.

```
NCPUs                   !Total number of threads
NCPUsLow                !Total number of threads in a memory bandwidth limited region
AffinityMode            !Dedicated or shared server?
AffinityPattern         !Scattered or compact affinity?
StartThread             !ThreadID of first affinity binding
UseNested               !Use nested parallelization?
    NCPUOuter           !Only used if UseNested=1, Number of CPUs in first parallel region
```

TABLE I. The input parameters for the parallelization framework. Any of these parameters can be specified by the user to dictate how the parallelization should occur, or set to -99 to be automatically defined.

- Create a dynamic parallelization structure, which removes the need for having multiple copies of the same routines for various degrees of parallelization.

With these goals in mind, the following parallelization framework was created.

A general parallelization framework

The result of all this, is the following OpenMP parallelization framework created in Fortran, which fulfils all the goals previously listed. The parallelization framework can be obtained from the HydroGeophysics Group. The download contains the parallelization framework module, as well as a small example showing how to setup and use it.

In short the module contains an initialization routine, where the user can specify the parameters shown in Table I, however these parameters can also be set to -99, in which case the initialization routine will get hardware information from the system and set the parameters autonomously.

Once the initialization is done, any parallel region should be called with the StartOpenMP function, as demonstrated in the example. StartOpenMP will determine whether parallelization should occur at this point in the code, and how it should occur.

Limitations and caveats

This parallelization framework has been used for roughly a year in our code, so while it has been tested quite thoroughly, it is likely that some bugs still remain. The framework was created using OpenMP 4, which have limited directives for nested parallelization. In the future, it is possible that smarter or more optimal ways of building this framework will occur. For instance, current OpenMP versions does not support different affinity-settings for different levels of parallelization. Furthermore, the framework only support two layers of nested parallelization, since our code has never needed more than two layers at any point. Though extending the code to more layers is fairly simple.

Finally, it should be noted that the framework only works for windows machines, and while most functions can be used directly on other systems, the automatic hardware determination will likely need to be completely rewritten.

SPARSE LINEAR SOLVERS

Let A be a $n \times n$ matrix, and b a $n-$vector, a commonly encountered problem in numerical modelling, is then to find the $n-$vector x that solves the linear system:

$$Ax = b. \tag{1}$$

Linear systems are generally easy to solve, and many efficient tools exists for this singular purpose. However, if the linear systems become sparse and large, then solving them efficiently often becomes a non-trivial issue.

The methods for solving sparse linear systems are generally split in two categories: direct solvers, and iterative solvers. While favor seems to have shifted towards direct solvers within the last decade in the EM geophysics community, both methods have their strengths and weaknesses, as will be discussed in the following.

Direct solvers

Direct solvers do a full factorization of the system matrix, which can take quite a while, and use a lot of memory. However, once such a factorization is done, the system can efficiently be solved for any number of right-hand sides. For direct solvers there exist a number of ready-made libraries. This makes using direct solvers relatively straightforward. Amestoy et al. (2001) introduced the direct solver named MUMPS, which is fully parallelized using the MPI-interface, and thus making it capable of operating in parallel on a cluster. Schenk et al. (2000) introduced the direct solver used in the Pardiso library, which is parallelized using the OpenMP interface, and thus making it capable of running in parallel on a single computer. MUMPS and Pardiso are currently two state of the art direct solvers, and which should be employed, depends on the level of parallelization desired. A slightly outdated comparison of direct solvers can be found in Gould et al. (2007). The biggest problem with direct solvers is the fact that they are neither capable, nor efficient, at handling very large linear systems. This is because, even though the system matrix might be extremely sparse, there is no guarantee that the factorization matrix will remain sparse. A memory consumption of 10-40 times that of the original matrix is not unheard of (Rücker et al. 2006).

Iterative solvers

Iterative solvers use either no factorization, or at most an incomplete factorization, followed by multiple forward- and backward-substitutions, in order to iteratively converge towards a solution to the linear system. Unlike direct solvers, there exists no efficient, and ready to use library, for parallel iterative solvers, that I am currently aware of. The main reason for this is probably that, there exists many different algorithms, and which one is superior is heavily system dependent (Ern et al. 1994, Nachtigal et al. 1992). Oldenburg et al. (2012) compares the use of direct and iterative solvers for the case of 3D EM forward modelling, and conclude that direct solvers are favorable for these kinds of problems. While this might indeed be the case, my personal experience with iterative solvers, suggests that the computational times shown in Oldenburg et al. (2012) for iterative solvers can be improved significantly by applying more optimal preconditioners, and thus the question of which method is superior remains.

Building an iterative solver is a matter of choosing an appropriate propagation method as well as good preconditioners, in the following I will go through our iterative linear solver.

Propagation methods

The first thing needed to iteratively solve a linear system is a propagation method. The number of propagation methods spread throughout literature can seem overwhelming, though Saad (2003) contains the most common algorithms used for iteratively solving sparse linear systems. In our solver we use conjugate-gradient (CG) (Hestenes and Stiefel 1952), which is known for its stability and widely used in our field of science (Brodie and Sambridge 2006, Kirkegaard and Auken 2015, Wu 2003). CG is valid for real positive definite systems, and is known for being very fast and stable.

Preconditioners

A preconditioner is essentially any transform to the linear system, before or during the propagation, such that the solution space becomes easier to probe iteratively. Experience within the iterative linear solving community have shown that proper preconditioning is of vital importance, since this to a large extent determines: memory requirements, solution time, and stability of the solver (Saad and van der Vorst 2000). Preconditioning generally comes in two forms when solving sparse linear systems. It can either be an initial preconditioner, which is applied before using any iterative solver. In that case, the job of the preconditioner is to be an inexpensive operation that either approximate the inverse of A or in some other way transforms A, such that the linear system becomes easier to iteratively solve.

The other kind of preconditioner is applied iteratively, while using the propagation method. Mathematically the job of such a preconditioner is to transform the eigenvalue distribution of the linear system, since the smaller the ratio

between largest and smallest eigenvalue is, the faster the system will in general converge.

In our linear solver, we currently use both kinds of preconditioners.

Initial preconditioners

The first preconditioner, which we always use is a reverse Cuthill-Mckee (RCM) reordering algorithm (Cuthill and McKee 1969), which is used before applying the iterative propagation method. In our particular case, the reordering is not done explicitly, but rather implicitly when the matrix for the linear system is first created, as detailed in Kirkegaard and Auken (2015). This is highly beneficial for several reasons. First, reordering algorithms are generally rather expensive, however this way the reordering is done only once, and only on the soundings which the linear system is based on. Since the soundings constitute a much smaller system, than the actual linear system used during a geophysical inversion, the compute time for the reordering becomes negligible in our case. Secondly, because the reordering is done on the soundings, it preserves the sounding integrity, which is crucial for the block splitting done during the parallelization of our iterative linear solver, as detailed later.

A reordering of the linear system is essential for two reasons. The first reason is that incomplete Cholesky (IC) factorization, which is one of our other preconditioners, only works well if the number of relevant elements in the factorization matrix is relatively evenly distributed among the different rows. Without reordering this is not so, and thus IC factorization would perform very poorly as a preconditioner (Kirkegaard and Auken 2015). The second reason why a reordering algorithm is crucial is due to the block parallelism, which we impose as a way of parallelizing the linear solver. In order for the block parallelism to be successful, it requires that no vital information is located far from the diagonal, which the RCM reordering algorithm helps ensure.

For completeness sake, the iterative solver includes an RCM reordering algorithm, however since the algorithm is not employed in our normal code it is neither parallelized nor optimized. A more effective RCM algorithm could likely be built based on the algorithm suggested in Karantasis et al. (2014).

Another initial preconditioning that we do is to normalize the diagonals of the matrix representing the linear system. This is done by letting D be the square root of the diagonal elements of A. The linear system is then transformed by multiplying equation 1 with D^{-1} from the left, which gives:

$$D^{-1}AD^{-1}Dx = D^{-1}b, \tag{2}$$

which can be rewritten as:

$$\tilde{A}\tilde{x} = \tilde{b}, \tag{3}$$

where $\tilde{A} = D^{-1}AD^{-1}$, $\tilde{x} = Dx$, and $\tilde{b} = D^{-1}b$. Thus all the diagonal elements become unity, which speeds up the iterative convergence significantly.

Iterative preconditioners

The other kind of preconditioners, are employed iteratively during the propagation. In our case, we have two iterative preconditioners, where we use either one or the other, depending on the difficulty of the linear system. The difficulty of a linear system is not something that is very well understood, however the diagonal dominance, d, is often used:

$$d = \min_{i=1}^{n} \frac{|A_{ii}|}{\sum_{j\neq i}^{m_i} |A_{ij}|} \tag{4}$$

where n is the number of rows in A, and m_i is the number of elements in the i'th row of A. The diagonal dominance gives an estimate of the size of the diagonal in comparison to the off-diagonal elements, which is related to the eigenvalue distribution through Gershgorin's theorem (Saad 2003, p. 117).

In our iterative solver we use the average diagonal dominance, $\bar{d}$, to determine which preconditioner to employ for a given linear system.

$$\bar{d} = \frac{1}{n}\sum_{i=1}^{n} \frac{|A_{ii}|}{\sum_{j\neq i}^{m_i} |A_{ij}|}, \tag{5}$$

For simple systems, a symmetric Gauss-Seidel preconditioner, M_{SGS} is utilized:

$$M_{SGS} = (D - E)D^{-1}(D - F), \tag{6}$$

where $A = D - E - F$, with D being the diagonal elements of A, E the strict lower triangular half, and F the strict upper triangular part. The good thing about using Gauss-Siedel methods is that no initial factorization is needed; instead the algorithm can be directly applied during the forward- and backward-substitution during the iterative propagation. This makes propagation using symmetric Gauss-Seidel preconditioning extremely fast, when only a few iterations are needed in order to reach convergence. Gauss-Seidel can be proven to converge, if the system is diagonally dominant (Bagnara 1995), but though convergence is assured Gauss-Seidel preconditioning converges poorly in many cases. Based on experience, we only use Gauss-Seidel preconditioning, when the average diagonally dominance is 10 or greater.

For more difficult linear systems, an IC factorization with dual dropping strategy is used as an iterative preconditioner (Saad 1994). The IC factorization computes a lower triangular matrix L and an upper triangular matrix U such that the matrix A can be factorized as:

$$A = LU + E \tag{7}$$

where E is an error matrix. The dual dropping strategy ensures that only the n largest elements of each row is kept, where n is an input parameter, and only if those elements are above a certain threshold value. Using these dropping criteria gives an upper bound on both the memory consumption of the factorization, as well as the time required to compute it. As previously mentioned, it is imperative for a successful IC factorization, that the elements are somewhat evenly distributed among the rows in the matrix. However, if this is the case, then the method can be very effective.

Block parallelism

Solving a linear system is inherently a sequential problem, and simple parallelization attempts generally scale poorly for dense linear systems. For sparse linear systems, it is however possible to get decent scaling, and in particular for the linear systems arising in EM geophysics, as will be shown.

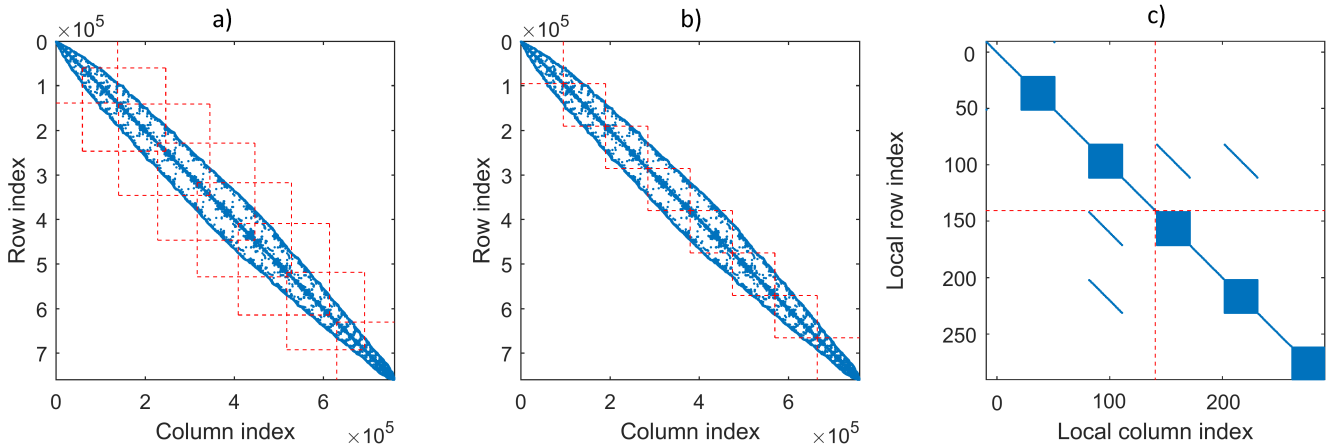

FIG. 1. Characteristic matrix sparsity pattern. Non-zero elements of the matrix are shown as blue dots, while the striped red lines indicate block-splitting boundaries. a) shows a block-splitting with overlap. b) shows a block-splitting without overlap, c) shows a zoom-in near a block boundary without overlap. The filled blue squares near the diagonal represent data from individual soundings, while the off-diagonal blue lines represent constraints between soundings.

Our parallelization method of the linear system consists of splitting the linear system into n or fewer blocks, where n is the number of parallel threads desired. In order for this to work, it is imperative that there are no significant elements

```
Example.f90            !Contains a small example, that initialize the parallelization, loads a matrix and
    solves the linear system
Solver.f90             !Contains the iterative sparse solver
SparseMatrix.f90       !Contains various sparse matrix functions needed by the iterative solver
Paralllelization.f90   !Contains the parallelization framework
Misc.f90               !Contains various small helping routines needed by the other modules
Load.f90               !Contains a minimalistic structure for loading the matrix, and setting the various
    settings for the example
RCM.f90                !Contains a RCM reordering algorithm
Quicksort.f90          !Contains a quicksorting algorithm used by the RCM module
Matrix.zip             !Contains a matrix saved in compressed sparse row format, as well as an ini file for
    running the example
Readme.txt             !Contains information needed for running the example
```

TABLE II. The files contained in the iterative solver, as well as an explanation of the various files.

in A far from the diagonal, which is one of the reasons why a RCM reordering was part of the preconditioning. Once the matrix has been reordered, the first version of our iterative solver used a blocksplitting algorithm that determined the max distance an element is placed from the diagonal and created overlapping blocks with this amount of overlap between each block, as shown in Figure 1 a). The overlap ensures that no information is lost during the parallel block propagation of the linear system. In practice, it turned out that this overlap was not needed, when solving the linear systems we encounter in EM, provided the soundings are RCM reordered. Thus, a much faster linear solver without overlap was created and used in the solver, see Figure 1 b). The reason why block-splitting without overlap works for our problems, is because all the vital information lies very close to the diagonal, while only non-vital information, about constraints between soundings, lie far away, see Figure 1 c). Note that in order for the non-overlapping block solver to be successful, it is imperative that the block-splitting is done such that no sounding information is split, thus sounding integrity has to be preserved, and splitting should only be done in-between soundings as shown in Figure 1 c).

With the above block-splitting, most of the difficulties about parallelizing the linear solver have been removed, especially in the non-overlapping case, where the large linear system essentially have been transformed to a series of smaller independent linear systems. However parallelized versions of both: CG, symmetric Gauss-Seidel and IC factorization still had to be made.

Our iterative sparse linear solver

The above solver was created, and can be obtained from the HydroGeophysics Group at Aarhus University. An overview of what is contained in the code can be seen in Table II. It should be noted that the solver operates on sparse matrices in compressed sparse row format.

Table III contains a holistic overview of how the iterative solver operates, written in pseudo-code.

Solver performance

Once the solver was completed, it was thoroughly validated and benchmarked with various linear systems relevant to us. Compared to our old code, the new parallel version was roughly ~ 35 times faster than our old code, which meant that the linear solver went from using roughly $\sim 50\%$ of the total computational time to $\sim 2-3\%$ of the computational time. These tests were of course dependent on both the geophysical system and numerical hardware. Furthermore, comparison with Pardiso was conducted, the results of which can be seen in Figure 2. Overall the results show that our solver performs rather poorly in comparison to Pardiso, at low levels of parallelization, but because of the superior scaling our iterative solver has, it outperforms Pardiso at high levels of parallelization. However, this comparison is not completely fair, since Pardiso does a zero order reordering before factorization, which does not scale well, while the matrices are already built in an optimal way that removes the need for reordering in the case of IC

```
[A,x,b] = RCM(A,x,b)           !RCM Reorder the linear system (note that this is done implicitly and on a
    sounding level in our code)
[A,x,b]=Normalize_diag(A,x,b)  !Normalize the diagonal elements of A and transform the system accordingly.
Blocksplitter(A)               !Split the linear system into blocks.
d=GetDiagDominance(A)          !Find the diagonal dominance of A, see eq 4
if d<Threshold then            !System not sufficiently diagonally dominant for Gauss-Seidel
  P=IC                         !Choose Incomplete Cholesky as preconditioner
  M=IC_Factorization(A)        !Compute Incomplete Cholesky factorization of each block
else
  P=SGS                         !Choose Symmetric Gauss-Seidel as preconditioner
end if
x=ApplyPropagation(A,x,b,P)    !Iteratively solve the full system using the appropriate block
    preconditioner.
```

TABLE III. Pseudo-code description of the iterative solver.

factorization. Nevertheless, the fact that the iterative solver is able to achieve super-linear scaling is noteworthy, but not unheard of in highly optimized code. The reason this is possible, is likely twofold. First, as the matrix is cut into smaller pieces, more of the non-essential constraints are removed from the preconditioner factorization, while this makes the factorization less accurate, it also makes it faster, since there are less elements to factorize and propagate. The second contributing factor to the super-linear scaling is the more standard reason, called the cache effect Eggers and Katz (1989). In short, every CPU has a cache associated with it (modern CPU's have several), the cache can be thought of as the CPU's local memory, and reading information from the cache is much faster than reading it from memory. However, the cache is very small, so it can only contain very limited information. Because of the limited cache storage, modern CPU's use advanced prediction algorithms to anticipate which information the CPU will need next from the cache. Whenever the information needed by the CPU is in the cache, it is called a cache hit, and otherwise a cache miss. The cache effect comes from having multiple threads working on similar data, if those threads happen to share the same cache, then what might have been a cache miss, if only one thread was employed, can become a cache hit when multiple threads are employed, since the relevant data was transferred to the cache for another thread.

As mentioned, the splitting of the linear system results in a less accurate preconditioning matrix, which can also be seen in Figure 2 c), where the number of propagation needed to reach convergence is shown to rise steadily with the number of threads, due to the rising inaccuracy in the preconditioner. It should be noted that the full matrix is still being solved, it is merely the preconditioning doing a slightly worse job at it, and thus additional propagations steps are required.

While the solver has been completely rebuilt, optimized, and parallelized, its compute time and memory consumption has previously been shown to scale linearly with the matrix size, and this is still true. Thus, the solver is capable of handling very large linear systems (Kirkegaard and Auken 2015). Successful tests have been performed on matrices as large as $\sim 6 \cdot 10^6$ rows/columns with $\sim 110 \cdot 10^6$ elements.

Limitations and caveats

The solver included here only covers positive definite matrix systems with real numbers. A complex and more general version which uses the BiCGStab routine was not included (van der Vorst 1992), since our code does not currently solve complex matrices, and thus the complex version has never been thoroughly tested.

The solver has primarily been tested on matrices created from 1D or 2D EM modelling, though a few tests have also been done on 3D modelling systems. While the dimensionality of the problem plays a role, the primary criteria for success is that, the sounding integrity is preserved and the data are structured using an RCM reordering algorithm. For problems outside EM modelling, it is likely that some of the parameters and thresholds need to be re-set in order to achieve optimal performance.

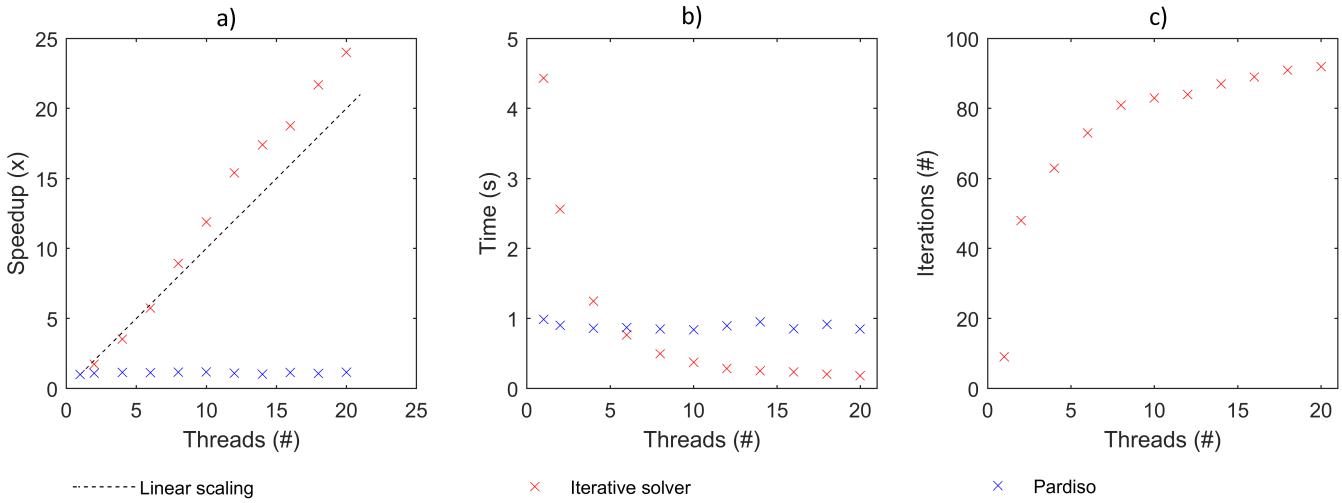

FIG. 2. Benchmarking the iterative solver, on a system with a matrix containing 42k rows and columns, with 500k elements. a) shows the speedup of the iterative solver and Pardiso. While the iterative solver reaches super-linear scaling, Pardiso scales very poorly. b) shows solving time as a function of threads. Pardiso is faster for low thread numbers, but because of its poor scaling the iterative solver out-scales it around six threads. c) shows the number of propagation required for the iterative solver to reach convergence as a function of threads.

RESULTS AND CONCLUSION

An easy to use, yet highly optimized, parallelization framework has been built. The framework can run autonomously or with simple user input. It furthermore removes the necessity of setting global OpenMP variables throughout the code, which is known to be a dangerous coding practice from the early days of coding where this was common practice. The parallelization framework follows best coding practices, and promotes a safer and more dynamic parallelization environment. The parallelization framework is also incorporated in the second coding example provided, which is a sparse iterative linear solver.

A sparse iterative linear solver, with super-linear scaling has been created. The solver is optimized for geophysical EM problems, which have been implicitly reordered using RCM, but should work well on many real positive definite sparse linear system. The solver is designed for modern multicore systems and relies on OpenMP parallelization. Because of the super-linear scaling, the solver outperforms the direct solver Pardiso when used on a modern system, and is capable of solving much larger systems than Pardiso.

ACKNOWLEDGEMENTS

Without Casper Kirkegaard to guide me and teach me the intricate ways of a computer, this report would not exist, so, Casper Kirkegaard, thank you very much.

Amestoy, P. R., Duff, I. S., L'Excellent, J.-Y., and Koster, J. (2001). A fully asynchronous multifrontal solver using distributed dynamic scheduling. *SIAM Journal on Matrix Analysis and Applications*, 23(1):15–41.

Anderson, E., Bai, Z., Bischof, C., Blackford, S., Demmel, J., Dongarra, J., Du Croz, J., Greenbaum, A., Hammarling, S., McKenney, A., and Sorensen, D. (1999). *LAPACK Users' Guide*. Society for Industrial and Applied Mathematics, Philadelphia, PA, third edition.

Auken, E., Christiansen, A. V., Kirkegaard, C., Fiandaca, G., Schamper, C., Behroozmand, A. A., Binley, A., Nielsen, E., Effersø, F., Christensen, N. B., et al. (2014). An overview of a highly versatile forward and stable inverse algorithm for airborne, ground-based and borehole electromagnetic and electric data. *Exploration Geophysics*, 46(3):223–235.

Bagnara, R. (1995). A unified proof for the convergence of jacobi and gauss–seidel methods. *SIAM review*, 37(1):93–97.

Brodie, R. and Sambridge, M. (2006). A holistic approach to inversion of frequency-domain airborne em data. *Geophysics*, 71(6):G301–G312.

Cuthill, E. and McKee, J. (1969). Reducing the bandwidth of sparse symmetric matrices. In *Proceedings of the 1969 24th national conference*, pages 157–172. ACM.

Dagum, L. and Menon, R. (1998). Openmp: an industry standard api for shared-memory programming. *IEEE computational science and engineering*, 5(1):46–55.

Eggers, S. J. and Katz, R. H. (1989). *The effect of sharing on the cache and bus performance of parallel programs*, volume 17. ACM.

Ern, A., Giovangigli, V., Keyes, D. E., and Smooke, M. D. (1994). Towards polyalgorithmic linear system solvers for nonlinear elliptic problems. *SIAM Journal on Scientific Computing*, 15(3):681–703.

Gould, N. I., Scott, J. A., and Hu, Y. (2007). A numerical evaluation of sparse direct solvers for the solution of large sparse symmetric linear systems of equations. *ACM Transactions on Mathematical Software (TOMS)*, 33(2):10.

Gropp, W., Lusk, E., and Skjellum, A. (1999). *Using MPI: portable parallel programming with the message-passing interface*, volume 1. MIT press.

Hestenes, M. R. and Stiefel, E. (1952). *Methods of conjugate gradients for solving linear systems*, volume 49. NBS.

Karantasis, K. I., Lenharth, A., Nguyen, D., Garzarán, M. J., and Pingali, K. (2014). Parallelization of reordering algorithms for bandwidth and wavefront reduction. In *Proceedings of the International Conference for High Performance Computing, Networking, Storage and Analysis*, pages 921–932. IEEE Press.

Kirkegaard, C. and Auken, E. (2015). A parallel, scalable and memory efficient inversion code for very large-scale airborne electromagnetics surveys. *Geophysical Prospecting*, 63(2):495–507.

Nachtigal, N. M., Reddy, S. C., and Trefethen, L. N. (1992). How fast are nonsymmetric matrix iterations? *SIAM Journal on Matrix Analysis and Applications*, 13(3):778–795.

Nickolls, J., Buck, I., Garland, M., and Skadron, K. (2008). Scalable parallel programming with cuda. *Queue*, 6(2):40–53.

Oldenburg, D. W., Haber, E., and Shekhtman, R. (2012). Three dimensional inversion of multisource time domain electromagnetic data. *Geophysics*, 78(1):E47–E57.

Panourgias, I. (2011). Numa effects on multicore, multi socket systems. *The University of Edinburgh*.

Rücker, C., Günther, T., and Spitzer, K. (2006). Three-dimensional modelling and inversion of dc resistivity data incorporating topographyi. modelling. *Geophysical Journal International*, 166(2):495–505.

Saad, Y. (1994). Ilut: A dual threshold incomplete lu factorization. *Numerical linear algebra with applications*, 1(4):387–402.

Saad, Y. (2003). *Iterative methods for sparse linear systems*. SIAM.

Saad, Y. and van der Vorst, H. A. (2000). Iterative solution of linear systems in the 20th century. *J. Comput. Appl. Math.*, 123(1-2):1–33.

Schenk, O., Gärtner, K., and Fichtner, W. (2000). Efficient sparse lu factorization with left-right looking strategy on shared memory multiprocessors. *BIT Numerical Mathematics*, 40(1):158–176.

Sodani, A., Gramunt, R., Corbal, J., Kim, H.-S., Vinod, K., Chinthamani, S., Hutsell, S., Agarwal, R., and Liu, Y.-C. (2016). Knights landing: Second-generation intel xeon phi product. *Ieee micro*, 36(2):34–46.

van der Vorst, H. A. (1992). Bi-cgstab: A fast and smoothly converging variant of bi-cg for the solution of nonsymmetric linear systems. *SIAM Journal on Scientific and Statistical Computing*, 13(2):631–644.

Wu, X. (2003). A 3-d finite-element algorithm for dc resistivity modelling using the shifted incomplete cholesky conjugate gradient method. *Geophysical Journal International*, 154(3):947–956.